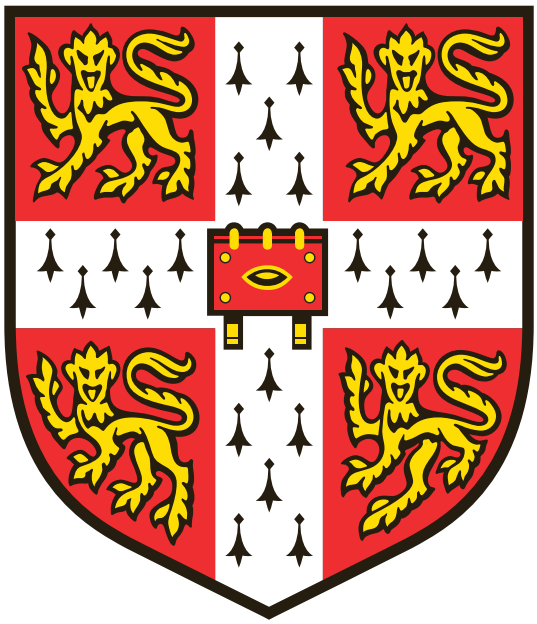

Plastic Deformation in Complex Crystal Structures

Robert P. Thompson

Pembroke College
University of Cambridge

This dissertation is submitted for the degree of Doctor of Philosophy

December 2017

Preface

This dissertation is submitted for the degree of Doctor of Philosophy. This dissertation is the result of my own work under the supervision of Prof. William J. Clegg in the Department of Materials Science and Metallurgy at the University of Cambridge between October 2013 and October 2017.

To the best of my knowledge the research described in this dissertation is original and includes nothing which is the outcome of work done in collaboration except as specified in the text. No part of this dissertation has been or is currently being submitted for any degree or other qualification at any other university. The length of this dissertation does not exceed 60,000 words.

Robert Thompson

Plastic Deformation in Complex Crystal Structures
Robert P. Thompson

Many materials with complex crystal structures have attractive properties, including high specific strength, good creep resistance, oxidation resistance, often through high silicon or aluminium content. This makes them of interest for high temperature structural applications, but the use of many such phases is limited by low toughness. Even outside structural applications, brittle failure is a primary cause of failure in coatings and device materials and, therefore, improved toughness is desirable. In complex crystals plasticity, and hence toughness, is limited by the energy increases that occur as linear defects, *dislocations*, move. This is known as the *lattice resistance*.

By understanding the factors controlling the lattice resistance in complex crystal structures, it is hoped that a general method for tailoring the flow stress of a material might be found. Present ductile-brittle criteria are based on simple ratios of polycrystalline elastic constants and are too limited to accurately capture flow behaviour. There are complex materials which, despite such criteria predicting brittle behaviour, exhibit low flow stresses, though on a limited number of slip systems: MAX phases, Mo_2BC, Nb_2Co_7 and Ta_4C_{3-x} are examples of this.

Where plastic flow is limited by the lattice resistance we must consider the effect of crystal structure on dislocation motion more directly. Aspects which are lost by considering bulk polycrystalline properties are elastic heterogeneity, elastic anisotropy and contributions to the energy changes by other interactions, such as electrostatic interactions. In this work examples of each of these are presented and modelled using an adapted version of the Peierls model.

A Peierls model generalised to use the entire stiffness tensor has been implemented in Python; this allows the investigation of the effect of varying anisotropy on the yield stress of materials that would not be picked up by the use of polycrystalline elastic constants. Calculations using the changing elastic tensor during hydrogen loading of cementite suggest that hydrogen loading causes a dramatic reduction in the flow stress, consistent with experiments and associated with hydrogen embrittlement of steel.

Materials for which empirical potentials can provide more insight than linear elasticity are explored with the example of ionic materials. This is done with a Peierls dislocation configuration and a molecular statics energy calculation. A simple model built electrostatic and Lennard-Jones interactions was used for the rocksalt structure, this model was found to describe the hard slip system well, but was insufficient to describe the softer slip system.

Local heterogeneity in elastic properties is explored in the MAX phases where local variation in chemical environment, characterised by electronegativity, produces pronounced variation in the local stiffness within the unit cell. These local variations have been modelled with density functional theory and have been shown to be consistent with the macroscopic elastic properties while also explaining the apparent scatter in the elastic properties. These non-uniform strains are shown to have a dramatic effect on the flow stress of the MAX phases.

The face-centred cubic Ti_2Ni structure has been used to experimentally demonstrate this effect of heterogeneity softening. The slip system was characterised by micropillar compression and the slip planes were found to be the $\{1\,1\,1\}$ planes. The hardness of a range of alloys with the Ti_2Ni structure was characterised by nanoindentation of the $\{1\,1\,1\}$ faces of single crystals. The hardness was found to decrease as the chemical, and thus elastic, heterogeneity of the unit cell increased, as expected.

This effect of heterogeneity softening presents a potential route to tailoring the yield stress of crystals.

Acknowledgements

Firstly I'd like to thank Bill for his enthusiasm and advice. His approach to science in particular and life in general has made the research group a great place to be. Essential to my project were his willingness to return a problem to basics and patience in helping me think hard about crystals. Without this approach the problems would surely have spiralled out of control.

I'd like to thank the Department of Materials Science and Metallurgy, the University of Cambridge, Pembroke College, the Engineering and Physical Research Council and Rolls-Royce plc for facilities and support, both financial and otherwise, throughout this research.

I'm grateful to all the people that made the Gordon Lab and the department the great place it is: John, Claire, Letitia, Rob, Philip and Joe who helped me settle in way back when, and those of you still here: Tom, Sam, Jimmy, Fernando, Alastair, Megan, Noel, Nashid, Eleanor, Max, Matt, Julia and everyone else. I'd particularly like to thank Joseph Reed and Thomas Furnival for years of friendship and "useful discussions", usually with *just one* drink on the way home.

Thanks are also owed to my other friends who've put up with me through all this, Adam Greig, Max Conway and Laurie Burchell particularly, and to all my other friends who I'm so lucky to know.

Finally I'd like to say how grateful I am to my family for all the support over the years. Mum and Dad, you've helped me to be curious about the world and showed me that we can describe and understand it. You set me on the road to being a scientist, but also kept me sane and happy over this near decade of academia, providing a place to take refuge when I found I still needed to be looked after. I'd also like to thank my grandparents who have all been so important to me, Peter and Barbara, and Alan and Marie.

Thank you all.

Some of the work presented in this thesis has been published in peer reviewed articles:

P. R. Howie, R. P. Thompson, S. Korte-Kerzel and W. J. Clegg, "Softening non-metallic crystals by inhomogeneous elasticity," *Scientific Reports*, vol. 7, no. 1, p. 11602, 2017. DOI: 10.1038/s41598-017-09453-1

R. P. Thompson and W. J. Clegg, "Predicting whether a material is ductile or brittle," *Current Opinion in Solid State and Materials Science*, in press, corrected proof, 2018. DOI: 10.1016/j.cossms.2018.04.001

Contents

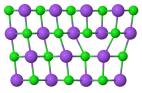

Figures

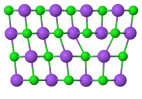

Chapter 1

Plastic deformation

> I have ventured to call them
> dislocations
>
> A.E.H. Love

Plastic deformation or plasticity is the process of permanently altering the shape of a solid body under the influence of an applied external force. Indeed under the application of a large enough force and if cracking can be suppressed, for example by applying a confining pressure, most materials will plastically deform. Though a range of mechanisms for plastic deformation exist in crystals, by far the most common is dislocation glide. Glide was first observed in 1867 [1] and was studied formally as early as 1899 [2, 3]. However it was not known or even proposed that dislocations, linear defects in a crystal structure, mediate plastic flow by moving over rational crystallographic planes [4].

If the process of dislocation glide cannot occur then a material is usually brittle and will fail by fracture or cracking, while if dislocation glide can occur a material is usually ductile and will fail by yielding. The brittleness vs ductility of a material is not a fixed property but depends on the stress state and the temperature. If sufficiently high hydrostatic pressure is applied then even materials like sapphire will undergo plastic flow [5]. At high temperatures, thermal activation can enable glide to occur in materials that are brittle at lower temperatures; many materials are known to exhibit ductile to brittle transition temperatures, for example titanium

carbide, olivine, and body-centred iron [4, 6–8].

Dislocation motion is of much practical importance in crystalline materials. In many metals, particularly those with a face-centred cubic structure such as copper or aluminium, dislocation motion must be hindered to achieve sufficient strength for use as an engineering material. Much of physical metallurgy is the study of the microstructural features that affect dislocation motion and their genesis in materials processing or alloy composition.

In other materials the crystal structure itself provides such a large barrier to motion that almost no plastic deformation is possible and these materials usually fail by brittle fracture. This is true of many non-metallic materials widely used as protective coatings or as functional materials in devices. Fracture is often the life-limiting factor for these materials, thus if their toughness were increased by making plastic flow easier, their lifetime might be extended.

Even in some metallic materials that exhibit comparatively simple crystal structures plastic flow, is limited not by microstructural features but by the inherent resistance of the crystal structure to the motion of dislocations. This is the origin of ductile-brittle transitions in body-centred cubic metals; for example chromium is brittle at room temperature [9] and iron and niobium become brittle at lower temperatures [10, 11]. This is the origin of the failure of the Liberty ships during the second world war in the cold waters of the North Atlantic. Originally thought to be due to high stresses caused by the welding technique used to join the steel, it was Constance Tipper who showed that it was the lack of plastic flow around the crack tip that enabled catastrophic failure of entire ships to occur [12].

Thus, there is a great motivation to understanding the inherent resistance to dislocation flow in a crystal structure, or *lattice resistance*, and in being able to alter that lattice resistance and thereby introduce a degree of toughness to otherwise brittle phases.

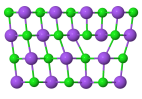

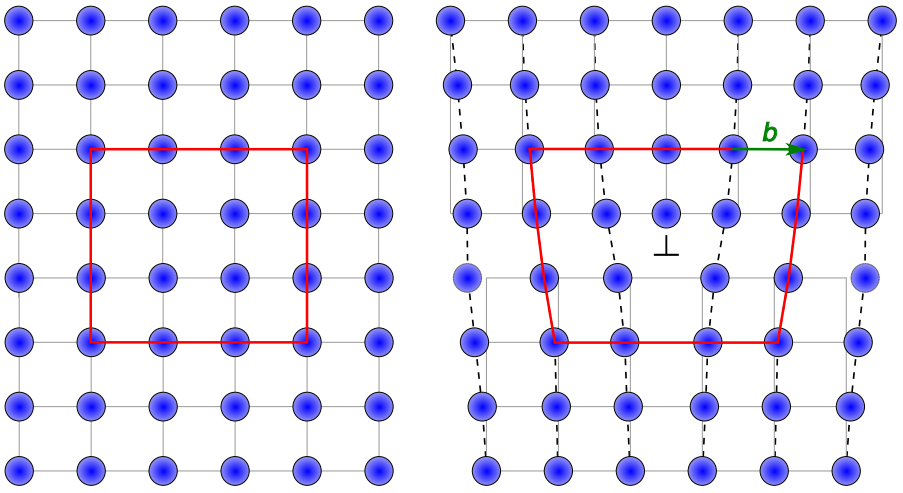

(a) A perfect crystal with a complete circuit shown in red.

(b) An edge dislocation with an incomplete circuit.

Figure 1.1: Inserting a half plane of atoms which terminate in a dislocation and a Burgers circuit to show the Burgers vector.

1.1 Dislocations

Dislocations are line defects in crystals that are important, amongst other reasons, because they are responsible for plastic deformation. Though the character of dislocations varies in a continuous fashion there are two limiting cases: Edge dislocations can be introduced to a perfect crystal by the introduction of an extra half plane of atoms, the termination of this half plane is the dislocation, see Figure 1.1b; screw dislocations are formed by shearing a region of crystal such that the lattice planes form a helix, the centre of which is the dislocation, as shown in Figure 1.2. Mixed dislocations have some of the character of both these end members.

Dislocations can be described in terms of a slip direction, a line direction and a slip plane. The slip direction is simply parallel to the Burgers vector, since this is the relative displacement caused by the passage of a dislocation through a region of crystal. The identification of the Burgers vector is done with a Burgers circuit, comprised of steps between nearest neighbours that would form a closed loop in a perfect crystal. The same set of steps is undertaken in a dislocated crystal and the loop is no longer closed; the displacement vector between the endpoints of the open loop is the Burgers vector. This is shown for an edge dislocation in Figure 1.1, where the Burgers vector is perpendicular to the line vector, and a screw dislocation

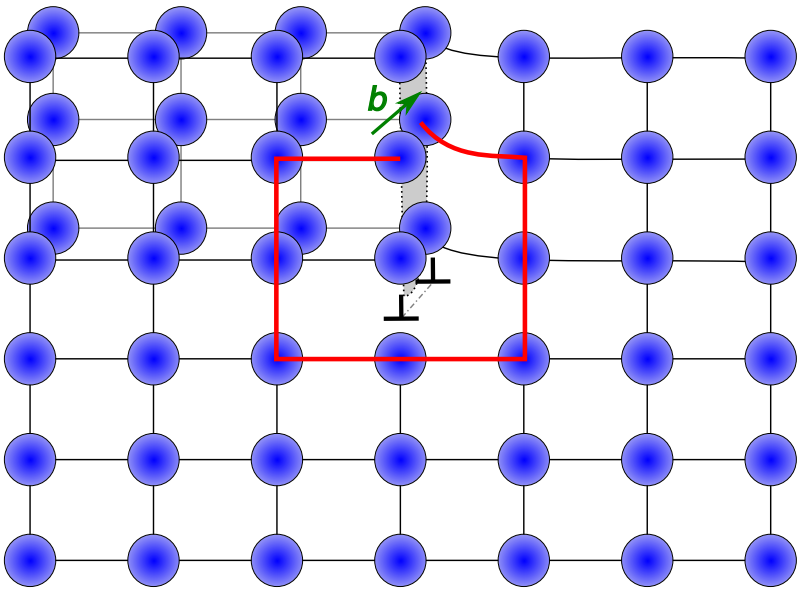

Figure 1.2: Schematic of a screw dislocation with a Burgers loop formed in a similar way to Figure 1.1. The displacement is parallel to the dislocation line in contrast with edge dislocations. The atomic positions are schematic only, the displacements being concentrated unphysically into one half plane.

in Figure 1.2, where the Burgers vector is parallel to the line vector. The line vector varies along the length of the dislocation but is locally the line defined by the defective region of crystal.

The slip plane is the crystallographic plane in which the dislocation can move and must contain the slip direction and line direction. Where the line and the slip directions are not parallel, a single slip plane is defined by these two vectors, but for screw dislocations, for which the slip direction and the line direction are parallel, the dislocation may be considered to lie in several slip planes. Thus screw dislocations can change the plane over which they are move; this process is known as cross slip [13]. Real dislocations are often between these end members, such dislocations are said to be mixed and are usually described as the sum of edge and screw components.

There are conventions about the sense of dislocations. The sense of the dislocation can be defined by the orientation of its Burgers vector relative to its line vector and slip plane. If the line vector is taken to be into the page and the sense of the Burgers loop is anticlockwise then the Burgers vector is defined from the start to the finish of the Burgers loop. This would be positive (i.e. to the right) in Figure 1.1b. Given the high symmetry of most crystals of interest, these choices are arbitrary.

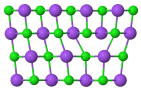

One useful consequence of this description is that if the sense of a dislocation is reversed then its stress/strain field will also reverse in sign. Hence oppositely signed dislocations attract, this lowers the stored elastic energy and potentially annihilates dislocations. Like-signed dislocations will repel to lower the stored elastic energy.

1.1.1 Historical overview

In the early twentieth century there were many observations of real world materials strengths that could not be reconciled with the theoretical shearing strength of a perfect plane of atoms. For a long time this was neglected because, as Gordon [14] explains "until about 1934 the Establishment explanation of these phenomena was remarkably unconvincing and seems to have reflected mainly a desire not to be asked embarrassing questions."

In 1934 the edge dislocation was proposed by Orowan [15–17], Taylor [18], and Polanyi [19] to explain the discrepancy between the ideal strength of crystal and the observed strengths of real materials. It was around this time that work undertaken by Volterra [20] and others, particularly Love [21], on elastic behaviour of homogeneous isotropic continua was related to plastic flow of crystalline materials; idealised dislocations in elastic continua are termed *Volterra dislocations*. By the end of the decade Burgers [22] had described screw dislocations.

It was not until the 1950s that experimental evidence for the existence of dislocations was produced; the initial evidence was growth surfaces of single crystals, preferential etching of a crystalline material at dislocations and x-ray studies of arrays of dislocations in the bulk [23].

Frank [24] predicted, in 1949, that a surface step could terminate at the intersection of a dislocation with a free surface, or conversely a dislocation intersecting with a free surface would necessarily create a step; these were observed soon after in 1950 by Griffin [25]. Preferential etching of dislocations was observed by Horn *et al.* [26] who matched the configuration of etch pits with the pre-existing surface growth features that arise from screw dislocations. The effect of plastic work and

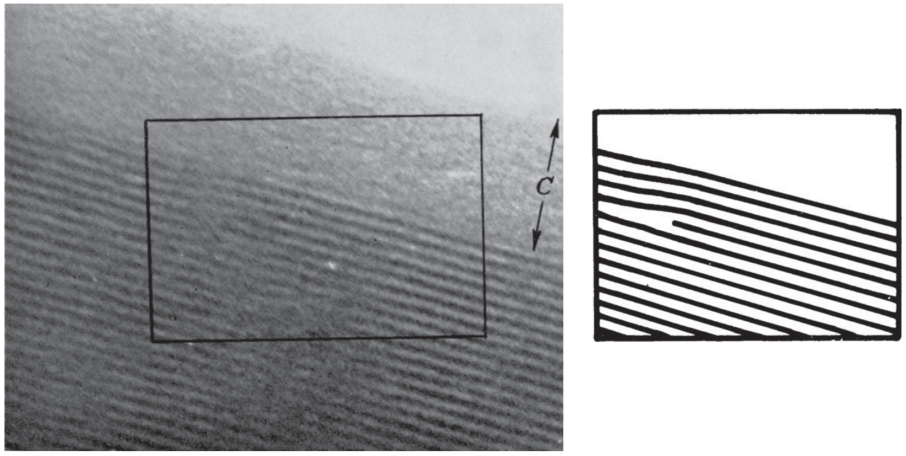

Figure 1.3: The first edge dislocation as imaged by Menter [28].

subsequent recovery on Laue spots (the x-ray beams diffracted by a single crystal) provide evidence of arrays of dislocations. The process was described by Cottrell [27]: Initially sharp Laue spots exist in a perfect crystal. Plastic work smears the spots by introducing a homogeneous distribution of dislocations and the spots then split into distinct sharp spots during recovery as dislocations align into arrays that form sub-grains with small misalignments across the new low angle grain boundaries.

An edge dislocation was first imaged in 1956 by Menter [28] in platinum phthalocyanine. The large organic complex with a platinum atom at the centre produces widely spaced rows of platinum atoms suitable for imaging with transmission electron microscopy. The image of this dislocation is shown in Figure 1.3

1.1.2 The stress required to move a dislocation

Though mathematical descriptions of dislocations in isotropic elastic continua date back to 1907 [20], the energies and forces around dislocations in crystalline lattices were not considered until later. In 1940 Dehlinger and Kochendörfer [29] and Peierls [30] presented dislocation models. The former presented the application of the Frenkel-Kontorova model, a one dimensional array of balls connected by springs on a periodic potential/substrate, to approximate a dislocation.

The latter, Rudolph Peierls, working during the advent of quantum mechanics presented the first formal solution for the energy changes as a dislocation moves in

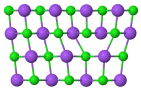

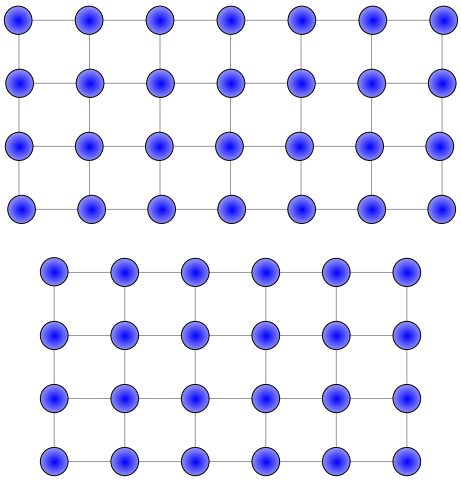

(a) Two semi-infinite crystals

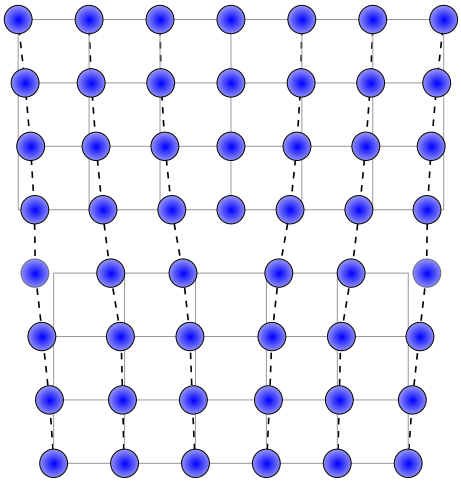

(b) A schematic edge dislocation

Figure 1.4: Schematics showing the creation of an edge dislocation in a simple square lattice by the joining of two misaligned half crystals.

a rather short note [30] and the idea was later extended by Nabarro [31]. The model is remarkably simple: consider two semi-infinite perfect crystals with their lattices aligned but with some initial offset between them as shown in Figure 1.4a. We can join them along what will become the slip plane. An edge dislocation is formed by the localisation of the misalignments to a small region of space, known as the core. This will happen where the energy of the dislocation is less than that of the planar defect.

Atomic configurations that form a dislocation are generated by by applying a displacement field to the atoms immediately above and below the slip plane, $u(x)$ and $u'(x)$ respectively. The Peierls model then estimates the energy of the configuration

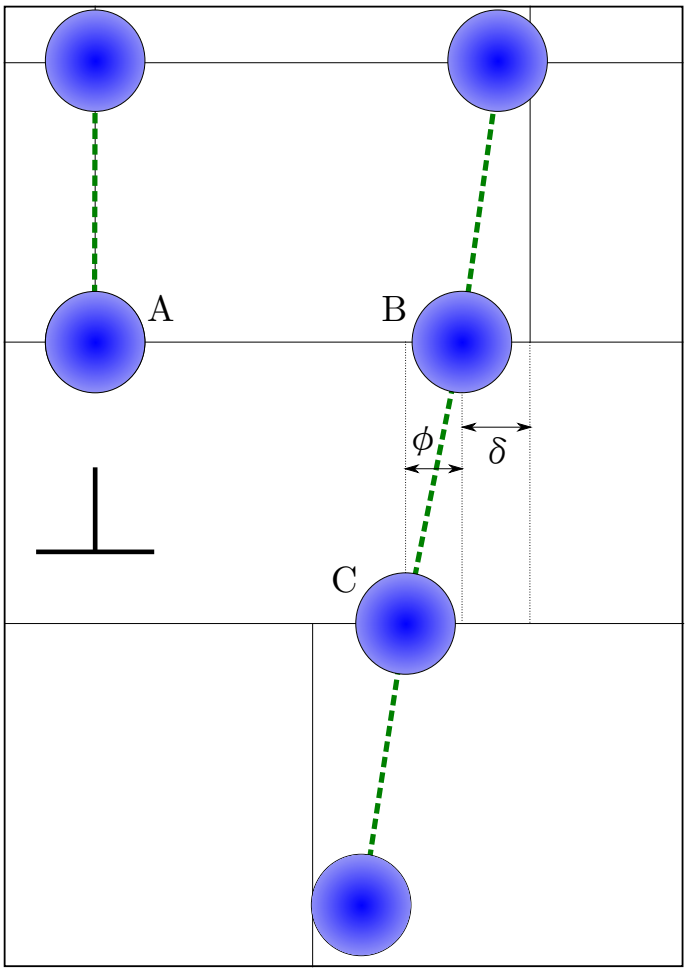

Figure 1.5: Detail of the local displacements around the dislocation core. δ is the extension of the bond parallel to the slip plane between atoms A and B, while ϕ is the misalignment of the bond across the slip plane between B and C.

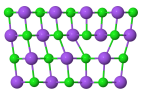

by considering two restoring forces generated by the atomic arrangement. The detail is shown in Figure 1.5. Firstly, the bonds parallel to the slip plane will be either extended or compressed; for example the bond between atom A and B has been compressed by the amount δ. This will tend to oppose the concentration of misalignments to the core and is zero in the case of no displacements from the initial positions. Secondly bonds across the slip plane are misaligned, e.g. the bond between atom B and C is misaligned by a lateral distance of ϕ. This misalignment energy will tend to favour the concentration of the misalignments around the core and is a at maximum in the case of no displacement from the initial position [32].

Peierls made the assumption that the displacements vary slowly with position, i.e. that the dislocation is very wide. This means that the bonds parallel to the slip plane (e.g. bonds like $\overrightarrow{AB}$ in Figure 1.5) experience only small strains. The energy associated with these *in-plane* strains is then described by the application of the displacement field to the surface of two semi-infinite elastic continua. The *misalignment* energy of bonds across the slip plane (bonds like $\overrightarrow{BC}$ in Figure 1.5) is assumed to be a periodic function. The form of the misalignment potential is taken to be sinusoidal:

$$U_{mis} = C \sin\left(\frac{2\pi\phi}{d}\right) \tag{1.1}$$

where d is the slip plane spacing, and ϕ is the disregistry or misalignment across the slip plane.

The constant, C, has to be chosen appropriately but can be found by assuming linear elasticity holds at small strains. Frenkel [33] derived a similar sinusoidal function for the stress to form a stacking fault:

$$\tau_{fault} = \tau_{\text{theory}} \sin\left(\frac{2\pi\phi}{b}\right) \tag{1.2}$$

where b is the Burgers vector and ϕ is the misalignment across the slip plane.

The energy of the dislocation is the sum of all these contributions. There will

be a configuration that is a minimum in the total energy; since the misalignment energy monotonically increases as the dislocation gets wider, whereas the in-plane strain energy decreases monotonically. Hence there will be a point where these two forces are balanced. This gives rise to a size, or width, of a dislocation. The width of the dislocation is defined as the distance from the core where the misalignment, ϕ in Figure 1.5 across the slip plane reaches half its maximum value. Peierls calculated this for an isotropic elastic solid, only accounting for the atomic planes immediately adjacent to the slip plane and found it to be:

$$w = \frac{d}{1-\nu} \tag{1.3}$$

where d is the plane spacing across the slip plane and ν is the Poisson ratio.

The stress required to move a dislocation can be calculated from the maximum energy gradient as the dislocation is displaced. Since the in-plane strains have a continuous definition in this model, the displacement of the dislocation has no effect and the in-plane strain energy does not change. The energy changes therefore depend only on the misalignment energy of bonds across the slip plane.

Peierls derived an expression for the critical stress for yielding in the absence of thermal activation, known as the *Peierls stress*, for an isotropic elastic material in terms of the ideal shear strength as calculated for uniform slip. The analysis only accounted for the interactions between the first plane of atoms either side of the slip plane. The Peierls stress is given by as:

$$\frac{\tau_p}{\tau_{ideal}} = \frac{4\pi}{1-\nu}(5.8 - \log|1-\nu|)\exp\left(-\frac{4\pi}{1-\nu}\right). \tag{1.4}$$

This was refined by Nabarro [31] and the direct summation of the discrete contributions was developed by Cottrell and Nabarro [32]. The result of that summation is:

$$\tau_p = \frac{2G}{1-\nu}\exp\left(-\frac{4\pi w}{b}\right) \tag{1.5}$$

where G is the shear modulus and b is the Burgers vector and ν is the Poisson ratio.

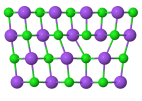

For an isotropic material the width can be substituted from Equation 1.3:

$$\tau_p = \frac{2G}{1-\nu} \exp\left(-\frac{2\pi d}{(1-\nu)b}\right). \tag{1.6}$$

Although this simple model made some significant assumptions, the method moved dislocation theory on in two ways: firstly, continuum elasticity could not account for energy changes as the dislocation moves since in an isotropic homogeneous continuum all the dislocation positions are equivalent. Secondly this approach removes the singularity at the core predicted by continuum elasticity for Volterra dislocations; such a singularity is not physically meaningful.

An important point here is that the Peierls stress is extremely sensitive to the size of the dislocation, w, and therefore to the factors that control the width, which in turn is defined by the lattice geometry, d/b, and the elastic properties.

Peierls found the perhaps surprising result that the energy changes have a periodicity of $b/2$ rather than b. This has been ascribed to the summation procedure of the energy of the misaligned bonds across the slip plane, of which there has been much discussion [34, 35]. Peierls summed over the atoms above the slip plane and below the slip plane independently. This is the "double-counting" scheme. Later models used a "single-counting' scheme in which the assumption of small displacements is dropped and the misalignment of an atom above the slip plane is dependent on the final position of the atoms below the slip plane. This is given as the reason the energy variation had a period of $b/2$ rather than b [34, 35], though it has been suggested that the problem is an artefact that arises from an assumption of small displacements and that using the final rather than initial positions of the atomic rows resolves the difficulties [36].

There is another explanation for the change in period based on symmetry arguments. The period will depend on the exact formulation of the energy and whether the $\alpha = 1/2$ position is symmetrically equivalent to the $\alpha = 0$ or $\alpha = 1$ positions. The periodicity of $b/2$ is easily explained on this basis.

Peierls assumed that both the elastic energy and the dislocation geometry re-

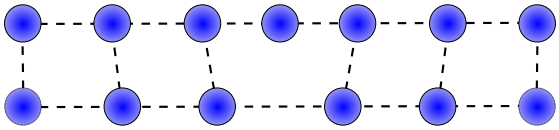

(a) The dislocation configuration for $\alpha = 0$.

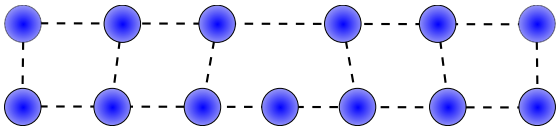

(b) The dislocation configuration for $\alpha = 0.5$.

Figure 1.6: The symmetrical positions of the dislocation. If the displacements normal to the slip plane are neglected and the model is sufficiently wide to ignore edge effects then these situations are equivalent. Peierls [30] assumed the displacements were small and that the strain energy remained constant, effectively neglecting normal displacements. Clegg *et al.* [37] constrained the model to only displace atoms parallel to the slip plane, achieving the same effect.

main constant as the dislocation moves and the only changes in the energy were therefore based on misaligned bonds across the slip plane. Another assumption that Peierls made was that the displacements of the atoms from the initial positions were small and so used the initial positions of the atoms in undistorted planes. These assumptions produce an atomic configuration at $\alpha = 1/2$ that is the reflection of the $\alpha = 0$ configuration across the slip plane, as shown in Figure 1.6. This must give the same energy for both configurations since the misalignment potential used by Peierls is also symmetrical about this plane, i.e. the bonds are mirrored but otherwise unchanged and so cannot have changed in energy.

There have been many criticisms of and modifications to the Peierls model in the years since but these have largely focused on adjusting the assumptions of the original method. In 1951 Foreman *et al.* [38] introduced empirical potentials to describe the energy of the misaligned interactions across the slip plane. They found the width of the dislocation was predicted to be larger than that of the original treatment and this was coupled with a decrease in the Peierls stress.

In 1955 Huntington [36] modified the model to double the periodicity and so account for crystals in which a displacement of half a Burgers vector is not equivalent to the initial position. Maradudin [39] considered a completely atomistic three dimensional model of a screw dislocation but did not consider radial displacements. That work only evaluated the energies of the symmetric and anti-symmetric configurations and so only estimated the energy change, not the maximum stress.

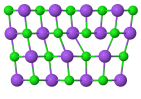

In 1994 a fully discrete model was developed by Ohsawa *et al.* [40]. This model made similar assumptions to the original Peierls model in that the only energy changes were in the sheared misaligned bonds across the slip plane, but instead of solving for an analytical solution Ohsawa et al. used numerical methods to optimise the configuration of 84 atoms, either side of the dislocation core. The model made no assumptions about the displacement field and instead iteratively improved all the atomic positions to find the equilibrium configuration. This was done for increasing applied external stresses until there was no stable configuration, i.e. the point at which slip would occur.

The generalised stacking fault (GSF) energy or γ-surface was incorporated into the Peierls model by Vitek [41] and this was extended by Bulatov and Kaxiras [42]. This improves upon the sinusoidal potential used for the misalignment energy in the original Peierls model. Ohsawa *et al.* [40] had already attempted to address this by using alternative potentials, but used essentially arbitrary functions that fitted the shear modulus at small strains, and so did not improve upon the sinusoidal form used by Peierls and Frenkel [30, 33].

Bulatov et al. retained the variational approach but used density functional theory (DFT) calculations to generate a misalignment potential. They extended the model to include a three dimensional potential, allowing both lateral and vertical displacements of the atoms in the slip plane. This is important around the core where large strains mean that the energy contributions can be inaccurate. By using DFT to calculate the misalignment potential the Peierls model can bridge the length scales between the atomistic core and linear elastic far field. This is no longer analytically solvable but is not difficult to solve numerically.

Analytical approaches to lattice-based Peierls models have continued, for example Joós and Duesbery [43] developed a closed form solution that is valid for narrow dislocations, whereas the original Peierls model assumed that dislocations are wide. This improved the agreement with experiment. The model proposed by Joós and Duesbery required input parameters calculated by empirical or *ab initio* methods

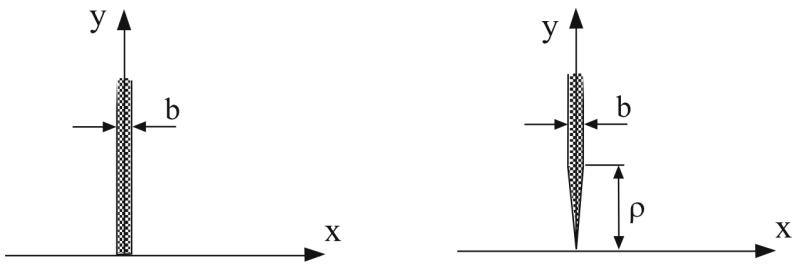

(a) Volterra dislocation. **(b)** Lubarda dislocation

Figure 1.7: The displacement discontinuities in the traditional Volterra dislocation and that used by Lubarda and Markenscoff that removes the singularity at the core. From [44].

but used these as parameters of a closed form solution, in particular they required the maximum restoring stress for the glide plane, i.e. the maximum gradient of the GSF energy.

A continuum elasticity solution was presented by Lubarda and Markenscoff [44] which removed some of the limiting assumptions of the original Peierls model; notably the assumption of fixed dislocation geometry as the dislocation was translated from one symmetrical position to the next and that only the misfit energy of the slip plane changes as the dislocation moves. They also included energy changes in the elastic energy away from the slip plane. The main challenge to using continuum elasticity to solve the Peierls model directly is the singularity in stress and strain at the dislocation core. This singularity arises where the displacement discontinuity of a Volterra dislocation across the half plane of an edge dislocation terminates at the core, as shown in Figure 1.7a. By introducing a gradual increase in the displacement discontinuity across the plane of an edge dislocation from zero at the core to b at some finite distance, as shown in Figure 1.7b, Lubarda and Markenscoff were able to formulate a tractable linear elastic continuum problem which was in much better agreement than previous analytical solutions. They found this distance to be interpretable as the width of the dislocation, giving rise to displacements that are consistent with the original Peierls model.

In 2006, Clegg *et al.* [37] used an atomistic approach to estimate the strains outside of the slip plane in addition to the energy of the misalignment across the slip plane. The atomic displacements were taken to have the same form as Peierls

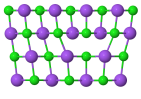

had derived, that is:

$$u(x_0) = \pm \tan^{-1} \frac{x_0}{w}. \tag{1.7}$$

where x_0 is the initial coordinate in the dimension parallel to the Burgers vector and w is the dislocation width, now a parameter to be optimised with no closed form solution.

The misalignment energy was taken to be sinusoidal by analogy with Frenkel [33]:

$$U^{\mathrm{x}} = \frac{Gb^3}{4\pi^2 d} \sum_n \left[1 - \cos\left(\frac{2\pi\phi_n}{b} \right) \right] \tag{1.8}$$

where G is the shear modulus, b is the Burgers vector, d is the slip plane spacing, and ϕ is the misalignment in units of distance, as shown in Figure 1.5. This arises from the requirement that Hooke's law be obeyed at small displacements and that the energy be periodic over a distance b. A schematic of the displacement and dimensions is shown in Figure 1.8. The strain is approximately given by:

$$\gamma_{\mathrm{xy}} = \frac{\phi}{d} \tag{1.9}$$

and so the stored elastic energy is:

$$\begin{aligned} U_{\mathrm{elastic}} &= \frac{1}{2} G \gamma_{\mathrm{xy}}^2 V \\ U_{\mathrm{elastic}} &= \frac{G}{2} \frac{\phi^2}{d^2} b dl \end{aligned} \tag{1.10}$$

where l is the length of the unit cell or element into the plane of the diagram in Figure 1.8

For small values of ϕ we can use the Taylor expansion of the cosine:

$$\cos(x) = 1 - \frac{x^2}{2} + \frac{x^4}{24} - \ldots \tag{1.11}$$

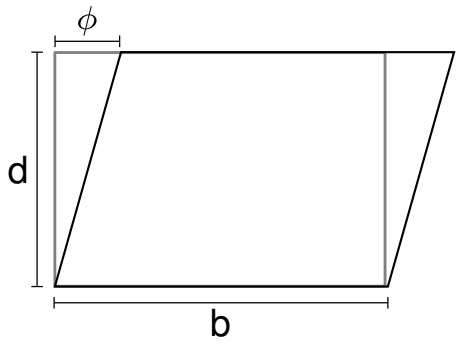

Figure 1.8: Schematic of the misalignment of a unit cell as might be expected at the slip plane. The quantities b and d are the equilibrium lengths in the unstrained state, ϕ is the lateral displacement.

and rewrite Equation 1.8 for a single unit cell or element as:

$$U^{\mathrm{x}} = \frac{Gb^3}{4\pi^2 d}\frac{2\pi^2\phi^2}{b^2} \tag{1.12}$$

which simplifies to:

$$U^{\mathrm{x}} = \frac{G}{2}\frac{\phi^2}{d^2}bd \tag{1.13}$$

which is a line energy in units of $\mathrm{J\,m^{-1}}$ so as an absolute energy is:

$$U^{\mathrm{x}} = \frac{G}{2}\frac{\phi^2}{d^2}bdl \tag{1.14}$$

which is the same as Equation 1.10.

The in-plane strain energy is taken to be:

$$U^{\mathrm{i}} = \frac{E}{2(1-\nu^2)}(b\cdot d)\sum_n \varepsilon_n^2 \tag{1.15}$$

where E is the Young's modulus, ν is the Poisson ratio, b is the Burgers vector, d is the slip plane spacing, ε is the strain calculated by $\varepsilon = \delta/b$, and δ is the extension of an in-plane bond, as shown in Figure 1.5. The energies are then summed over interaction between atomic rows extending 1000 atomic spacings either side of the dislocation core.

The width no longer has an analytical solution, so must be found numerically. The true value is taken to be that which gives the lowest energy of the dislocation.

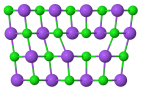

The variation of the energy is smooth and has only one minimum. This is because the misalignment energy increases monotonically with increasing width and the elastic in-plane strain energy decreases monotonically.

It is interesting to note that this formulation restores the symmetry that is destroyed in the calculation of elastic energy by continuum elasticity. The strains above and below the slip plane are symmetric, so despite allowing the strain energy to vary as the dislocation moves, this model has the same period as the original Peierls model of $b/2$.

1.2 Ductility criteria

In most structural applications a catastrophic brittle failure by fast fracture is unacceptable. Furthermore many materials used in devices or coatings both protective and functional often fail by brittle fracture and so a material that is more ductile, at least relatively, may have improved performance. This has motivated numerous attempts to find ductility criteria to predict from simple and easily measurable properties whether a material will fail in a ductile or a brittle manner.

The Pugh ratio, B/G where B is the bulk modulus and G is the shear modulus, is one of the most widely known and is still used today [45–49]. This ratio is used to indicate the relative ease of either plastic deformation or brittle fracture. High values of this ratio should tend to indicate ductility while low values should indicate brittleness. This can be physically justified on the basis that the resistance to slip is proportional to the shear modulus: as Pugh discussed, the Orowan bowing stress is proportional to G, but it can also be justified from the lattice resistance, which is also proportional to G, see Equation 1.6. For a given lattice, i.e. constant d/b, the shear flow stress should scale with the shear modulus. In a similar way, the ease of fracture must be related to the ease of separating layers of atoms. Since this must relate to the energy of straining bonds and the energy of creating surfaces, Pugh took the bulk modulus is a reasonable proxy. This gave good results empirically when Pugh [50] analysed a wide range of material data.

However this does not accurately capture reality. For example for two face-centred cubic metals, aluminium and copper, for which B/G is 2.74 and 3.00 respectively, and these metals both show large elongations to failure. For rhodium and iridium, B/G is 1.77 and 1.74 respectively, and they show small elongations to failure [50]. On the other hand very brittle phases are easily found with similar values of B/G; the C15 Laves phases [51, 52] $NbCr_2$ and HfV_2 have large values of B/G, 2.88 and 3.47 respectively [53], but exhibit no significant plasticity. In contrast Ti_3SiC_2 has a value of B/G of 1.37 (using experimental polycrystalline values) [54] and shows very easy slip.

Rice and Thomson [55] suggested an alternative approach based on the energetics of sharp crack tips and whether blunting dislocations can be spontaneously emitted. The analysis used the Peierls approach to evaluate the energy of a dislocation close to free surfaces and found that the term Gb/γ_s, where γ_s is the surface energy, G is the shear modulus and b is the Burgers vector, to be a dimensionless value that reflects the propensity to fail by either ductile or brittle means and is justified along similar lines to the Pugh ratio. Gb scales with the energy of emitting a blunting dislocation, so high values will oppose the formation of dislocations and blunting of cracks, thus favouring brittle failure. On the other hand γ_s represents the energy of the crack and high values will tend to favour reduction of the surface by blunting and favour ductile failure.

The Rice and Thomson criterion [55] was updated by Rice [56] to be the quotient γ_{us}/γ_s where γ_{us} is the unstable stacking fault energy and γ_s is still the surface energy. This criterion follows essentially the same reasoning but no longer makes the assumption that γ_{us} scales linearly with G.

An alternative condition was put forward by Zhou *et al.* [57] that does not include the surface energy. They propose the energy to blunt a crack by dislocation emission is dependent on γ_s in the same way as the energy of growing the sharp crack, since the formation of a dislocation creates ledges and alters the surface area. In this way the ratio of the energies is independent of the surface energy (though the absolute

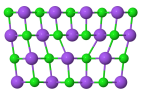

value of either energy is clearly dependent on γ_s) and so the crossover from brittle to ductile behaviour is also independent of the surface energy. They find instead that the appropriate quotient is γ_{us}/Gb and set a critical value of 0.014. As the authors note, this is an interesting result because the critical threshold is not the cross over in a competition between two processes, one of fracture and one of plasticity, but instead is equivalent to a critical value of the Peierls energy.

One drawback of these more physically insightful approaches is that strictly they apply only for one slip system and one mode of fracture on one plane and so must be recalculated for all possible combinations and then averaged with some appropriate statistical weighting. These criteria can become rather cumbersome: experimental determination of the unstable stacking fault energy and the surface energy is laborious, and calculations quickly become time consuming as combinations of fracture and slip modes are considered. They also rely in all cases on two assumptions: Firstly the energy barrier for slip or emission of dislocations, via the Peierls model, scales linearly with the stacking fault energy or shear modulus; secondly that the stress required for slip scales simply with the Peierls energy. These quantities will be related but it is unlikely that the relationships are simple, as would be needed for such ductility criteria to be reliable.

An example for which these criteria break down is the contrast between the phases titanium carbide, TiC, and the ternary carbide MAX phase Ti_3SiC_2. The above models all correctly predict that TiC is brittle: The value of $\gamma_s/\gamma_{us} = 1.76$ is too small with values in excess of 3 required for ductility [58, 59] and the values of $Gb/\gamma_s = 20.48$ and $\gamma_{us}/Gb = 0.032$ are too large to indicate ductile behaviour [59, 60]. However these same criteria produce similar values for Ti_3SiC_2, for which $\gamma_s/\gamma_{us} = 1.42$, $Gb/\gamma_s = 27.3$ and $\gamma_{us}/Gb = 0.0219$ [60, 61]. The Pugh model and the two Rice models [50, 55, 56] actually predict the MAX phase to be more brittle than stoichiometric titanium carbide. This is at odds with reality since titanium carbide has a yield stress of over 2 GPa at temperatures below 600 °C [62] while at room temperature the critical resolved shear strength of Ti_3SiC_2 is reported to be

36 MPa [63], though reanalysis of the data suggests the strength is higher at 77 MPa [64].

The inability to capture or predict the ductility or brittleness of materials limits the use of these ductility criteria; while they highlight some perhaps noteworthy trends they could not have been used to predict the anomalous yielding in the MAX phases and other layered compounds that are now being commercialised to take advantage of the high temperature capability that arises from their chemistry.

1.3 Tailoring the Peierls stress

Attempts to relate the electronic structure to plasticity have been made, but even recently such studies have tended to find structural, physical and elastic properties of "complex" materials and then infer the relative ductility on the basis of these properties, usually the ductility criteria discussed above. For example the addition of Mo or W to certain ternary metal nitrides with chemistry obeying $Ti_xM_{1-x}N$ is predicted to significantly improve the toughness, an effect dubbed "*supertoughening*" [45, 65]. The authors use *ab initio* calculations to find the elastic response of the alloyed crystal to an applied strain. They find a number of interesting things including the development of a layered electronic structure and trends for elastic properties, particularly the Pugh ratio, B/G, with the valence electron concentration. The authors speculate about selective local responses to stress, though with no further exploration since the elastic constants were calculated from the energy changes under uniform applied shear strains.

However the conclusions drawn from these purely elastic simulations about plasticity can be, at best, qualitative. These studies are based on arguments of easily broken bonds since "during dislocation motion bonds are broken and reformed and, obviously, dislocation glide will occur more easily in planes normal to those containing weaker bonds" [45] without further justification. Clearly this is not a mechanistic explanation for the effect of chemical bonding on plasticity, instead relying on dated and empirical ratios of elastic constants.

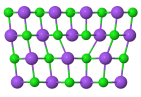

Other studies recognise the limits of simple ductility criteria and use the concept of Peierls stress more directly [66–68]. They use the established results for simple materials, i.e. taking no account of local heterogeneities is made, so that the distribution of strains is always uniform; often the materials are simply taken to be isotropic continua. The conclusions that can be drawn from applying a simple model to a complex structure are limited to those that could be drawn from the simple model: i.e. that if the elastic constants and stacking fault energies take suitable values then the dislocation will be wider or that the ratio of the slip plane spacing and the Burgers vector will allow easier slip. Given these are evident from most of the formulations for the Peierls stress, it does not shed much light on the ideal material to use or how to modify materials to improve their ductility.

1.4 Layered crystals

Some layered compounds have been shown experimentally to have very low flow stresses when compared with analogous materials. One example is Ti_3SiC_2, which has a (uniaxial) yield stress of 200 MPa [54], this can be compared with titanium carbide which yields at stresses of around 1 to 2 GPa even at temperatures of 600 °C. This is significant since the main barrier to plastic flow in TiC is the lattice resistance up to very high temperatures [69]. Another example is Nb_2Co_7, this phase has a layered monoclinic structure and yields at a critical resolved shear stress of between 100 MPa and 500 MPa, and this can again be contrasted with the critical resolved shear stress of the related phase $NbCo_2$, a cubic Laves phase that has a critical resolved shear stress of between 2 and 5 GPa [70]. There are other layered crystals that seem to show similar behaviour: W_2B_5 has been observed to behave analogously with the MAX phases, with a weak basal plane [71] and $\zeta - Ta_4C_{3-x}$ exhibits higher toughness and lower hardness than the equiatomic TaC, possibly pointing to easier plastic flow [72].

If the relatively easy plastic flow in these complex structures can be explained then this understanding could form the basis of controlling the lattice resistance

and so the ductility of materials that are ordinarily brittle. This is clearly of great interest because many brittle materials show attractive properties including high specific strength, good creep resistance and environmental stability. For example, the MAX phase Ti_3SiC_2 is stable to over 2300 °C, forms a protective silica scale and has a specific stiffness roughly three times that of titanium [73].

1.4.1 MAX phases

The MAX phases are a group of layered compounds with a hexagonal crystal structure. The compositions obey the form $M_{n+1}AX_n$ where M is an early transition metal such as titanium or niobium, A is a group A element (usually IIIA or IVA) and X is either carbon or nitrogen. The possible stoichiometries lead to the shorthand 211, 312, 413 etc, these are shown in Figure 1.9.

The crystal structure can be usefully described as the stacking of layers parallel to (0 0 1) of MX and MA which share M atoms, shown in Figure 1.9. The MX regions have the same octahedral coordination of X by M as would be expected from phases such as TiC. The MX layers parallel to the (0 0 1) plane of the MAX phases can be described as an integer number of {1 1 1} layers of TiC, as shown in Figure 1.10. The MA regions take a quasi-close packed structure, with a hexagonal layer of A atoms between two of M atoms stacked as one would expect of hexagonal metals. As with the MX regions, there are two MA blocks in the unit cell. The crystal symmetry fixes certain atomic positions and unit cell parameters. The free parameters are: the lattice parameter a, the ratio of lattice parameters, c/a, and the z-positions of certain atomic sites. In the 211 phases the M1 site is free to move in the z-direction, in the 312 phases the C1 and M2 sites are free and in the 413 the M1, C2, M2 and A1 sites are free. The sites are labelled in Figure 1.9.

The description of complex crystals is often in terms of clusters of atoms that appear to pack together and fill space. The clusters may or may not have physical significance: for example clusters of up to 55 atoms of Ni-Al are stable on surfaces and so are clearly physically significant, but geometric descriptions of clusters can be

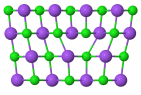

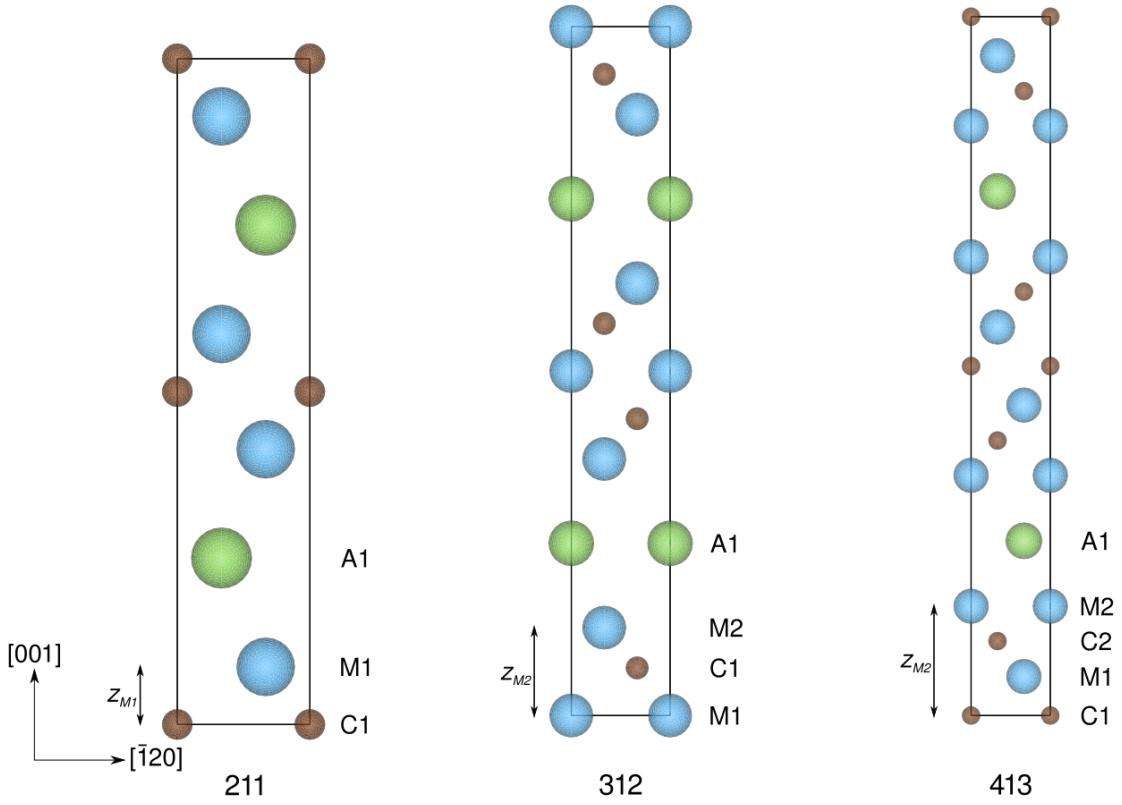

Figure 1.9: The unit cells of the first three possible MAX phases. Graphics prepared with VESTA [74].

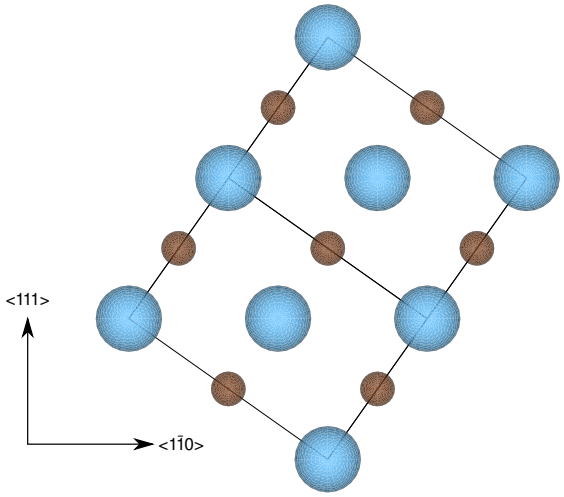

Figure 1.10: The unit cell of TiC, which has the rock salt structure, oriented to show the {1 1 1} planes which are equivalent to the MX layers of the MAX structure shown in Figure 1.9. Graphic prepared with VESTA [74].

made of simple materials like FCC aluminium [75]. Care must be taken therefore not to ascribe undue significance to purely geometric features, but the description of the MAX crystal structure as layers is not simply geometric but can be justified on the basis of heterogeneity in the chemical environments, i.e. the layers are meaningful.

The bonding in MAX phases has been shown, by density functional theory (DFT) calculations, to be a combination of metallic, covalent and ionic bonding but with covalent bonding predominant in the MX layer and metallic bonding in MA layers. Large variations in structural and mechanical properties are observed to depend on changes in the nature of this heterogeneous bonding character [73, 76]. Notably the extreme (among MAX phases) properties of Ti_2SC are ascribed to the unusual strong bonding between Ti and S in addition to the strong bonding between Ti and C in contrast with most other MAX phases. This unusual bonding is taken to underlie the high elastic constants, $E = 316\,\text{GPa}$ the highest of any 211 MAX phase, and hardness of 8 GPa, very nearly the highest of any bulk MAX phase [76, 77].

1.4.2 Deformation in MAX phases

Deformation in Ti_3SiC_2 has been widely studied, particularly by Barsoum [63, 78–81], and was found to readily occur by the glide of dislocations. Room temperature deformation was shown to increase the density of perfect basal dislocations with a Burgers vector equal to the lattice parameter a, so $b = <1\,1\,\bar{2}\,0>$.

Using heavily textured bulk samples of Ti_3SiC_2 the critical resolved shear stress of Ti_3SiC_2 was estimated by compression test. A sample with the basal planes of the sample oriented at approximately 65° to the compression axis and a yield stress of 200 MPa was measured. Schmid's law is:

$$\tau_y = \sigma_y \cos\phi \cos\lambda \tag{1.16}$$

where τ_y is the shear yield stress on the slip plane in question, σ_y is the uniaxial yield stress ϕ is the angle between the slip plane normal and the loading axis, and

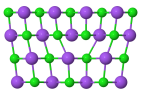

λ is the angle between the slip direction and the loading axis. The ϕ must be 25° (= 90° − 65°) but λ is not known but if taken to be the maximum possible value, given $\phi = 25°$, of 115° then $\tau_y = 77\,\text{MPa}$, providing an upper bound [64]. While this is higher than the estimate made by the original authors [63], Humphrey [64] points out that this is likely an overestimate due to the variation in Schmid factor across the sample and load redistribution between soft and hard grains but in any case is very low for a ceramic and approaches the flow stresses of pure cubic close-packed metals.

As discussed in section 1.3, attempts have been made to explain and hence control the lattice resistance of materials, and this has been done for the MAX phases too. One study on MAX phases [82] with the chemistry M_2AlC (M = Ti, V, Cr) used more recent ductility criteria, namely Zhou-Carlsson-Thomson [57] and Rice [56], which were discussed in detail in section 1.2. There is recognition that the lattice resistance of a single dislocation, which is what limits ductility in most ceramics, is not simply dependent on bulk elastic constants. The authors therefore calculate ductility criteria based on stacking fault energies and surface energies, which necessitates choosing which plane to fault or cleave. In the MAX phases there are two natural choices: between the M atom and the A atom or between the M atom and the X atom. However there is no direct link, in these studies, between these properties and dislocation behaviour, and hence no direct link to the ductility.

Some studies have considered the Peierls stress in complex crystals with layered structures [66–68] but usually these have simply applied the result for an isotropic elastic material, as given in Equation 1.6.

The result is therefore based on polycrystalline bulk elastic properties and the specifics of the MAX crystal structure are disregarded save the values of d and b chosen. These have tended to give high values of the Peierls stress, e.g. 980 MPa for Ti_2AlC [66] which we can compare with 700 MPa observed experimentally in TiC [37]. The strength of TiC should be an upper bound on the flow stress in the MAX phase, since the MAX phases contain planes of TiC. Furthermore these planes of

TiC in the MAX phases are equivalent to the slip planes in TiC [69].

The GSF calculated by DFT has been used in at least one study [68] but assumed that no change in confining elastic field occurred during dislocation motion, which has been shown to be significant [37, 44]. Gouriet *et al.* [68] predict a Peierls stress between 611 MPa and 957 MPa, which is also similar to the experimental observation for TiC.

The effect of crystal chemistry on the lattice resistance in the MAX phases is very strong, and it has not been completely explained. If the factors controlling lattice resistance can be understood, there may be a route to tailoring the Peierls stress of a material. In this way the ductility of otherwise brittle phases could be improved.

1.5 Alternative energy formulations

The Peierls model is based on a linear elastic formulation of the energy, perhaps with a fitted misalignment potential. Other formulations might provide more insight. Empirical potentials have been developed for a wide range of materials and conditions for the field of molecular dynamics. These potentials are computationally tractable, at least compared to quantum mechanical treatments, while hopefully retaining enough fidelity to actual behaviour to give physical insight [83].

Various potentials exist for different types of materials, which usually are applicable to only some classes of materials. For example, the embedded atom method applies well to metals [84], the Lennard-Jones and Buckingham potentials describe dispersion interactions, and the short range exchange interaction arising from Pauli exclusion [85, 86] and bond order potentials describe covalent bonding, e.g. the Tersoff potential [87].

Ionic solids are an ideal class of materials with which to demonstrate the application of alternative energy calculations by applying empirical potentials. Some modelling of dislocation motion by the conventional Peierls-Nabarro model, using the elastic properties and the generalised staking fault energy, has been undertaken

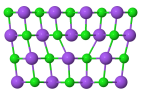

for MgO [88], however the chemical bonding is well described by fairly simple empirical potentials that could provide more insight into the factors controlling plasticity than linear elasticity.

There are large numbers of ionic solids with the same simple crystal structures, e.g. rock salt and caesium chloride [89], and the primary contribution to the energy of these materials is the electrostatic interaction, which is mathematically simple:

$$U_{ij}^{\text{electro}} = \frac{1}{4\pi\varepsilon_0}\frac{q_i q_j}{r_{ij}} \tag{1.17}$$

where ε_0 is the permittivity of free space, q_i is the charge on atom i and r_{ij} is the separation between atoms i and j.

The Lennard-Jones potential is often used to capture the shorter range interaction in ionic solids. The Lennard-Jones is one of the simplest formulations to represent these interactions in ionic solids and has the form:

$$\phi_{ij}(r_{ij}) = 4\varepsilon_{ij}\left[\left(\frac{\sigma_{ij}}{r_{ij}}\right)^{12} - \left(\frac{\sigma_{ij}}{r_{ij}}\right)^{6}\right] \tag{1.18}$$

or in the "A–B" form:

$$\phi_{ij}(r_{ij}) = \frac{A_{ij}}{r_{ij}^{12}} - \frac{B_{ij}}{r_{ij}^{6}} \tag{1.19}$$

where r_{ij} is the atomic separation, ε_{ij} is the depth of the energy minimum, σ_{ij} is the atomic separation at which the energy is zero and A_{ij} and B_{ij} are simply parameters to be fitted and are related to ε_{ij} and σ_{ij} by $A_{ij} = 4\varepsilon_{ij}\sigma_{ij}^{12}$ and $B_{ij} = 4\varepsilon_{ij}\sigma_{ij}^{6}$. The total energy for a pair of atoms is then:

$$U_{ij}(r_{ij}) = \frac{1}{4\pi\varepsilon_0}\frac{q_i q_j}{r_{ij}} + \frac{A_{ij}}{r_{ij}^{12}} - \frac{B_{ij}}{r_{ij}^{6}} \tag{1.20}$$

The energy of perfect ionic crystals is relatively easily calculated via a Madelung or Ewald summation [90, 91], but these usually rely on an assumption of symmetry; an assumption that is broken by the introduction of a defect. In the case of a dislocated crystal another approach is required. One option is a direct sum, which

scales with the square of the number of atoms in the simulation. If the distance from the dislocation line is considered the simulation time scales with the fourth power, which can rapidly become intractable. However advances in computing hardware and efficient implementations of array operations in NumPy [92], particularly an efficient implementation of the Einstein summation convention [93] may make this a workable solution.

An alternative is to use an implementation of a long range electrostatics solver that allows for non periodicity in two dimensions. One such implementation is the multiscale summation method in LAMMPS [94–96], which divides the problem into one short range potential plus a series of smoothly vanishing long range potentials over increasingly coarse meshes at larger interatomic distances. The use of LAMMPS allows the extension of the energy calculations to other energy terms such as polarisability of ions and so on.

1.5.1 Dislocations in ionic crystals

The rocksalt structure is particularly common in ionic solids and phases of this structure have been widely studied in terms of their plasticity. The slip direction is usually $<1\,1\,0>$ and the active slip planes are $\{0\,0\,1\}$ and $\{1\,\bar{1}\,0\}$, and sometimes $\{1\,\bar{1}\,1\}$. For edge dislocations the last would expose charged surfaces of atoms at free surfaces, so despite being the closest packed plane it is not commonly seen [97]. Schematic illustrations of edge dislocations are shown in Figure 1.11.

Experimental work has characterised the yield stress of ionic solids with the rocksalt structure over a wide range of temperatures, including very low temperatures by using liquid helium ($\sim$4 K), and they deviate strongly from the prediction of elastic Peierls models. This makes them useful as a model system for testing dislocation theories [97].

Previous modelling of dislocations in ionic crystals has been undertaken, notably by Puls and Norgett [98] who simulated edge $\{0\,0\,1\}<1\,\bar{1}\,0>$ dislocations in MgO, and by Woo and Puls [99] who modelled the same dislocation geometry in a range

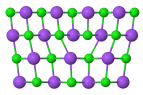

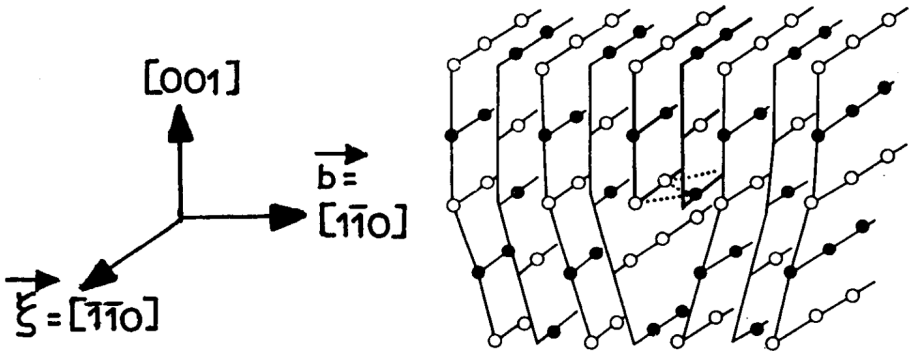

(a) The {0 0 1}<1 $\bar{1}$ 0> slip system.

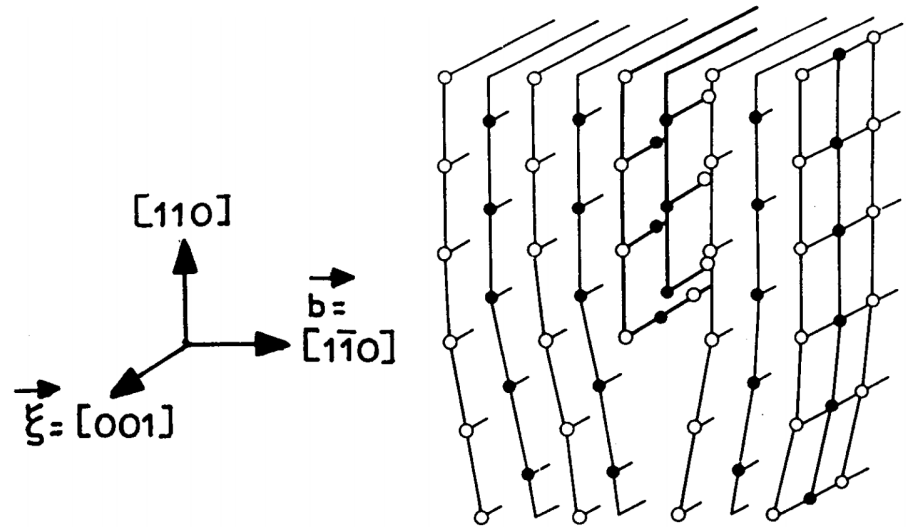

(b) The {1 1 0}<1 $\bar{1}$ 0> slip system.

Figure 1.11: Schematic edge dislocations in the rock salt structure reproduced from [97].

of ionic crystals with the rocksalt structure, among others [100–105]. These were limited by the computational resources available and used a variety of strategies to overcome these limits; one approach was to optimise only the equilibrium position and then assume linear trajectories for the atoms for intermediate states, as developed by Granzer *et al.* [100]. This is similar to the assumption made by Peierls [30] that the dislocation width does not vary between the equilibrium positions, which has been shown to have a very large effect on the results [37, 42].

Another method to overcome computational limitations was to simulate only small regions atomistically. This was achieved by applying a variety of boundary conditions, usually derived from elasticity theory, to constrain the atomistic region and modelling material outside this core region as elastic. Such conditions were used in [99]. The use of conditions like these prevents the separation of the different energetic components since there is always a large contribution from the elastic region as well as the electrostatics and short-range interactions. A fully atomistic simulation would hopefully show the individual energy contributions and give some insight into the dominant factors controlling dislocation motion.

A fully atomistic model using suitable interatomic potentials will hopefully illustrate the factors that control dislocation motion in ionic solids.

1.6 Summary of background information

Dislocations are key to the properties of many crystals. In materials such as ceramics and intermetallics the crystal structure itself presents the largest barrier to dislocation motion. This normally limits the applications of ceramic and intermetallic phases, which have attractive properties but exhibit such limited plasticity that they are too brittle for structural applications.

There are some ceramic and intermetallic phases, such as the MAX phases or Nb_2Co_7, that do show relatively easy plastic flow, though usually limited to a small number of slip planes. Since this happens in phases with similar chemistry to other, brittle, phases (such as the MAX phases vs TiC and Nb_2Co_7 vs $NbCo_2$) this change

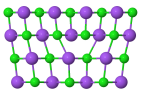

in behaviour is likely to be due to the crystal structure.

The Peierls stress, i.e. the lattice resistance in the absence of thermal activation, can be predicted using a Peierls model. There are a number of such models in the literature that make a variety of assumptions about the nature of the energy calculations and the atomic displacements around the core. The best models make use of the generalised stacking fault, whereby a planar defect is modelled accurately by density functional theory and the results of that model are assumed to be applicable as a misalignment potential in a more element-based model of the dislocation core. Another common assumption is that the atomic displacements are only parallel to the slip plane.

More complex or computationally intractable approaches have gradually been introduced but few, if any, Peierls models have attempted to combine more complex displacement fields and generalised stacking fault energies with an atomistic-scale model of the whole dislocation structure.

This leads the current work down two distinct, complementary paths. One challenge is to develop the Peierls model to reduce the number of assumptions about atomic positions and the interactions between them. This seems particularly tractable by incorporating complex displacement fields and new energy calculation methods.

In particular the assumptions that the atomic displacements are only parallel to the slip plane and are small in planes not immediately adjacent to the slip plane and therefore discarded are possible to address by the use of more generalised displacement fields. Such a displacement field then allows the treatment of materials using empirical potentials that apply over long distances, such as the Lennard-Jones potential for ionic materials, potentially addressing the slip in alkali halides that has not been well described by Peierls models based on linear elasticity.

If successful this would open the way to treating the effects of crystal structure on dislocation behaviour more fully. However in the case of a new model the ideal test case is not a complex crystal with behaviour that is not well understood.

Rather, a model is better developed and tested against well understood behaviour of simpler materials and then applied to complex crystals. For the purposes of developing a model simpler crystals are appropriate, such as pure elements, such as copper, iron and diamond, and simpler covalently bonded crystals such as titanium carbide. This covers a wide range of lattice geometries and yield stresses and is generally well described by exiting models. In this way it can be hoped to improve the generality of the Peierls model and broaden its applicability while also characterising its ability to predict, accurately, known behaviour.

In parallel, there is immediate interest in the low flow stresses observed experimentally in layered crystals such as the MAX phases. This can be addressed by adapting existing methods; using insight into the crystal structure to inform quantum mechanical modelling of complex phases, and altering an existing Peierls model to take account of this.

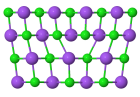

Chapter 2

A new Peierls model

> Dislocation theory is after all,
> perhaps mainly of interest to
> dislocation experts
>
> *J. E. Gordon*

Though there are a number [31, 36, 37, 41, 42, 44, 68, 98] of Peierls models published in the literature over the decades since Peierls [30] first presented his solution, few have been applicable to situations beyond the initially envisaged problem, which is somewhat narrowly defined for an orthorhombic lattice that obeys linear elasticity. In this chapter a model is presented that allows the consideration of energies defined by linear elasticity using the full elastic tensor, empirical potentials and generalised stacking fault energies. The model is also kept modular to allow extension to other formulations, e.g. a full quantum mechanical treatment using density functional theory.

This model does not aim to radically deviate from all the previous work on the Peierls model, there is no need to as much progress has been made over the years. Instead this new model aims to bring together as much of that previous work as possible to try and provide new insight into the behaviour of dislocations. For example, the use of ionic empirical potentials is not new, [102], and neither is the idea of fitting a misalignment potential and numerical optimisation of the structure rather than closed form solutions [42], others have considered a more generalised

displacement field [44] and the full elastic stiffness tensor has been used since very early in the study of dislocations [106]. There is however scope to further combine these different factors, along with more powerful computers in the modern era, to provide a more generalised model while relaxing the assumptions and simplifying constraints enough to provide insights into unusual dislocation behaviour.

The Python programming language was chosen for a number of reasons. Firstly the Python model is inherently modular, which provides a flexible structure, allowing parts of the model to be altered, extended or replaced quickly and easily. Secondly Python is also widely used for scientific computing, with a comprehensive body of documentation and a large support community. Finally Python has a very large number of extending modules providing advanced capabilities, particularly projects like NumPy and SciPy. NumPy provides a powerful and efficient implementation of arrays and a range of simple functions as well as more advanced linear algebra operations. SciPy is a project built on the basic data structure of the NumPy array and provides advanced algorithms and convenience functions including differential equations, numerical solvers and optimisers, image processing and statistical functions. The code written in this work has been published on-line [107].

To calculate the Peierls stress we must find the changes in the dislocation energy as a dislocation moves from one low energy position to the next. The variable α is used to denote the displacement of the dislocation as a fraction of the Burgers vector, b. Since boundary conditions are insufficient to define the atomic configuration, for each value of α the atomic configuration of the dislocation that minimises the energy must be found. Once sufficient samples of α have been made the Peierls stress can be calculated by:

$$\tau_p = \frac{1}{lb^2} \left. \frac{\partial U}{\partial \alpha} \right|_{max} \tag{2.1}$$

where l is the length of dislocation line for which the energy, U, is calculated for and b is the Burgers vector.

For a given value of α the lowest energy configuration is found via three steps: first the definition, creation and representation of an atomic configuration, second

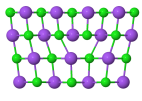

the evaluation of the overall energy, and third the iterative improvement of the configuration to find the minimum energy. Taken together the first two steps can be thought of as a function that takes the value of α along with some input parameters as arguments and returns the total energy:

$$U_{\text{total}} = f(\alpha, p_1, p_2, ..., p_n) \tag{2.2}$$

The input parameters, p_i, could be as general as the coordinates of every atom in the configuration or as specific as the single parameter defined by Peierls in his original treatment, the width of the dislocation. The main difference is trade off between computational tractability and the risk of over-constraining the model. Algorithms exist for finding the minimum of functions of the form given in Equation 2.2. Such algorithms are much faster for functions with small numbers of parameters and some algorithms are not reliable for large numbers of parameters. Hence decisions about how to define an atomic configuration will have consequences for the optimisation of that configuration to find the lowest energy.

Here the positions of the atoms are used to define the configuration and then constraints applied. Hence individual atoms are represented in space by coordinates as an array of the form:

$$atoms = \begin{pmatrix} x_1 & y_1 & z_1 \\ x_2 & y_2 & z_2 \\ . & . & . \\ . & . & . \\ x_n & y_n & z_n \end{pmatrix}$$

where x_i, y_i and z_i are coordinates in Euclidean space of the ith atom, in units of Ångströms, i.e. *not* relative to any crystallographic axes.

This representation can be extended: for example in the case of ionic solids the charge on each ion would be a necessary parameter for any energy calculation and

would be represented thus:

$$atoms = \begin{pmatrix} x_1 & y_1 & z_1 & q_1 \\ x_2 & y_2 & z_2 & q_2 \\ . & . & . & . \\ . & . & . & . \\ x_n & y_n & z_n & q_n \end{pmatrix}$$

This could be extended to an arbitrary number of parameters such as parameters for empirical potentials, labels for symmetrically distinct ions of the same species etc.

2.1 Building a dislocation

The model might be expected to start in the same way as Peierls; bringing together two half crystals as shown in Figure 1.4a and simply allowing the structure to relax, leaving all the atomic positions as free variables. However there are two reasons to apply constraints to the atomic coordinates: firstly constraints reduce the number of parameters to search and secondly an unconstrained global optimisation might remove the dislocation entirely. This would create a perfect crystal, which would have a lower energy than a dislocated crystal. To achieve this a displacement field based on initial atomic coordinates is used to find a final atomic configuration.

For a given value of α, there will be an initial configuration of atoms defined by two half crystals brought together at a slip plane with some relative displacement between them defined by α and the Burgers vector. The core of the dislocation is taken to be the line where $x, y = 0$. The position of the core with respect to the lattice of the half crystals is defined by α, usually with $\alpha = 0$ defining the configuration in which the extra half-plane of atoms aligns with the dislocation core, as shown in Figure 1.4b.

The final, in the sense of ready to be evaluated energetically rather than op-

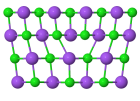

timised, configuration is the combination of the initial positions and an array of displacements defined by some displacement field, $\boldsymbol{\delta}(x_0, y_0, z_0)$, i.e.:

$$\mathbf{r}_i = \mathbf{r}_i^0 + \boldsymbol{\delta}(\boldsymbol{r}_i^0) \tag{2.3}$$

where $\mathbf{r}_i$ is the position vector defining the final position of the ith atom, $\mathbf{r}_i^0$ is the vector defining the initial position of the ith ion and $\boldsymbol{\delta}$ is a vector displacement field.

2.1.1 Defining the initial atomic positions

Firstly we must define the initial positions of the atoms in the half crystals. In the Peierls model the material was assumed to be a simple orthorhombic lattice; i.e. a misaligned bond across the slip plane has a minimum energy when the bond is normal to the slip plane. To consider the effects of the particular structure the atomic configuration must be generated from the lattice and motif of the perfect crystal.

To create a crystal conveniently oriented with respect to the Cartesian reference axes and the crystal slip system, unconventional unit cells were defined. Directions and planes defined relative to the unconventional or dislocation cell will be marked prime, e.g. $[1\,0\,0]'$. The Burgers vector $\mathbf{b}$ is taken to be the $[1\,0\,0]'$, the shortest slip plane normal that is a full lattice vector is taken to be $[0\,1\,0]'$ and the $[0\,0\,1]'$, parallel to the line vector, is the shortest lattice vector that is perpendicular to both the Burgers vector and the slip plane normal and its sign is such that the axes are right handed. Filling space by combining a motif and a lattice defined according to these axes is convenient because most of the mathematical results of dislocation theory, stress and strains fields etc., are defined taking x, y and z parallel to $[1\,0\,0]'$, $[0\,1\,0]'$, $[0\,0\,1]'$ respectively.

For example the NaCl $<1\,\bar{1}\,0>\{1\,1\,0\}$ slip system gives a new unit cell aligned with the slip system:

$$
\begin{aligned}
[1\,0\,0]' &= {}^1\!/_2[1\,1\,0] && \parallel \mathbf{b} \\
[0\,1\,0]' &= {}^1\!/_2[1\,\bar{1}\,0][c] && \parallel \mathbf{d} \\
[0\,0\,1]' &= [0\,0\,1] && \parallel \mathbf{l}
\end{aligned}
$$

where $\mathbf{l}$ is the line vector of the dislocation.

The atoms in this non-conventional unit cell are:

$$
motif = \begin{pmatrix}
0 & 0 & 0 & +1 \\
{}^1\!/_2 & {}^1\!/_2 & {}^1\!/_2 & +1 \\
0 & 0 & {}^1\!/_2 & -1 \\
{}^1\!/_2 & {}^1\!/_2 & 0 & -1
\end{pmatrix}
$$

where a $+1$ in the final column denotes the positive charge of a sodium ion and a -1 denotes the negative charge of a chloride ion.

Similarly the NaCl $<1\,\bar{1}\,0>\{0\,0\,1\}$ slip system is defined by the unit cell:

$$
\begin{aligned}
[1\,0\,0]' &= {}^1\!/_2[1\,1\,0] && \parallel \mathbf{b} \\
[0\,1\,0]' &= [0\,0\,1] && \parallel \mathbf{d} \\
[0\,0\,1]' &= {}^1\!/_2[1\,\bar{1}\,0] && \parallel \mathbf{l}
\end{aligned}
$$

and the atoms are:

$$
motif = \begin{pmatrix}
0 & 0 & 0 & +1 \\
{}^1\!/_2 & {}^1\!/_2 & {}^1\!/_2 & +1 \\
{}^1\!/_2 & 0 & {}^1\!/_2 & -1 \\
0 & {}^1\!/_2 & 0 & -1
\end{pmatrix}
$$

These unit cells are shown in relation to the conventional cell in Figure 2.1. With these unit cells we can convolve the motif with a lattice to generate an initially perfect crystal defined with respect to Cartesian axes aligned with the slip system. Two offsets are then applied; firstly the half crystal below the slip plane, which is defined by $y < 0$, will be offset in the positive x direction by $b/2$ and then the entire crystal is offset to put the dislocation core in the desired location.

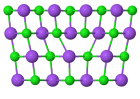

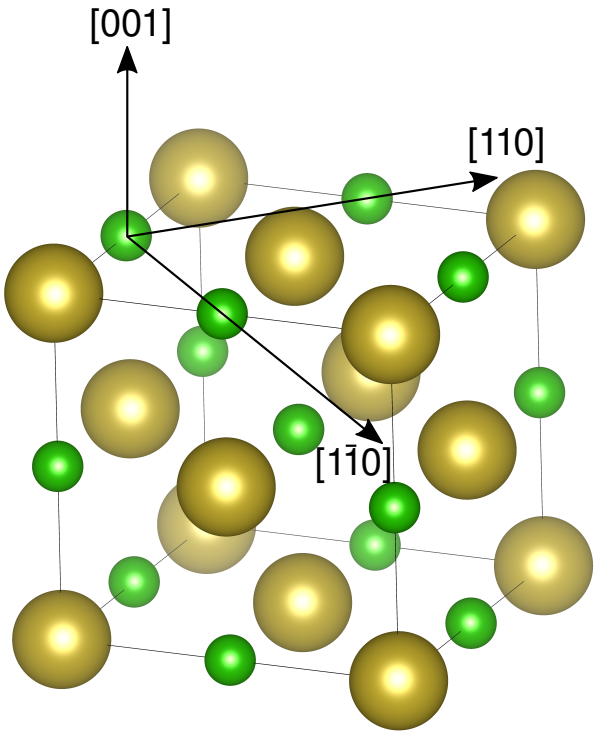

(a) The conventional unit cell of sodium chloride with the salient slip directions and plane normals highlighted.

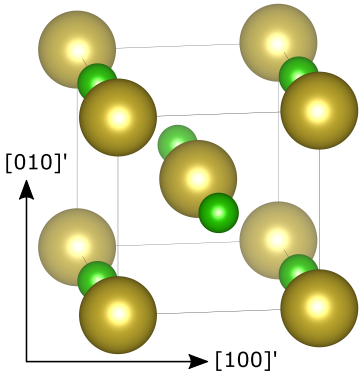

(b) The sodium chloride unit cell best aligned with the <1 1 0>{1 $\bar{1}$ 0} slip system. The new [100]' and [010]' axes are parallel to the to the {1 1 0} and {$\bar{1}$ 1 0} axes of the conventional unit cell respectively.

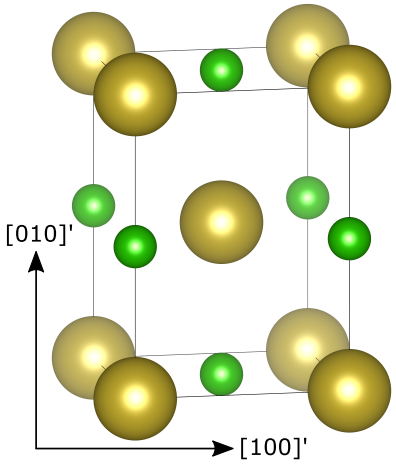

(c) The sodium chloride unit cell best aligned with the <1 1 0>{0 0 1} slip system. The new [100]' and [010]' axes are parallel to the to the {1 1 0} and {0 0 1} axes of the conventional unit cell respectively.

Figure 2.1: Possible unit cells for sodium chloride showing the conventional unit cell and two unconventional unit cells with the new crystallographic axes aligned to slip system, i.e. the Burgers vector and slip plane normal. Graphics prepared with VESTA [74].

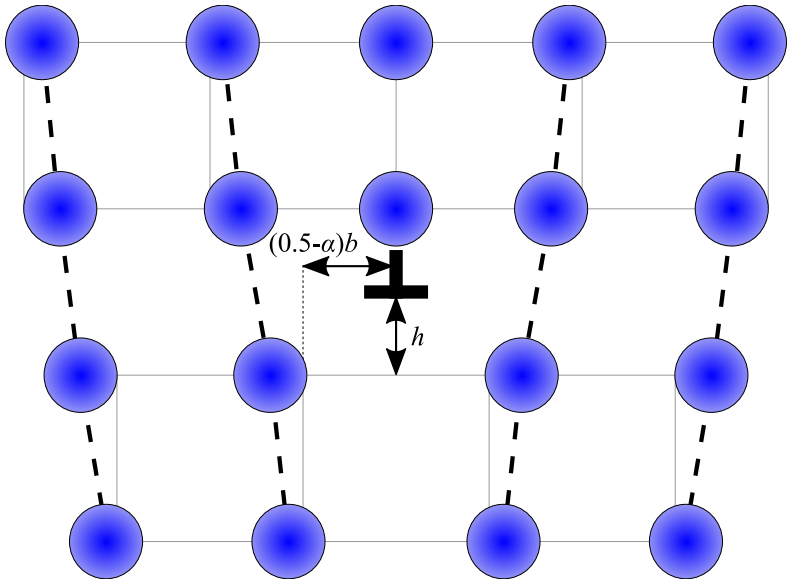

Figure 2.2: The offsets applied to the initial atomic configuration to build a dislocation with its core centred on the correct position. The horizontal offset, i.e. parallel to the slip plane, is defined with respect to the lower half of the crystal.

The x position is defined by an offset along the slip direction of αb, where α is a variable. The position of the core normal to the slip planes might be expected to be fixed by symmetry, in the case of NaCl the core must be at a height of $d/4$ in order to be halfway between the two (0 2 0) layers, but it is not inconceivable that this height might vary in some crystals.

The initial positions of the atoms in the dislocated crystal are related to those of an initially perfect crystal by:

$$\boldsymbol{r_i^0} = \boldsymbol{r_i^{\text{perfect}}} + \begin{cases} [-\alpha b, h, 0] & \text{if } y_i^{\text{perfect}} > 0 \\ [b(1/2-\alpha), h, 0] & \text{if } y_i^{\text{perfect}} < 0 \end{cases} \tag{2.4}$$

The offset to the atomic coordinates in $-\alpha b$ such that as α increases the dislocation motion is in the positive x direction. The variable h defines the height (i.e. position normal to the slip plane) of the dislocation core with respect to the unit cell. Its value may be fixed by symmetry. These offsets are shown schematically in Figure 2.2

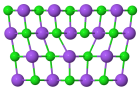

2.1.2 Displacement fields

A suitable displacement field is required. First we can take a Volterra dislocation, which in a continuous isotropic elastic medium has a displacement field [108]:

$$u = \frac{b}{2\pi}\left[\arctan\left(\frac{x}{y}\right) + \frac{xy}{2(1-\nu)(x^2+y^2)}\right] \tag{2.5a}$$

$$v = -\frac{b}{2\pi}\left[\frac{1-2\nu}{4(1-\nu)}\ln(x^2+y^2) + \frac{x^2+y^2}{4(1-\nu)(x^2+y^2)}\right] \tag{2.5b}$$

where u and v are the components of the displacement field parallel to x and y respectively, x is the initial position parallel to the Burgers vector, y is the initial position parallel to the slip plane normal, b is the magnitude of the Burgers vector and ν is the Poisson ratio of the material. The terms all converge to fixed values at large x or y except the logarithmic component of v. This represents the bending of a single crystal that arises from the introduction of an extra half plane [108].

This formulation of the displacement field and subsequent solution for an isotropic elastic continuum is discontinuous, diverging at $r = 0$, where $r = \sqrt{x^2+y^2}$. To remove the discontinuity Eshelby [106] proposed considering a single dislocation to be composed of a continuous distribution of dislocations with infinitesimal Burgers vectors, the integral of which yields the Burgers vector of the full dislocation.

By considering the local strains (a normal strain parallel to the slip plane) due to this distribution, the stress on the slip plane can be found. By applying a force balance condition with the stress arising due to the misalignments, the displacements at the slip plane can be found, following the arguments laid out in [34].

Let $\mathbf{b}'dx'$ be the Burgers vector of an infinitesimal dislocation lying between x' and $x' + dx'$. The dislocation corresponds to a displacement of $-2(du/dx)dx'$. The total Burgers vector can be found by integration:

$$b = \int_{-\infty}^{\infty} b'(x')\ \mathrm{d}x' = -2\int_{-\infty}^{\infty}\left(\frac{\mathrm{d}u}{\mathrm{d}x}\right)_{x=x'}\ \mathrm{d}x' \tag{2.6}$$

The shear stress due to a Volterra dislocation is [109]:

$$\sigma_{xy}^{\text{Volterra}} = \frac{\mu b}{2\pi(1-\nu)} \frac{x(x^2-y^2)}{(x^2+y^2)^2} \tag{2.7}$$

where x relates to the the core of the single dislocation, centred on the origin, with Burgers vector b.

The shear stress on the slip plane due to a single Volterra dislocation is found, by setting $y = 0$ and substituting for b, to be:

$$\sigma_{xy}^{\text{Volterra}}(x,0) = -\frac{\mu}{2\pi(1-\nu)} \int_{-\infty}^{\infty} \frac{b'}{x-x'}\, \mathrm{d}x' = \frac{\mu}{\pi(1-\nu)} \int_{-\infty}^{\infty} \frac{1}{x-x'} \left(\frac{\mathrm{d}u}{\mathrm{d}x}\right)_{x=x'} \mathrm{d}x' \tag{2.8}$$

where $x - x'$ is the distance between some point x and the infinitesimal dislocation at x'.

At the minimum energy position the net stress on the slip plane, i.e all $(x, 0)$, vanishes, so there must be a balancing stress arising from the misalignment of the material across the slip plane. By analogy with Frenkel [33]:

$$\sigma_{xy}^{\text{misalignment}}(x,0) = C \sin\left(\frac{2\pi\phi}{b}\right) \tag{2.9}$$

or in terms of the displacements either side of the slip plane:

$$\sigma_{xy}^{\text{misalignment}}(x,0) = -C \sin\left(\frac{4\pi u}{b}\right) \tag{2.10}$$

If Hooke's law is satisfied at small strains we can write:

$$\sigma_{xy}^{\text{misalignment}}(x,0) = 2\mu\varepsilon_{xy} = \frac{\mu\phi}{d} \tag{2.11}$$

We can combine Equation 2.8 and Equation 2.11 to give an integral equation thus:

$$\int_{-\infty}^{\infty} \frac{1}{x-x'} \left(\frac{\mathrm{d}u}{\mathrm{d}x}\right)_{x=x'} \mathrm{d}x' = \frac{b(1-\nu)}{2d} \sin\left(\frac{4\pi u}{b}\right) \tag{2.12}$$

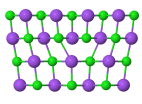

A solution is [106, 109]:

$$u(x) = -\frac{b}{2\pi}\arctan\left(\frac{x}{w}\right) \tag{2.13}$$

where w is the half width of the dislocation and, for an isotropic elastic solid, has the value:

$$w = \frac{d}{2(1-\nu)}. \tag{2.14}$$

Equation 2.13 satisfies the boundary condition that $u(\infty) = -u(-\infty) = -b/4$. $x = w$ gives $u(w) = 1/2\,u(\infty)$, i.e. in the region $-w < x < w$ the disregistry across the slip plane is greater than half the maximum that occurs at $x = 0$.

The two dimensional case gives a displacement field [106, 110, 111]:

$$u(x,y) = \frac{b}{2\pi}\left(\arctan\left[\frac{y + w\frac{|y|}{y}}{x}\right] - \frac{\pi}{2}\frac{|y|}{y}\frac{|x|}{x}\right) + c_1\frac{xy}{x^2 + (y + w\frac{|y|}{y})^2} \tag{2.15a}$$

$$v^y(x,y) = c_2\frac{y(y + w\frac{|y|}{y})}{x^2 + (y + w\frac{|y|}{y})^2} + c_3\ln\left|\frac{x^2 + (y + w\frac{|y|}{y})^2}{b^2}\right| \tag{2.15b}$$

The final atomic configuration is then defined by:

$$\boldsymbol{r}_i = \boldsymbol{r}_i^0 + [u_i\,\hat{\mathbf{i}},\ v_i\,\hat{\mathbf{j}},\ 0\,\hat{\mathbf{k}}] \tag{2.16}$$

These terms can be interpreted physically: the arctan term is the same as in the original Peierls treatment, representing displacements along the slip plane that alter the local misalignment across the slip plane. The terms with the prefactors c_1 and c_2 represent shear strains: the xy and yx shears respectively. The logarithmic term, with the prefactor c_3, represents the bending of the entire crystal that must arise from the introduction of an extra half plane of atoms. This logarithmic term does not converge to a constant value at large x or y, but this is consistent with this physical interpretation as a bend in the lattice planes [109].

Hence the parameters have physical interpretations: the width of the dislocation still defines the region with large disregistries, while c_1 and c_2 define the magnitude of displacements associated with shear strains around the dislocation core and c_3

defines the magnitude of the bending of a crystal that must arise from the introduction of an extra half plane of atoms. To illustrate the displacements produced by these different terms some exaggerated (by a factor of ten from that predicted for an isotropic elastic medium) dislocation configurations are shown in Figure 2.3.

The inclusion of $v(x, y)$ in the displacement field means that there will always be some finite displacement normal to the slip plane. This is expected and is associated with phenomena such as pressure dependent yield stress [114]. These displacements might also be responsible for the normal strains observed around line defects in layered crystals that have been ascribed to a new class of defect called ripplocations [115].

For a continuous isotropic elastic medium the various parameters in Equation 2.15 are found analytically to have fixed values for the lowest energy dislocation. The half-width, w, takes the same value as in Equation 2.14 and the three other parameters are defined by:

$$c_1 = \frac{b}{4\pi(1-\nu)} \tag{2.17a}$$

$$c_2 = \frac{b}{4\pi(1-\nu)} \tag{2.17b}$$

$$c_3 = -\frac{b(1-2\nu)}{8\pi(1-\nu)}. \tag{2.17c}$$

The terms of the form $|x|/x$ and $|y|/y$ are to give all the terms the right sense in the right regions of space, i.e. above and below the slip plane in y and either side of the dislocation in x. This reduces to the simpler solution in Equation 2.13 if only the atoms adjacent to the slip plane are considered. This form is useful because it is continuous and finite for all values of x and y.

This gives a displacement field for a general material which has four parameters: the width, w, and the scaling factors, c_1, c_2 and c_3. These parameters are varied to find the lowest energy dislocation. If the energy is calculated by an atomistic model, rather than by continuum elasticity, then there is no analytical solution for these parameters. Instead those values that minimise the energy are taken to be the

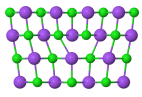

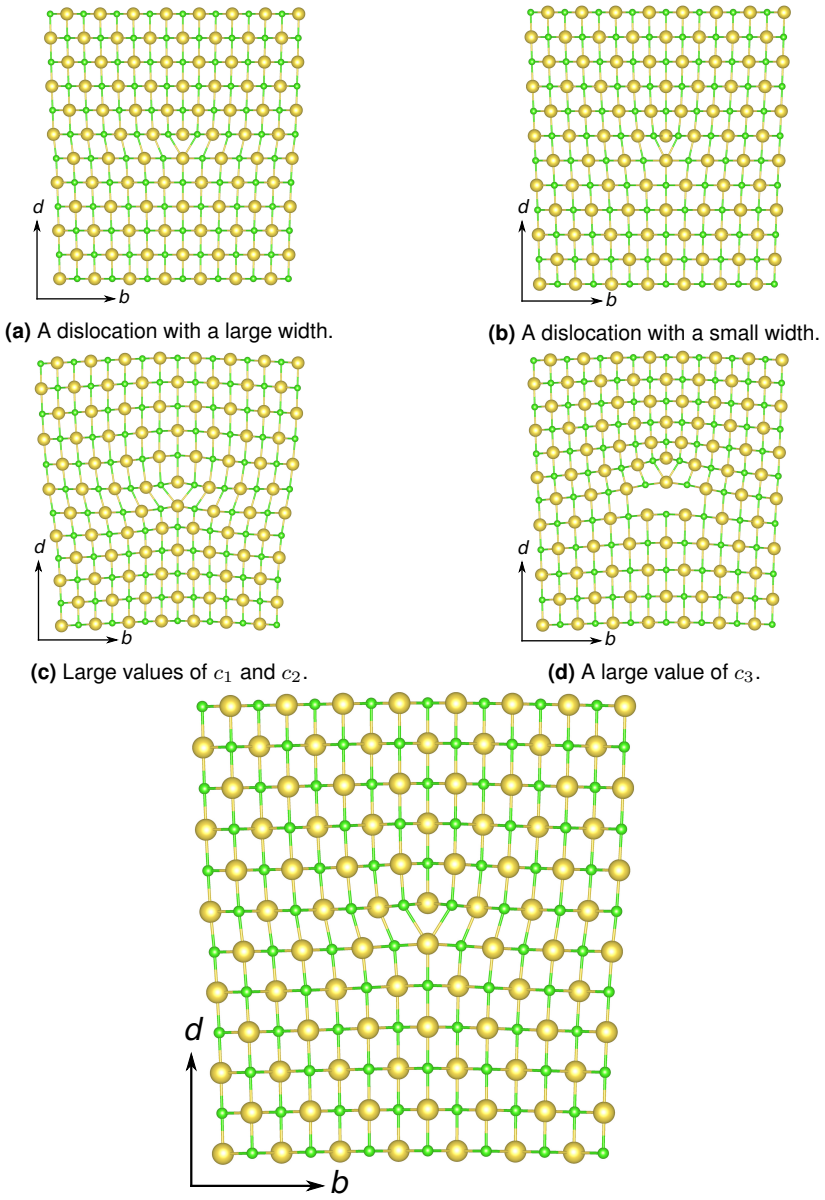

(a) A dislocation with a large width.

(b) A dislocation with a small width.

(c) Large values of c_1 and c_2.

(d) A large value of c_3.

(e) A "typical" configuration, taken to be the dislocation structure predicted for a Volterra dislocation in a continuous elastic medium using the elastic constants of NaCl.

Figure 2.3: Various configurations of sodium chloride <1 1 0>{0 0 1} dislocations demonstrating the effects of the parameters of the displacement field defined in Equation 2.15, w, c_1, c_2 and c_3. Typical parameters are taken to be those predicted for an isotropic elastic material as given in Equations 2.14 and 2.17, giving 1.78 Å, 0.40 Å, 0.40 Å and –0.12 Å respectively for sodium chloride. Exaggerated values were ten times that. Calculated with $\nu = 0.207$ and $a = 5.644$ Å [112, 113]. Graphics prepared with VESTA [74].

correct solution.

A final note on the parametrisation of the dislocation structure is that the values c_1, c_2 and c_3 are not constrained by any assumptions made so far. The purely isotropic case described above the parameters c_1, c_2 are positive and c_3 is negative, but there is no physical reason they cannot have a different sign. However a negative value of the width is not physically meaningful in this formulation. A negative width reintroduces the discontinuity at which displacements would diverge (in fact it would introduce two, one either side of the slip plane). Hence the constraint that $w > 0$ is applied, but c_1, c_2 and c_3 are allowed to vary freely.

2.2 Evaluating the dislocation energy

Since there are insufficient boundary conditions to completely define a dislocation's atomic configuration with even four parameters, the energy of the dislocation is the only way to identify a correct or true configuration. Hence the energy of atomic configurations must be characterised. One method to calculate the energy is to try and replicate the model based on elastic energy in the two half crystals and misalignment energy across the slip plane. There is also the opportunity to calculate the full strain tensor and along with single crystal elastic constants the effects of elastic anisotropy can be taken into account.

Another would be to use empirical potentials similar to those used in molecular dynamics, allowing the exploration of dislocation properties in materials that are not well modelled by elasticity or where more can be learned by other methods. Ionic solids or compound semiconductors are examples of materials where more physical insight is possible with interatomic potentials that relate more closely to the nature of the crystal chemistry than elastic constants.

The first approach builds on the original approach of Peierls [30] and Nabarro [31] and explains how the dislocation is stable due to a balancing of two forces. There is a force that attempts to spread the dislocation out into a planar defect, which arises due to the elastic stored energy in the bonds either side of the slip plane.

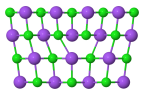

The elastic energy would be zero in the case of a planar defect, i.e. an infinitely wide dislocation. Another force tends to decrease the dislocation width, arising from the misfit or misalignment across the slip plane. The misalignment energy would be a maximum for the planar defect where the entire slip plane is misaligned and would decrease monotonically as the width decreases.

Using an elastic model to find the energy has a number of advantages. A two dimensional model is sufficient since the condition of plane strain can be applied. If elastic theory can be applied at the scale of the unit cell then displacements need only be considered between unit cells rather than within them, which simplifies the model considerably.

2.2.1 Strain energy

The elastic energy can be easily calculated for a small volume if the strain and the elastic tensor are known. A good discussion of tensors and elasticity is given by Kelly and Knowles [116, 117] and a discussion of elasticity in the context of dislocation theory is given by Hirth and Lothe [118]. The salient results are drawn together here.

Hooke's Law can be written as a tensor relationship using the Einstein summation convention:

$$\sigma_{ij} = c_{ijkl}\varepsilon_{kl} \tag{2.18}$$

where σ_{ij} is the stress tensor, c_{ijkl} is the elastic tensor defining the properties of the material and ε_{kl} is the strain tensor. Strain is defined, for $i = j$, by:

$$\varepsilon_{ii} = \frac{\partial u_i}{\partial x_i} \tag{2.19}$$

and for $i \neq j$ by:

$$\varepsilon_{ij} = \frac{1}{2}\left(\frac{\partial u_i}{\partial x_j} + \frac{\partial u_j}{\partial x_i}\right). \tag{2.20}$$

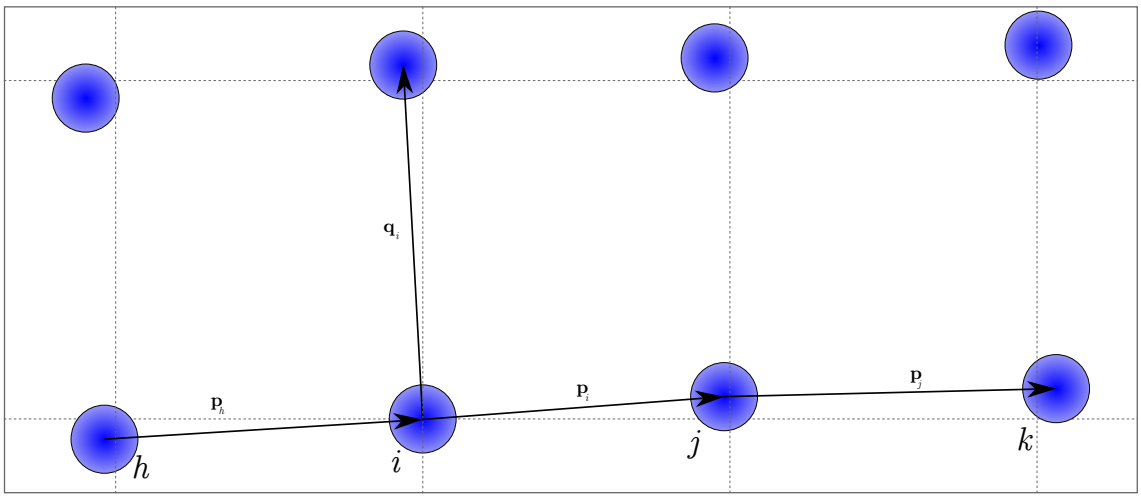

Figure 2.4: The bonds that are considered for the ith atom in a region of crystal away from the slip plane; there is one bond to the nearest neighbour in the positive x direction, $\mathbf{p}_i$, and one to the nearest neighbour in the positive y direction, $\mathbf{q}_i$, to avoid double counting.

If Hooke's law holds then the stored elastic energy per unit volume is:

$$u_{\text{elastic}} = {}^1\!/_2\, \sigma_{ij}\varepsilon_{ij} = {}^1\!/_2\, c_{ijkl}\varepsilon_{ij}\varepsilon_{kl}. \tag{2.21}$$

Hence to find the elastic energy we must evaluate $\partial u_i/\partial x_j$ for $i, j = 1, 2, 3$. Assuming a primitive orthogonal lattice, estimating the components of strain is not difficult. The condition of plane strain constrains $\varepsilon_{ij} = 0$ for i or $j = 3$. In the 1–2 (or x–y) plane the strains can be identified from the vectors between neighbouring unit cells. For simplicity a primitive lattice is assumed and these vectors can be conceived of as bonds.

For this simple case two bonds are identified for each atom, one to the nearest neighbour in the x direction and one to the nearest neighbour in the y direction as shown in Figure 2.4. The simplest estimate of the stress components is:

$$\begin{aligned} \left.\frac{\partial u}{\partial x}\right|_i &= \frac{\mathbf{p}_i \cdot \hat{\mathbf{i}}}{b} & \left.\frac{\partial u}{\partial y}\right|_i &= \frac{\mathbf{q}_i \cdot \hat{\mathbf{i}}}{d} \\ \left.\frac{\partial u}{\partial y}\right|_i &= \frac{\mathbf{q}_i \cdot \hat{\mathbf{j}}}{d} & \left.\frac{\partial u}{\partial x}\right|_i &= \frac{\mathbf{p}_i \cdot \hat{\mathbf{j}}}{b} \end{aligned} \tag{2.22}$$

However there is a problem with this formulation. This assumes that every bond would, in equilibrium, be parallel to either the x or the y axis. This assumption

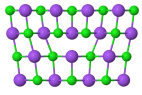

is valid for the original Peierls model in which only displacements parallel to the x direction were considered but the logarithmic term here represents a change in lattice orientation with position.

Addressing this requires some estimate of the local lattice orientation. The logarithmic term in Equation 2.15, representing the bending of the lattice, means that far from the dislocation core the lattice can be tilted to a large angle with respect to the slip direction at the core. If the same reference axes are used everywhere, this bending results in an ever increasing strain, and therefore ever increasing strain energy away from the core. Using a local lattice orientation as the reference frame to calculate the strain means that strains will be largest near the core, as expected.

There are many possible ways of estimating the local lattice orientation. One possible method is to take the average of the neighbouring bonds so for the atom labelled i shown in Figure 2.4 the ideal orientation of $\mathbf{p}_i$ would be parallel to $(\mathbf{p}_h+\mathbf{p}_j)$. The ideal orientation for $\mathbf{q}_i$ can be taken to be at 90° to this. Therefore $\hat{\mathbf{i}}$ and $\hat{\mathbf{j}}$ in Equation 2.22 can be replaced with

$$\begin{aligned}\hat{\mathbf{i}}' &= \frac{(\mathbf{p}_h + \mathbf{p}_j)}{|\mathbf{p}_h + \mathbf{p}_j|} \\ \hat{\mathbf{j}}' &= \hat{\mathbf{i}}' \times \hat{\mathbf{k}}\end{aligned} \tag{2.23}$$

and the strain tensor can be calculated for each atom/unit cell, and hence the strain energy for each unit cell.

2.2.2 Misalignment energy

At the slip plane the method above will break down. For an atom immediately below the slip plane the identification of the nearest neighbour above the slip plane can be ambiguous, or can leave some atoms multiply bonded and others unbonded. The nearest neighbour will also change as the dislocation moves. Figure 2.5 shows an possible configuration around a dislocation core that would result in this kind of problem. Considering the atom m, it can be seen that it is further from both

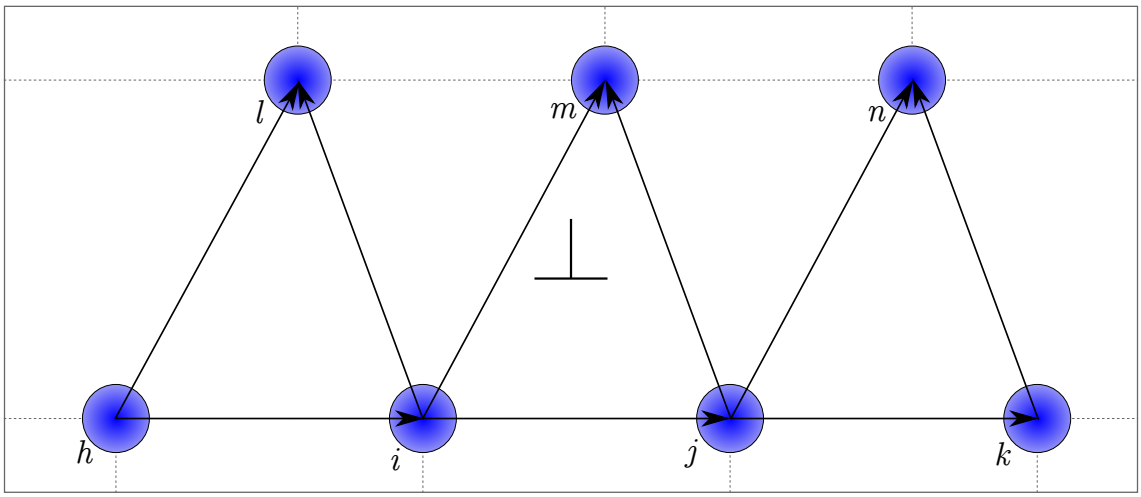

(a) The initial positions of atoms either side of the slip plane..

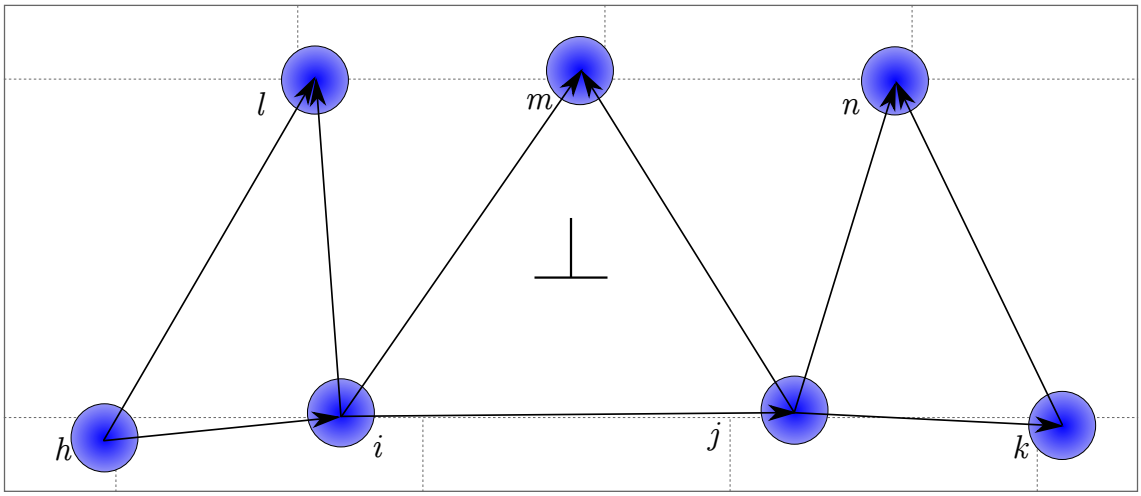

(b) The final positions of the atoms either side of the slip plane.

Figure 2.5: The slip plane before and after the application of the displacement field in the vicinity of the dislocation core. If we consider only nearest neighbours then the atom labelled m would be unbonded while others, like n would be bonded twice. Ambiguities can also arise when neighbours are equidistant and the neighbours would also change as the dislocation moved using a nearest neighbours model. Instead the two nearest neighbours across the slip plane are considered, as shown this results in a forward bond and a backward bond. Notice the changing orientation of the slip plane in the dislocated crystal.

atom i and atom j than their other neighbours, l and n, and so atom m would be unbonded in a simple nearest neighbour model. The atom n might be bonded twice in such a model.

A less arbitrary method is to use the initial positions and assume that the ith atom can be bonded to two atoms in the layer above the slip plane. Since initially the horizontal spacing between atoms is b for all atoms the two atoms must be within an interval $x_i^0 - b < x \leq x_i^0 + b$, bonds can be identified as shown in Figure 2.5a. The energy of the two bonds is averaged to avoid a double counting error.

There are several methods to calculate the energy of the misaligned bonds. The

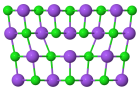

simplest is to use the Frenkel approximation which, for an isotropic elastic material is:

$$U_i^{\text{mis}} = \frac{Gb^2}{4\pi^2}\left[\frac{d}{b}\right]\left[1-\cos\left(\frac{2\pi\phi}{d}\right)\right] \tag{2.24}$$

which in terms of single crystal elastic constants takes $G = C_{66}$ (in Voigt notation see [117]). The 66 term is used if the elastic tensor is in the frame of reference of the slip system, with the 1 axis parallel to the slip direction, the 2 axis parallel to the slip plane normal and the 3 axis parallel to the line vector. C_{66} is thus always the relevant stiffness constant regardless of the material symmetry.

A more complete method for the calculation of the energy makes use of the generalised stacking fault energy. Density functional theory can be used to calculate the energy of a stacking fault at an arbitrary misalignment. This is calculated by applying a displacement to two half crystals in a DFT simulation with periodic boundary conditions which introduces two opposing planar faults. The displacement is applied along the Burgers vector and the atoms are allowed to relax perpendicular to that displacement. Although the displacement field does not include any lateral motion (i.e. parallel to the dislocation line), allowing the DFT simulation of the stacking faults to relax laterally means that the energetic implications of lateral motion are included in the misalignment potential, although with an implicit assumption that the strains along the line vector do not extend beyond the slip plane.

The energy changes with respect to a perfect crystal were considered and fitted with a simple empirical function:

$$\gamma(\phi) = \sum_{m=1}^{M} C_m\left[1-\cos\left(\frac{2m\pi\phi}{b}\right)\right] \tag{2.25}$$

where ϕ is the misalignment in the same units as the Burgers vector b, m is an integer from 1 to M, and C_m are coefficients fitted by a least-squares method. This is in units of $\mathrm{J\,m^{-2}}$, so a factor of b must be applied to convert to a line energy in $\mathrm{J\,m^{-1}}$.

2.2.3 Empirical potentials

Some materials can be described in a more physically insightful way than linear elasticity; as described in section 1.5, empirical potentials have been developed for the field of molecular dynamics to be computationally convenient while at the same time approximating reality to a sufficient degree to gain insight into a system [83]. Such potentials are usually fitted to measured properties such as lattice energies and elastic constants.

One way to incorporate such potentials into the Peierls model described here is to write a simple Python implementation of the potentials using the SciPy and NumPy packages and associated tools [92, 119–121]; another way is to use the Atomic Simulation Environment [122] or the Python interface to the LAMMPS software package [95, 96].

The ionic solids were investigated using the Lennard-Jones potential:

$$\phi_{ij}(r_{ij}) = 4\varepsilon_{ij}\left[\left(\frac{\sigma_{ij}}{r_{ij}}\right)^{12} - \left(\frac{\sigma_{ij}}{r_{ij}}\right)^{6}\right] \tag{2.26}$$

where ε_{ij} is the depth of the energy well and σ_{ij} is the radius at which the energy is equal to zero or in the A–B form:

$$\phi_{ij}(r_{ij}) = \frac{A_{ij}}{r_{ij}^{12}} - \frac{B_{ij}}{r_{ij}^{6}} \tag{2.27}$$

where $A_{ij} = 4\varepsilon_{ij}\sigma_{ij}^{12}$ and $B_{ij} = 4\varepsilon_{ij}\sigma_{ij}^{6}$. The energy for any two atoms is then:

$$U_{ij}(r_{ij}) = \frac{1}{4\pi\varepsilon_0}\frac{q_i q_j}{r_{ij}} + \frac{A_{ij}}{r_{ij}^{12}} - \frac{B_{ij}}{r_{ij}^{6}} \tag{2.28}$$

where ε_0 is the permittivity of free space.

The Lennard-Jones potential has been chosen as a simple way to implement the application of empirical potentials. Fitted parameters are readily available [123] and the potential is applicable to a class of materials for which the dislocation properties are not fully understood, the alkali halides.

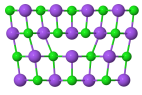

Ion	σ_i/Å	ε_i/J mol^{-1}
Li^+	1·715	241·25
Na^+	2·497	327·44
K^+	3·184	494·97
Rb^+	3·302	1006·25
Cs^+	3·440	2097·44
F^-	3·954	27·05
Cl^-	4·612	104·68
Br^-	4·812	150·46
I^-	5·197	176·56

Table 2.1: Parameters used for Lennard-Jones calculations from [123].

The parameters used for the Lennard-Jones potential are shown in Table 2.1. These were fitted to the lattice properties of the solid salts. They are calculated for each ion individually, to best reproduce lattice properties, and must be combined according to Lorentz-Berthelot rules:

$$\begin{aligned} \varepsilon_{ij} =& \sqrt{\varepsilon_i \varepsilon_j} \\ \sigma_{ij} =& \frac{\sigma_i + \sigma_j}{2} \end{aligned} \tag{2.29}$$

A simple implementation without modification for computational ease, such as cut off distances, is given in [107] and an example input file is given for LAMMPS in section A.3. LAMMPS input files are described in the LAMMPS documentation [96].

2.2.4 Optimisation of the dislocation structure

Given one of the above cases, or a similar one, that provides energy as a function of a small number of parameters, an optimisation routine is required. The original version of this Peierls model [37] included a simple binary search to find the width of the dislocation. However for a multi-parameter space this is not appropriate.

Fortunately the open source project SciPy includes implementations of a number of optimisers. The one chosen here was the quasi-Newton method of Broyden, Fletcher, Goldfarb, and Shanno [121, 124], or BFGS. This method uses the first derivative of the energy with respect to the different parameters, and is one of the

class of algorithms known as hill-climbing optimisers, which seek a stationary point.

While the derivative of the energy with respect to the parameters is not simple to find, the atomic positions are defined as smooth functions of the input parameters and the energy is therefore likely to be a smooth function of the atomic positions too. Hence the overall behaviour of the energy as a function of the input parameters should be well suited to a gradient based method. The SciPy implementation of the BFGS algorithm includes the ability to approximate the first derivative numerically.

If it is found that the energy function is not well behaved, SciPy also includes the Nelder-Mead simplex algorithm that does not make use of gradient information. This method calculates the objective function, here the energy, at $n + 1$ points in parameter space where n is the number of parameters. This defines a "simplex", i.e. a triangle in two dimensions, a tetrahedron in three and so on. A search direction is defined along the vector joining the worst of these $n + 1$ points and the centroid of the rest, and a small number of point along this line are trialled. The worst point of the initial simplex is then replaced with an "improved" point and the process repeated [125, 126].

2.2.5 Summary

In this section, the constituent parts of a new Peierls model have been discussed in some detail, including how to practically implement and combine various aspects in a modular fashion. If the model is to be used in a predictive way, it should first be verified against some known benchmarks.

Previous Peierls models have described the observed behaviour of simpler crystals well, from diamond to F.C.C. metals [37, 42], and so this is the natural set of benchmarks against which to test the model. Other experimental benchmarks that could be used to test the model are historical data for the alkali halides [37, 97], since Peierls models have always had problems predicting the differences between slip systems in these phases, and some more recent examples of slip in complex crystals such as cementite [127].

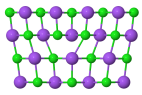

2.3 Results and Discussion

2.3.1 Elastic Energy Calculations

The equilibrium dislocation configuration for a given dislocation position was calculated by optimisation of the dislocation structure with respect to the calculated energy, the sum of the strain energy in the half crystals either side of the slip plane and the misalignment energy in the slip plane. As discussed in section 2.2.4 the choice of optimiser is affected by the behaviour of the function. The BFGS was found to be faster than the Nelder-Mead, though both algorithms produced very similar results, within the tolerance (i.e. the error that can be tolerated) set for the algorithms to terminate. It was found that only a very small error in the result could be tolerated in deciding the algorithm had converged. Tolerating larger errors led to inconsistent results. A relative error of around 1×10^{-7} was usually sufficiently low. This is important because small changes in the energy are being studied.

The variation of the dislocation energy with respect to the dislocation parameters, as defined in Equation 2.15, was investigated. These calculations were performed for a dislocation in copper at $\alpha = 0$. The simulation cell used extended to 800 Burgers vectors from the dislocation core, which is approximately 0.4 µm across the whole simulation.

First the dislocation structure was optimised to find the equilibrium configuration, then the various parameters were varied away from these equilibrium values individually. The results are shown in Figure 2.6.

As expected all the parameters showed a single minimum and the variation was

Parameter	Ideal	Simulated $\alpha = 0$	Simulated $\alpha = 0.5$
w (Å)	1.581	2.441	2.431
c_1 (Å)	0.308	0.36268	0.36270
c_2 (Å)	0.308	0.293070	0.293075
c_3 (Å)	-0.0493	-0.061864	-0.061862
Energy (J/m)	$1.567\,95 \times 10^{-9}$	$1.209\,65 \times 10^{-8}$	$1.209\,63 \times 10^{-8}$

Table 2.2: A comparison of the ideal dislocation parameters and those found by optimising the energy of a simulated dislocation, the ideal values of c_1, c_2, c_3 and w are calculated from the elastic constants using Equation 2.17. The ideal energy is taken to be $^1/_2 Gb^2$.

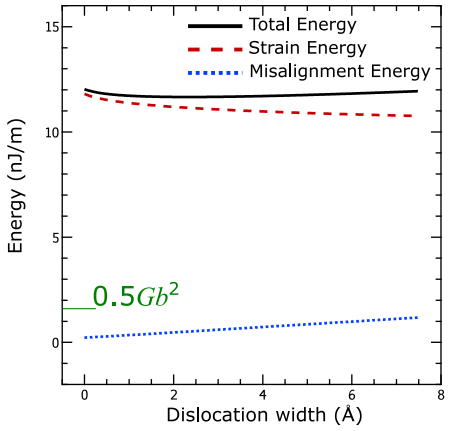

(a) The variation in the dislocation energy with the dislocation width.

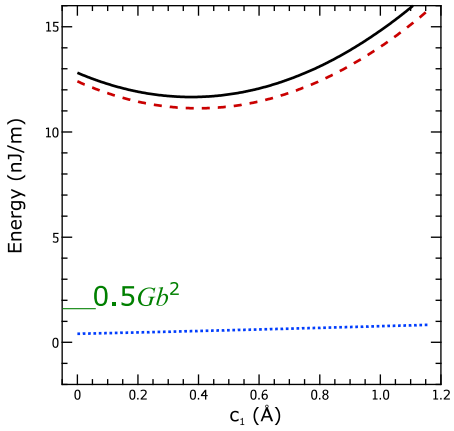

(b) The variation in the dislocation energy with the dislocation parameter $\mathbf{c_1}$.

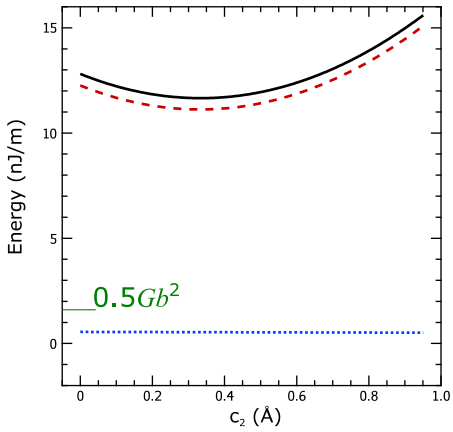

(c) The variation in the dislocation energy with the dislocation parameter $\mathbf{c_2}$.

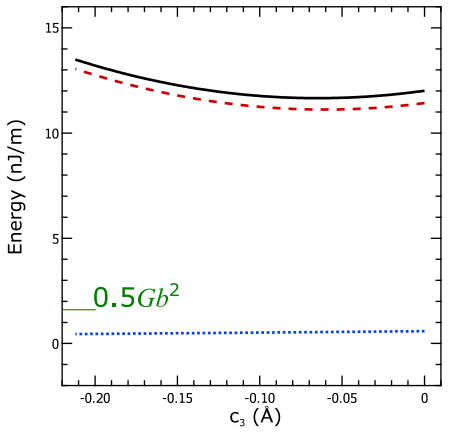

(d) The variation in the dislocation energy with the dislocation parameter $\mathbf{c_3}$.

Figure 2.6: The variation of the calculated energy of a dislocation in copper at the $\alpha = \mathbf{0}$ position, calculated for a simulation extending 0.4 µm from the dislocation core. The parameters are as defined in Equation 2.15. Only one parameter was varied at a time, all the others were held constant at their equilibrium values. The total energy is the solid black line, the strain energy in the two half crystals is the dashed red line and the misalignment energy in the slip plane is the dotted blue line.

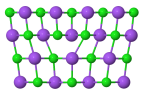

smooth, so a variational approach is applicable and the optimiser is likely to be reliable, i.e. the lowest energy configuration can be said to be the configuration a dislocation would take.

The values of these parameters have simple solutions for the case of an isotropic elastic medium, given in Equation 2.14 and Equation 2.17. These only depend on the Poisson's ratio, which for copper is ∼0.34 [128], and the lattice parameters. These ideal values are compared with the optimised values in Table 2.2. The energy of the dislocation is approximately $4Gb^2$, higher than the $\sim 0.5Gb^2$ that might be expected. However, the values of the dislocation configuration parameters are similar to the ideal values, as calculated from Equation 2.17. The atomistic model differs from the isotropic elastic continuum in that the values of the parameters vary as a function of α and the symmetry between c_1 and c_2, which are equal for an isotropic material, is broken.

The small variations in the values of the dislocation parameters and the dislocation energy, both as relative and absolute values, require that care is taken in the computation not to introduce errors. One example that has already been mentioned is the tolerance, or relative error that can be tolerated before the optimisation is terminated. If the tolerance is not tight enough, this manifests as noise that depends on the initial guess to start the optimisation search, or the exact choices of parameters in the optimisation algorithm. This apparent noise would be deterministic but unpredictable, so would appear random.

Another problem was the precision of the floating point arithmetic. It was found that 64 bit precision was usually sufficient, but some systems, particularly diamond, had such drastically different magnitudes for the strain and misalignment energies that the sum rounded to the strain energy. The dislocation energy would then be wrongly optimised to reduce that term alone. While the strain energy term dominated the line energy for these materials, principally silicon, the changes in the misalignment energy and the changes in the strain energy term were not nearly as different as the values themselves. The problem was addressed by using NumPy's

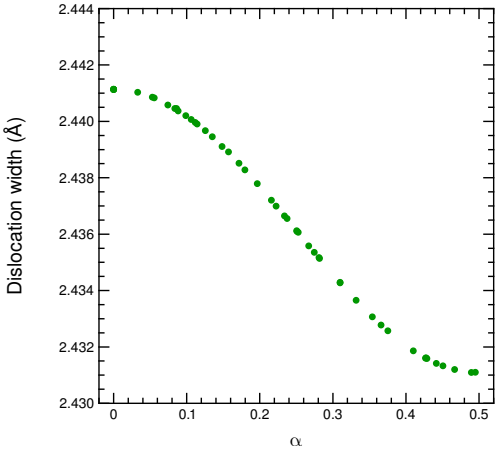

(a) The variation of the dislocation width, w, as a function of α. The width defines the region of the slip plane where the misalignments are greater than half the maximum value.

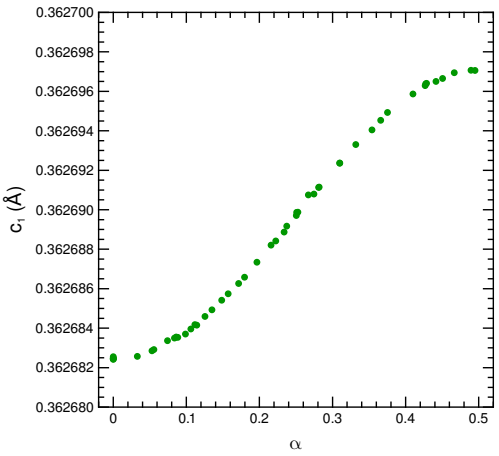

(b) The variation of the dislocation width, c_1, as a function of α. The parameter c_1 represents the magnitude of the xy strains.

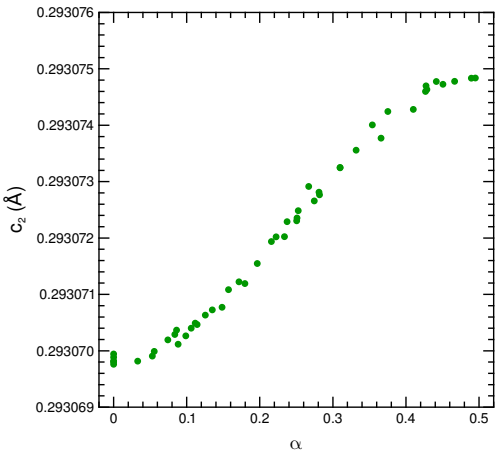

(c) The variation of the dislocation width, c_2, as a function of α. The parameter c_2 represents the magnitude of the yx strains.

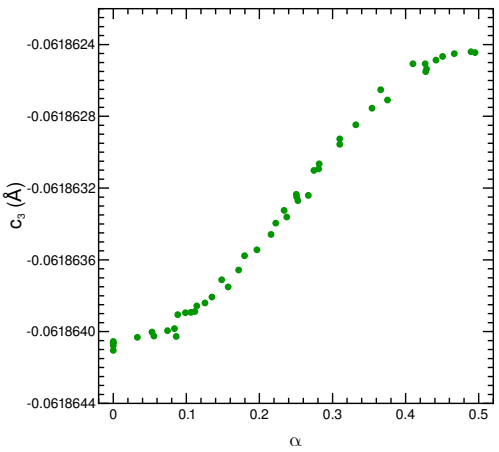

(d) The variation of the dislocation width, c_3, as a function of α. The parameter c_3 represents the magnitude of the bending that arises in a crystal as a result of the introduction of an extra half plane of atoms.

Figure 2.7: The variation of the displacement field configuration parameters with α. Only small changes in the parameters were seen, the largest changes were seen in w and the smallest in $\mathbf{c_3}$. The parameter all vary smoothly and approach $\alpha = \mathbf{0, 0.5}$ with no gradient, as required for equilibrium. Some noise was observed in the value of $\mathbf{c_2}$ and $\mathbf{c_3}$.

128 bit precision.

The variation of the dislocation parameters and the dislocation energy were investigated by randomly sampling α in the range 0 to 0.5 and optimising the dislocation configuration to give the lowest energy. The variation in the dislocation configuration parameters is given in Figure 2.7, while the variation of the total energy is given in Figure 2.8 and the relative changes in the different energy components is shown in Figure 2.9.

An important observation is that the periodicity of the dislocation energy, and indeed the dislocation configuration, predicted by this model is b, not $^{b}/_{2}$ as predicted

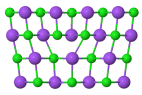

by Peierls [30] and Clegg *et al.* [37]. As discussed in Chapter 1, this is expected based on the symmetry inherent in the model.

Peierls introduced an implicit symmetry by assuming that the dislocation configuration does not change as the dislocation moves and thus predicted a period of $b/2$. The formulation was changed by Huntington [36] to predicted a period of b. The model presented by Clegg *et al.* [37] included an implicit symmetry since motion of atoms was limited to the slip direction and the strain energy was calculated from strains in the atomic bonds rather than as an integral over an elastic medium. This meant that there was no distinction between the atoms above the slip plane and the atoms below the slip plane, and thus no distinction between the $\alpha = 0$ and $\alpha = 0.5$ position. The current model has no such symmetry across the slip plane, due to the logarithmic term in Equation 2.15, and so the periodicity of b is expected.

The dislocation parameters vary smoothly from $\alpha = 0$ to $\alpha = 0.5$ and approach the two equilibrium positions with zero gradient as required by equilibrium. There is some noise in the value of c_2, as shown in Figure 2.7c. This is likely due to the changes in the dislocation parameters being close to the tolerance of the optimisation algorithm. This is not sufficiently noisy to present a problem, but highlights the need for care in deciding the trade off between computational time and the accuracy of the calculated values.

The variation of the energy with α, Figure 2.8, was qualitatively as expected from previous work [37, 42]: a smooth but very small variation in the energy, some five orders magnitude smaller than the value of the dislocation energy. The variation of the two components of the energy was also as expected. This is most easily seen as changes by setting the energy at $\alpha = 0$ to be zero, as shown in Figure 2.9. The strain energy and the misalignment energy vary out of phase with each other, thus the two components of the energy experience larger variations than the total. It is also possible that the relative magnitude of the two components will alter which of the two equilibrium positions is stable and which is unstable.

To undertake further analysis the energy variation can be fitted with a simple

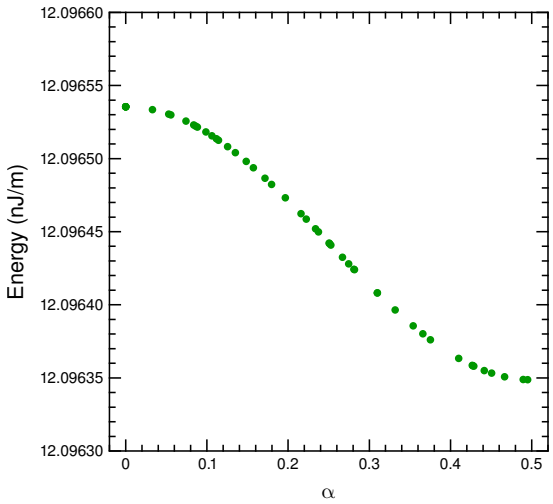

Figure 2.8: The variation of the dislocation energy with position for a dislocation in copper. The results shown are for a model including atoms to a distance of 800 Burgers vectors from the dislocation core, i.e. a distance of ∼300 nm. Note that the changes in energy are small relative to the absolute value of the dislocation energy, at around $1 \times 10^{-5}\, U_{\text{disloc}}$.

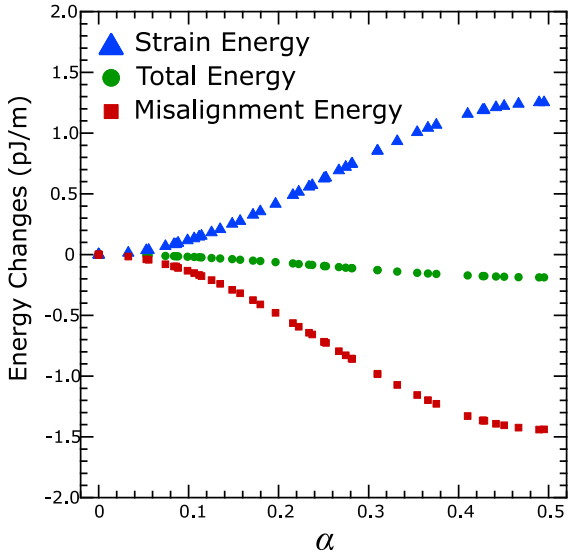

Figure 2.9: The energy changes with position for a dislocation in copper showing the two components of the energy, the strain energy and the misalignment energy, and the total energy. This simulation extended 800 Burgers vectors from the dislocation core, or around 4 µm.

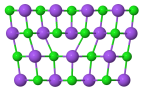

empirical function:

$$U = \sum_{n}^{N} C_n \cos(2\pi n\alpha) \tag{2.30}$$

where C_n are the parameters to be fitted, n is an integer between 0 and N and α is the displacement of the dislocation from the initial position as a fraction of the Burgers vector. Usually it was found that $N = 4$ gave a good fit to the calculated energy variations. Since this is an easily differentiable function, the stress can be calculated in a straightforward manner from the gradient:

$$\tau = \frac{dU}{d\alpha}\frac{1}{lb^2} \tag{2.31}$$

where l is the length of dislocation line and b is the Burgers vector. The gradient is readily calculated by:

$$\frac{dU}{d\alpha} = \sum_{n}^{N} -2\pi C_n \sin(2\pi n\alpha) \tag{2.32}$$

This provides a smooth and differentiable function that both allows for noise in the data and makes calculating the Peierls stress easier. The Peierls stress is the maximum value of the stress, which occurs at the point of maximum gradient $dU/d\alpha$, i.e. where:

$$\frac{d^2U}{d\alpha^2} = \sum_{n}^{N} -4\pi^2 n^2 C_n \cos(2\pi n\alpha) = 0 \tag{2.33}$$

A script was written to do this fitting and gradient calculation automatically; the code is included in an archive which can be found in [107]. An example of this sort of fit is shown in Figure 2.10. For the example of copper above, this yields a Peierls stress of 8.98 MPa or, as a fraction of the shear modulus, $2.54 \times 10^{-4}\,G$. This is approximately 10 times larger than the value estimated by experiment [129]. However, for very soft materials the error in such experiments can be very large.

To characterise the dependence of the model on the volume of crystal modelled, various simulation sizes were modelled for dislocations in copper. The size here is the range about the core of the dislocation in the slip direction and normal to the slip planes, while symmetry was exploited along the dislocation line to model

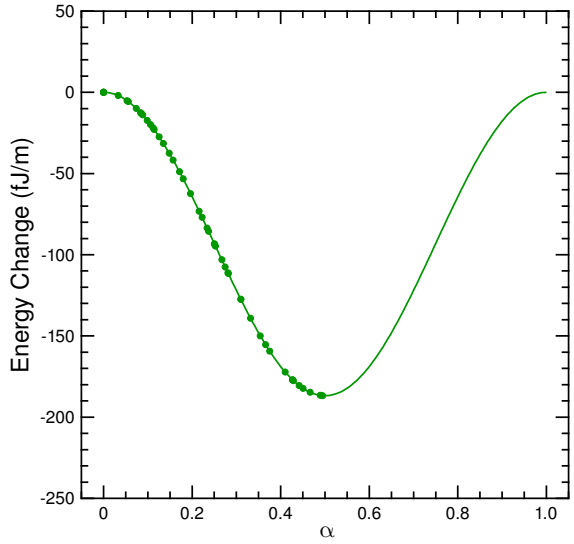

Figure 2.10: Empirical fit to the dislocation energy as it varies with dislocation position using 4 terms. The fit is good, so can be reliably used for further analysis.

only one repeat unit. The resulting simulated crystal therefore has a rectangular cross-section, rather than, say, cylindrical.

The energy and Peierls stresses were calculated and are presented in Figure 2.11. The effects of size are limited to a small range for this elastic simulation, with the Peierls stress converging to 1 % when the simulation is ∼30 nm across, which is around a hundred Burgers vectors.

The variation of energy with respect to simulation size does not converge, as can be seen in Figure 2.11b. However this is expected: as derived by Nabarro [31] the energy of a single dislocation in an otherwise perfect cylindrical crystal will vary logarithmically with the radius of the crystal. A best fit line is shown in Figure 2.11b, with an equation of the form:

$$y = c_1 + c_2 \log(x) \tag{2.34}$$

which fits the results well. This is seen in the current work because the displacement field, Equation 2.15, includes a logarithmic term, whereas previous models have usually been limited to displacements parallel to the slip direction, at least in the far field.

The Peierls stress was calculated for a number of phases and compared with

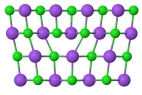

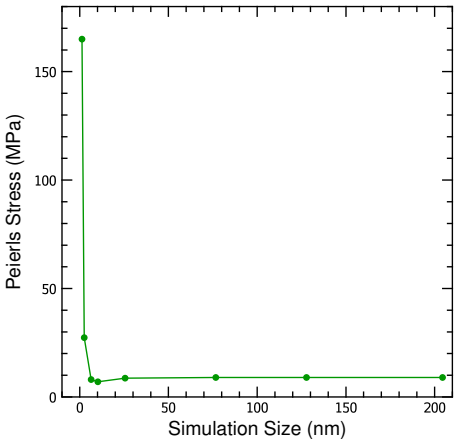

(a) The variation of the calculated Peierls stress with simulation size.

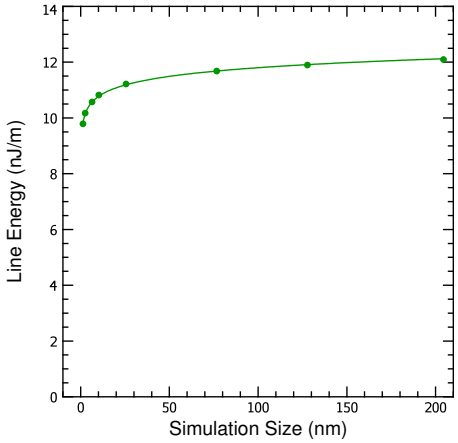

(b) The variation of the calculated dislocation line energy with the simulation size and a best fit line for a logarithmic function.

Figure 2.11: Plots characterising the sensitivity of the model to the simulation size. The value of the Peierls stress is quite quickly converged to a constant, the energy in fact increases logarithmically, as shown by the best fit line.

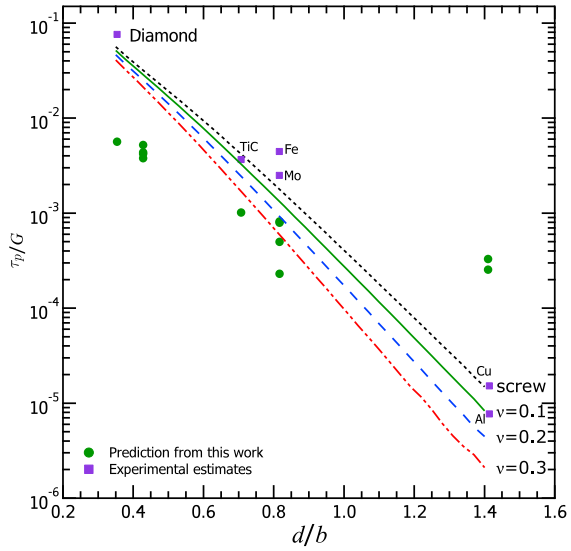

Figure 2.12: A comparison of predicted Peierls Stresses against experimental estimates [129] and a previous model [37] for an isotropic material, the highest for a screw dislocation and the others are for edge dislocations where $\nu = 0.1$, 0.2 and 0.3.

experiment and previous models, and is shown in Figure 2.12. As can be seen the qualitative trends are preserved, with the same trend in Peierls stress with lattice geometry observed. However the values predicted differ systematically from experiment: at low values of d/b the current model underestimates the Peierls stress and at high values of d/b the model overestimates the Peierls stress. This weaker influence of lattice geometry on the Peierls stress is consistent with previous Peierls models that have a periodicity of b rather than $b/2$ [35]. The model is therefore limited as a quantitative predictive tool, but should allow qualitative comparisons to be undertaken.

The effect of changes in the single crystal elastic tensor were assessed for the Fe_3C structure, cementite. Work by Miles Stopher and David Bombac on the effects of hydrogen embrittlement in steels have assessed the effects of hydrogen on the elastic tensor [127]. It is expected from experiment [127] that a softening of the cementite phase occurs, allowing dislocation mediated dissolution. The elastic tensors for the four compositions, 0 at%, 5 at%, 7 at%, 10 at% hydrogen, that were investigated are given in section A.1.

The Peierls analysis results are shown in Figure 2.13. There is little to no change in the Peierls stress at hydrogen loadings of below 7 %, but there is a clear and large drop in the Peierls stress for cementite between 7 % and 10 %. While, as seen earlier, the quantitative results of the model may not be directly comparable with experiment, the relative changes in behaviour are reliable. This is consistent with the idea that cementite is softened by the addition of hydrogen.

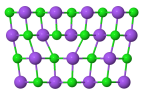

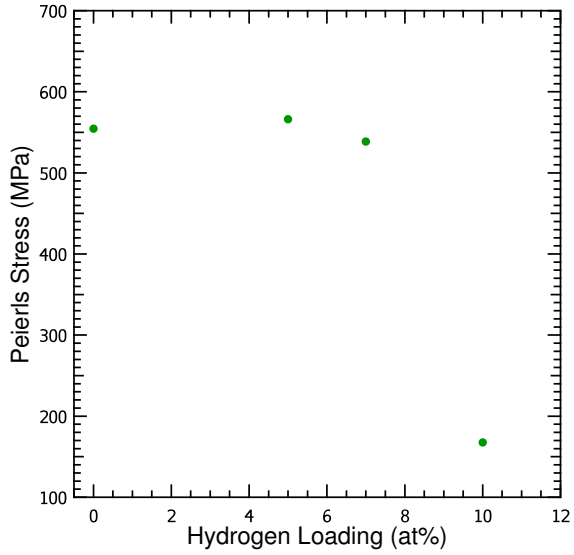

Figure 2.13: The effect of hydrogen loading on the predicted Peierls stress of cementite on the [1 0 0](0 1 0) slip system.

2.3.2 Dislocations in ionic solids

Energy changes in ionic solids were fitted with an empirical function in a similar manner to that described in section 2.3.1 except now the energy components are not misalignment and strain energy terms but electrostatic and short-range terms. This was done for the two slip systems known to operate in crystals with the rocksalt structure, the $<1\,1\,0>\{0\,0\,1\}$ and the $<1\,1\,0>\{1\,\bar{1}\,0\}$.

First the energy was calculated via a Python program, the code is available online [107], that used a simple approach: calculating the energy for all the interactions in the crystal with no cut offs. This gives the energy without the risk of artefacts that can be introduced by cut offs, but at the cost of computational time. Importantly the energy of the dislocation itself is difficult to estimate, since the energy calculated by this method includes the energy of the whole crystal, i.e. the energy of the free surfaces and so on. This was addressed by assuming that the energy changes were due to the dislocation alone, which is reasonable because the faces of the dislocated crystal are far enough from the dislocation not to deform very much.

The energy changes calculated in this way, using the same optimisation procedure as described above, are shown in Figure 2.14. There is a curious result that the periodicity appears to be different for the two dislocations, a period of b for the

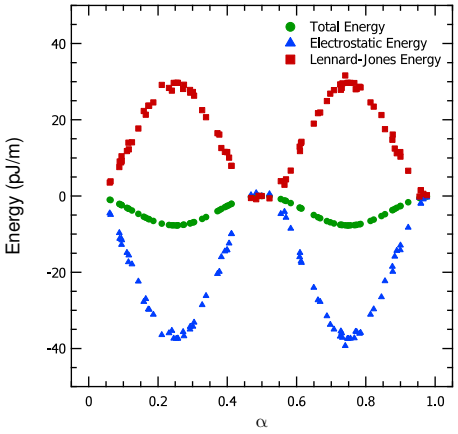

(a) The energy changes with displacement of a <1 1 0>{0 0 1} dislocation in NaCl.

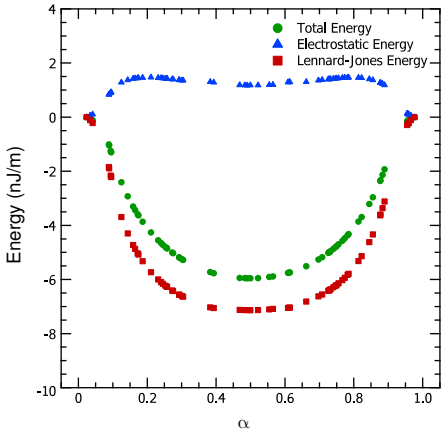

(b) The energy changes with displacement of a <1 1 0>{1 $\bar{1}$ 0} dislocation in NaCl.

Figure 2.14: The energy changes with position of dislocation in NaCl. Note that the scale of the energy changes is much larger for the <1 1 0>{1 $\bar{1}$ 0} slip system.

<1 1 0>{1 $\bar{1}$ 0} slip system and $^{b}/_{2}$ for the <1 1 0>{0 0 1} slip system. This can be explained in terms of the crystal structure.

Considering the core structures shown in Figure 1.11, for the <1 1 0>{0 0 1} slip system the $\alpha = 0.5$ position is nearly equivalent to the $\alpha = 0$ position. The two positions can be related by swapping all the cations for anions and vice versa. The result is that the electrostatic energy must be the same. Since the short range potential used here is symmetrical for anion-cation or cation-anion interactions, all the first neighbour interactions will also be the same since there are no cation-cation or anion-anion neighbours to swap. There will be differences in the second nearest neighbours, which change from anion-anion to cation-cation interactions and vice versa. This difference is observed; the halfway position is lower in energy than the initial position by $1.4 \times 10^{-22}\,\mathrm{J\,m^{-1}}$. This is a very small difference as expected, but is within the expected precision of the calculation. Thus strictly the period of the dislocation energy is b, but for practical purposes can be treated as $^{b}/_{2}$. Such a similarity does not exist for the <1 1 0>{1 $\bar{1}$ 0} slip system, so the period is more plainly b without extra minima.

The data was fitted using the function given in Equation 2.30, and this gave the Peierls stress of the two systems as 76.6 MPa for the <1 1 0>{0 0 1} slip system, and 63.7 GPa for the <1 1 0>{1 $\bar{1}$ 0} system. The value for <1 1 0>{0 0 1} system

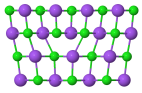

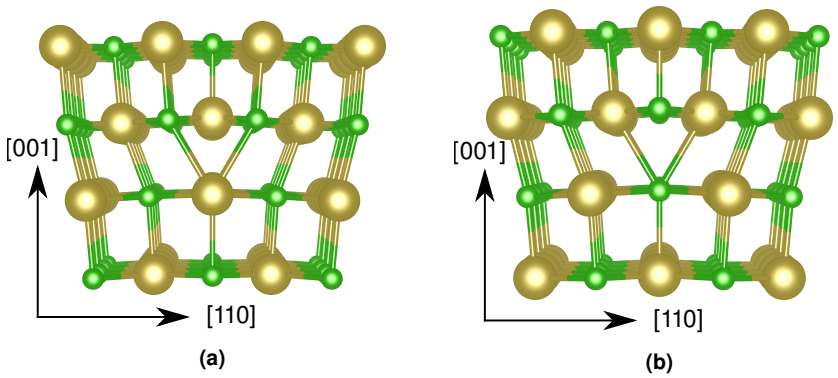

Figure 2.15: Dislocations in NaCl showing the similarity between the two symmetrical positions; if the short range potential were applied to only first neighbours these would be equivalent, related by reflection through the plane normal to the slip direction, in this case [1 1 0]. Graphics prepared with VESTA [74].

within a factor of 2 of experimental measurements of the Peierls stress, Haasen [97] estimated the Peierls stress of this slip system to be 140 MPa. The value for the $<1\,1\,0>\{1\,\bar{1}\,0\}$ slip system is clearly not in agreement with the estimated Peierls stress of 10 MPa.

The variation of the dislocation width is shown in Figure 2.16. The period of the variation of the width for the two slip systems is the same as that of the energy variation. The $<1\,1\,0>\{0\,0\,1\}$ slip system shows the expected behaviour, small and smooth variation, as shown in Figure 2.16a. There is some noise in the graph showing that perhaps the model has not fully converged on the lowest energy value. There is a much larger variation in the width for the $<1\,1\,0>\{1\,\bar{1}\,0\}$ slip system, Figure 2.16b, and there is a discontinuity in the value at around $\alpha = 0.1$. This corresponds to the very steep part of the energy variation shown in Figure 2.14b.

One problem with modelling dislocations in ionic materials is the computational complexity compared to the elastic case. The model must be three dimensional since the interactions are three dimensional, which means the number of atoms is larger. Additionally the calculation scales more quickly with the size of the simulation, since now there are n^2 energy calculations to do for n atoms rather than simply n for the elastic energy calculation. Thus despite using the NumPy [92], which is well optimised to efficiently undertake calculations, the scale of the simulation was much more limited, extending only tens of nanometers rather than hundreds from the dislocation core. Given the inherently long range nature of the electrostatic

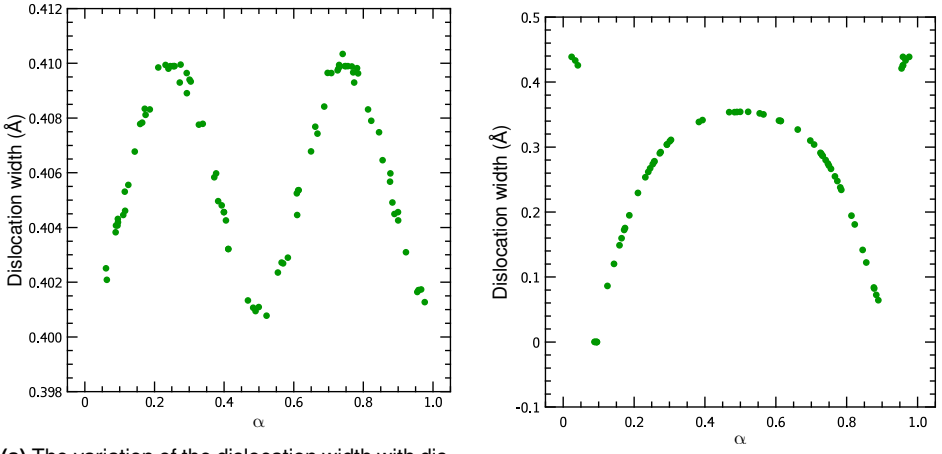

(a) The variation of the dislocation width with dislocation position for the <1 1 0>{0 0 1} slip system.

(b) The variation of the dislocation width with dislocation position for <1 1 0>{1 $\bar{1}$ 0} slip system.

Figure 2.16: The variation of the dislocation width with position for the two slip systems of NaCl. The <1 1 0>{0 0 1} slip system shows the expected behaviour, showing relatively small variation in a smooth and continuous manner. The <1 1 0>{1 $\bar{1}$ 0} slip system shows a much larger variation and a rapid if not discontinuous change at around $\alpha = 0.1$.

interaction this is potentially insufficient.

To address this, the model was adapted to use the LAMMPS [96] software package to undertake the energy calculation, using the Coulombic and Lennard-Jones calculators built in to the LAMMPS package. An example script and input files are included in section A.3. The principle is much the same, though now the energy calculation is using the highly optimised LAMMPS routines. These rely on choosing appropriate parameters and settings, which was done according to the LAMMPS manual [96]. One particular advantage is the ability to employ periodic boundary conditions along the length of the dislocation line, thus removing potential artefacts that might arise from the termination of the dislocation.

The results for the $<1\,1\,0>\{1\,\bar{1}\,0\}$ slip system are shown in Figure 2.17. The variation is quite similar to that found using the naïve Python based energy calculator despite the periodic boundary conditions along the dislocation line and extending the simulation out from the core to $\sim$100 nm. The maximum gradient of the best fit achievable using Equation 2.30 gives the Peierls stress as 63.8 GPa, which is very close to the the result obtained earlier, with an original calculator written in Python, as shown in Figure 2.14b.

The variation of the dislocation width with α is shown in Figure 2.18. There are some differences between the Python based model and the LAMMPS based model.

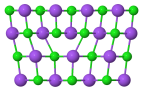

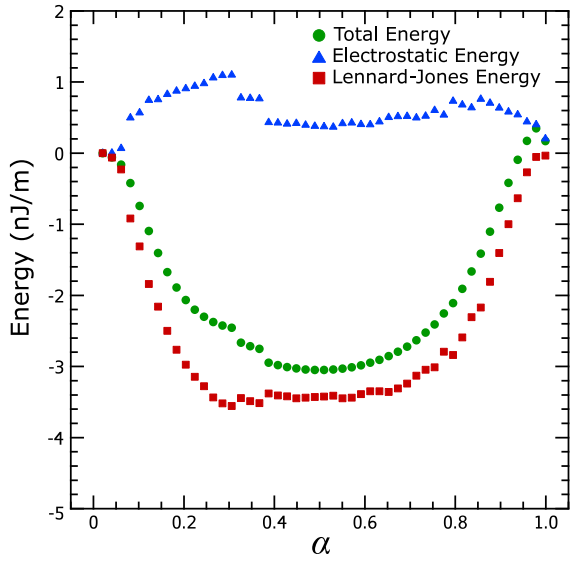

Figure 2.17: The energy variation of a <1 1 0>{1 $\bar{1}$ 0} dislocation in NaCl using the energy calculations available in LAMMPS. There is a lot of scatter, which does not appear to be random, but is likely due to insufficiently tight convergence criteria.

Both models show a discontinuity in the width, dropping rapidly around $\alpha = 0.1$, but the LAMMPS based model predicts zero width for α ~0.1 to 0.9, where the Python based model predicted an increase to a maximum at $\alpha = 0.5$. This might be attributable to the size of the simulation or the termination of the dislocation since those are the principle differences between the two models.

It therefore seems unlikely that simulation size or the termination of the dislocation at the free surface were major problems, instead some other factor is likely at fault.

This model of a dislocation in ionic material makes a number of assumptions that it may not be valid. In the definition of the displacement field the model has assumed that all the atoms follow the same displacements that as would occur in a continuous isotropically elastic medium. This might be invalid in more than one way: firstly, there is no possibility of local deviation from the displacement field, which particularly likely to occur in the core region; secondly there is the possibility that given the long range interactions across regions of the crystals are quite unlike the elastic energy calculations used to derive the displacement field the entire form of the field may be invalid for this application.

The second here seems unlikely given that the harder slip system was well de-

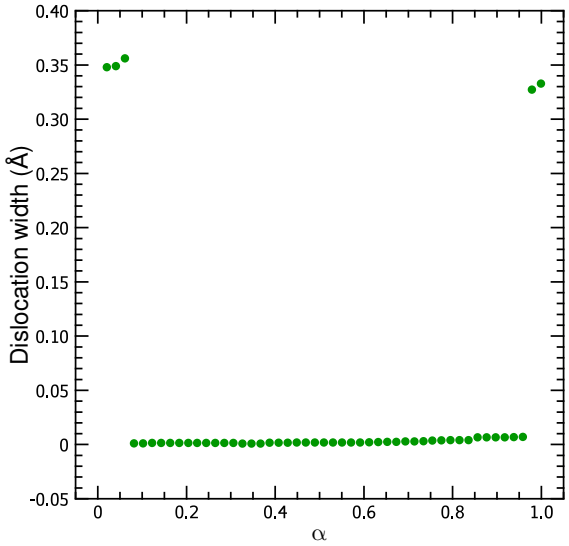

Figure 2.18: The variation of the dislocation width with position for the <1 1 0>{1 $\bar{1}$ 0} slip system in NaCl when using the energy as calculated by the LAMMPS software package.

scribed by the model, but the possibility of core reconstruction has been examined before, such as Hoagland *et al.* [102] who observed a deviation from the ideal Volterra dislocation displacements. This could be addressed by the incorporation of more flexible boundary conditions such as those used by Hoagland *et al.*

Another set of simplifications have been made in the interaction potential used here. The Lennard-Jones potential is one of the simplest potentials that can predict any material behaviour, but more accurate, if more computationally expensive, potentials do exist, incorporating the polarisability of atoms and more accurately representing the Pauli exclusion energy.

Finally there is a possible source of error in the experimental evidence for the low Peierls stress on this softer slip system. All experiments necessarily occur at finite temperatures, while the Peierls stress is by definition only valid at 0 K. It has been observed that dislocations in alkali halides can deviate from the usual increase in critical resolved shear stress for dislocation motion as the temperature approaches absolute zero.

There are two effects noted by Haasen [97] that could cause the experimental estimate of the Peierls stress to be an under estimate. One effect is that the first 1 % of impurity atoms can cause softening at low temperatures (<30 K) can make

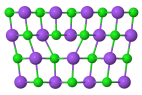

the nucleation of kinks easier and so lower the stress required to move a dislocation. The other effect that has been suggested to explain anomalies at low temperatures is that dislocations might tunnel through the Peierls barrier in NaCL and LiF at very low temperatures (<5 K).

2.4 Conclusions

A parametrised form of the displacement field around an edge dislocation has been reached by adapting the solution for an isotropic elastic medium. This allows the construction of atomic configurations in three dimensions rather than one. This formulation also reduces the parameter space that must be searched for the optimal dislocation structure to a tractable size.

A series of Python modules have been written to allow the modelling of dislocations in a variety of materials using a variational approach to minimise the energy of the atomic configuration for every dislocation position. The Peierls stress is calculated from the maximum gradient of the dislocation energy. The modular nature allows functionality to be added or altered easily.

The first module builds the dislocation by constructing an array representation of atomic coordinates around the dislocation core via the adapted displacement field. This is deliberately left extensible to allow, for example, the addition of a screw dislocation or core reconstruction.

Two further modules have been written to calculate the energy of a dislocation as represented by an array of atomic coordinates. One builds on the existing Peierls models that use linear elasticity for strain energies away from the slip plane and a misalignment potential for the slip plane, either approximated as a sinusoid that obeys Hooke's law at low strains, or fitted empirically to *ab initio* calculations of the γ-surface. This module extends the Peierls analysis to use the full stiffness tensor rather than simple elastic constants. The other uses the electrostatic interaction and the Lennard-Jones potential to calculate the energy of a dislocation in an ionic solid.

The elastic Peierls model is in agreement with the trends in material behaviour observed in experiment and predicted by previous models. However the effect of lattice geometry is not as strong in this model as is observed by experiment, consistent with previous models that have a periodicity of a full, rather than a half, Burgers vector, thus only qualitative conclusions can be drawn. The model does predict a softening of the cementite structure when hydrogen is added, as predicted by experiment.

The ionic Peierls model successfully predicts the behaviour of the $<1\,1\,0>\{0\,0\,1\}$ slip system in NaCl as observed by experiment. The electrostatic and short-range repulsion energy components vary out of phase with each other, in a parallel to the strain energy and misalignment energy in traditional Peierls models. The behaviour of the $<1\,1\,0>\{1\,\bar{1}\,0\}$ slip system is not successfully predicted. It was shown that this was not due to the size of the simulation or the termination of the dislocation line at a free surface by the use of LAMMPS as an energy calculator, which allowed much larger simulations and the use of periodic boundary conditions.

There are a number of assumptions inherent to the model, either implicitly or explicitly. The application of the adapted Volterra displacement field is a central assumption in this model, and this could be investigated by allowing the coordinates of atoms within some core region to relax freely while applying the displacement field to the outer regions. This is challenging due to the increased complexity of the optimisation of the dislocation structure as more parameters are allowed to vary independently. Another simplification is the use of the Lennard-Jones potential, which ignores polarisability, which is only an issue in the softer $<1\,1\,0>\{1\,\bar{1}\,0\}$ slip system. More realistic potentials are available either to be implemented directly, or within projects such as LAMMPS. A final possibility that is not investigated here is the role of point defects in dislocation motion in the alkali halides. These are known to be important but the model assumes that the crystals are perfect aside from the single edge dislocation. This could be addressed with molecular dynamics, but would require significantly more computing power.

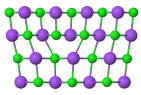

Chapter 3

Heterogeneity in the MAX phases

As discussed in section 1.2, the MAX phases are predicted to be brittle by a wide range of ductility criteria but they are in fact observed to be damage tolerant and to flow easily in the basal plane [63]. Predictions of the Peierls stress made using the methods described in section 1.1 have been made previously [68, 82]. However these have had limited success, producing over-estimates, for example Gouriet *et al.* [68] reported the Peierls stress to be at least 611 MPa which is similar to that estimated for titanium carbide and other very hard brittle materials in which slip is limited at room temperature by the Peierls mechanism [37, 130–132]. Given that flow stresses in the region of a few tens of MPa have been observed at room temperature [63, 64], which is more comparable with FCC metals than FCC carbides, it is reasonable to expect the Peierls stress of MAX phases to be lower than that of TiC.

The poor performance of Peierls models for MAX phases, and potentially for other complex phases, might be due to the treatment of the MAX phase unit cell as elastically homogeneous. This is surprising because many studies have discussed the heterogeneity of the bonding and electron structure. One recent review was written by Magnuson and Mattesini [133], and discusses the complex and mixed nature of the bonding varying across the different atomic sites: more metallic in the MA layers, more covalent in the MX layers, and charge transfer contributing an ionic component to the bonding.

The bonding is associated with many of the properties of the MAX phases, for

example high melting point, high specific stiffness, electrical and thermal conductivity, and a near zero Seebeck coefficient to name a few [76, 133, 134]. However the clear and strong heterogeneity of the unit cell has largely been neglected when considering the mechanical properties of the MAX phases, the only consideration of the atomic environments being the choice of plane at which the generalised stacking fault energy was calculated [82].

There has been some study made of the variation in properties across the unit cell of the MAX phases, for example in calculating the generalised stacking fault energies at different positions within the unit cell such as the work by Gouriet *et al.* [68], or surface energies such as the work by Music *et al.* [135]. Gouriet *et al.* [68] showed that the gamma surface is lower for a stacking fault between the M and A sites than for a fault between the M and X sites, which will also correlate with lower stiffnesses for elastic deformation in the M-A regions than the M-X regions. It would be surprising if no account had ever been made for the heterogeneous nature of the MAX phases. What has not been studied, however, is the relative variation of these properties, in particular by considering the changing elastic responses of the two regions separately. Given that any macroscopic experiments can only probe the whole unit cell and not the individual regions within it, the local variations of these regions may be key to understanding the flow behaviour of the MAX phases.

3.1 Chemical heterogeneity

If the MAX phases are elastically heterogeneous, there is the question of what might be the expected properties and how these might vary within the MAX phase unit cell. A simple way of characterising the chemical heterogeneity is the electronegativity, χ, of regions within the unit cell. For both the M–X and M–A regions, an average electronegativity is easily calculated, as once sharing of atoms between the regions is accounted for, there are equal numbers of M and A atoms in the M–A region and similarly equal numbers of M and X atoms in the M–X region. The difference in

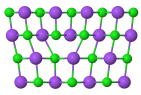

electronegativity between the two regions is therefore defined by:

$$\Delta\chi = \frac{\chi_X - \chi_A}{2} \tag{3.1}$$

where χ_X and χ_A are the electronegativities of the X and A atoms respectively. The electronegativity of the M atoms does not feature since the M atoms contribute to both regions.

There are a variety of measures of electronegativity, but perhaps the most fundamental and transferable is the Mulliken scale [136], which takes the electronegativity of a species to be the average of the ionisation energy, the energy change upon removing an electron, and the electron affinity, the energy change upon adding an electron. This scale is more fundamental than others because it is calculated from the fundamental properties of atoms, as opposed to more relative scales that are calculated from enthalpies of formation and covalent radii and so on [137].

Since the elements that take the X site, carbon and nitrogen, are generally more electronegative than those that take the A site, elements like aluminium and silicon, it is expected that electron transfer will be into the M–X region from the M–A [76]. Such a transfer would be expected to increase the strength of the bonding in the M–X layer and reduce it in the M–A, with a corresponding change in the moduli of the two regions.

3.2 Density functional theory calculations

Measuring single crystal elastic constants for the MAX phases is challenging due to the difficulty of growing single crystals and experimentally determining the stiffness of sub-unit cell regions of the crystal presents an even greater challenge. Instead density functional theory (DFT) can be employed. DFT has been widely used to calculate single crystal elastic constants of a large variety of materials and is considered reliable and reproducible [138].

The density functional theory calculations were performed with the SIESTA

package [139], a pseudopotential-based LCAO package using semicore pseudopotentials with partial core corrections in the Perdew-Burke-Ernzhof (PBE) formulation generated and tested by the ATOM implementation [139] of the Troullier-Martins procedure [140, 141] as described in the software documentation [142]. A double-ζ polarised basis set including the semicore states was used, the cutoff radii of which were optimised with a variational simplex method.

The starting point for the calculations presented here was a series of optimised unit cells for a range of MAX phases produced by a procedure developed by Philip Howie. A optimisation approach to generating suitable pseudopotentials was taken using ATOM [142]; pseudopotentials with a range of cut-off radii were tested against all-electron calculations of the atomic ground state and a number of excited states and the cut-off radius is improved until the best (i.e. closest to all-electron) pseudopotential is identified.

Initially some simulation parameters have to be optimised: the k-grid size and the mesh cut-off. Suitable values are chosen to provide sufficient accuracy and ensure the energy converges [143].

Once pseudopotentials and the simulation parameters have been generated the lattice parameters are optimised. The literature values are used as the starting point but the calculated equilibrium lattice parameter is typically 1 % to 2 % bigger that the experimental value when using the generalised gradient approximation [144–146]. Initially the lattice parameter ratio, c/a, is kept fixed and the lattice parameter a is varied to reduce the hydrostatic pressure to zero.

The basis set was optimised with this roughly equilibrated unit cell. Most of the variables are taken to be suggested values from examples provided by the authors of SIESTA [143]. The problem is variational (i.e. a lower energy means a better basis set) so the basis set is optimised by the simplex optimisation method, also known as the Nelder-Mead method [125]. With an accurate basis set the lattice parameters are now optimised to find the true equilibrium point, relaxing both a and c to reduce the stresses to zero (or equivalently finding the minimum energy).

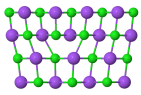

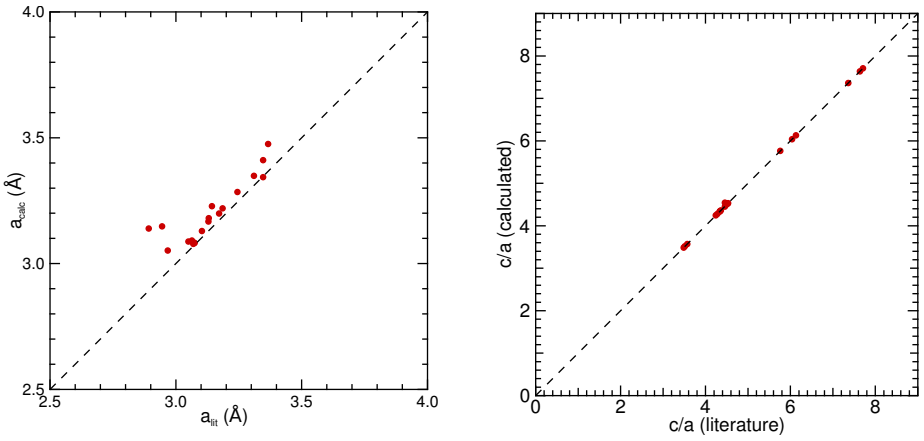

(a) A comparison between the lattice parameter, a, calculated here with literature values.

(b) A comparison between the calculated lattice parameter ratio, c/a, with literature values.

Figure 3.1: A comparison of the unit cells calculated by DFT with those reported in the literature. There is reasonable agreement between the lattice parameters a calculated here and found experimentally in the literature. The lattice geometry, c/a, is in excellent agreement with reported values.

Many of the atomic positions are fixed by symmetry, but those parameters that are free to vary without breaking the structure's symmetry are relaxed. These are the heights in the c-axis of some of the atoms as shown in Figure 1.9.

A comparison of the lattice parameters generated by DFT with Howie's method is shown in Figure 3.1 and the data are summarised in Table 3.1. The agreement is good as expected, particularly in the lattice geometry, c/a. The better agreement in c/a than in the lattice parameters themselves is because the errors in the lattice parameters are correlated, in that both a and c are overestimated as expected with the PBE formulation [144, 146]. These equilibrated unit cells were used as the basis for further investigation of MAX phase behaviour.

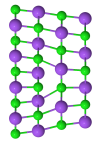

Phase	a	a_{lit}	c/a	c/a_{lit}	z_1	$z_{1,\mathrm{lit}}$	z_2	$z_{2,\mathrm{lit}}$	z_3	$z_{3,\mathrm{lit}}$	d/b	$z_{\mathrm{M-A}}$	$d_{\mathrm{M-A}}$
Nb_2AlC	3.1297	3.1035	4.5215	4.5213	0.0898	0.0880	-	-	-	-	0.7243	0.1602	2.2479
Nb_2GaC	3.1806	3.1310	4.3322	4.3325	0.0887	0.0880	-	-	-	-	0.6988	0.1613	2.1880
Nb_2InC	3.1987	3.1720	4.5303	4.5303	0.0827	0.0860	-	-	-	-	0.7579	0.1673	2.4041
Nb_2SC	3.3484	3.3100	3.4862	3.4864	0.0944	0.0990	-	-	-	-	0.5425	0.1556	1.7956
Nb_2SnC	3.2844	3.2450	4.2441	4.2435	0.0833	0.0850	-	-	-	-	0.7074	0.1667	2.2954
Ti_2AlC	3.0517	2.9680	4.5422	4.4554	0.0844	0.0882	-	-	-	-	0.7378	0.1656	2.1898
Ti_2GaC	3.0914	3.0640	4.3431	4.3424	0.0855	0.0880	-	-	-	-	0.7143	0.1645	2.1887
Ti_2InC	3.1481	2.9450	4.4905	4.4852	0.0790	0.0829	-	-	-	-	0.7670	0.1710	2.2587
Ti_2SC	3.2279	3.1432	3.5172	3.5158	0.0977	0.0998	-	-	-	-	0.5355	0.1523	1.6830
Ti_2SnC	3.2196	3.1860	4.2786	4.2781	0.0807	0.0790	-	-	-	-	0.7243	0.1693	2.3076
Zr_2InC	3.3434	3.3470	4.4541	4.4547	0.0874	0.0860	-	-	-	-	0.7243	0.1626	2.4243
Zr_2SC	3.4755	3.3663	3.5711	3.5714	0.0998	0.1013	-	-	-	-	0.5364	0.1502	1.8058
Zr_2SnC	3.4110	3.3470	4.3590	4.3591	0.0854	0.0860	-	-	-	-	0.7175	0.1646	2.4015
Ti_3AlC_2	3.0831	3.0730	6.0390	6.0387	0.0710	0.0691	0.1305	0.1276	-	-	0.7216	0.1224	2.2714
Ti_3SiC_2	3.0820	3.0747	5.7642	5.7620	0.0727	0.0722	0.1355	0.1353	-	-	0.6600	0.1147	2.0321
Nb_4AlC_3	3.1674	3.1296	7.7081	7.7073	0.0549	0.0552	0.1088	0.1086	0.1575	0.1574	0.7130	0.0926	2.2345
Ti_4GaC_3	3.0781	3.0690	7.6371	7.6377	0.0516	0.0558	0.1091	0.1068	0.1549	0.1564	0.7263	0.0936	2.1940
Ti_4SiC_3	3.0878	3.0500	7.3627	7.3614	0.0535	0.0532	0.1120	0.1118	0.1603	0.1599	0.6604	0.0901	2.0230

Table 3.1: The unit cell parameters as modelled by density functional theory and some values from the literature for comparison.

3.3 Calculating the local stiffness

One method for calculating the elastic constants via DFT is simply to simulate the unit cell with periodic boundary conditions and apply a stress/strain state and fit either the equation:

$$\sigma_{ij} = C_{ijkl}\varepsilon_{kl} \tag{3.2}$$

or:

$$u = \frac{1}{2}C_{ijkl}\varepsilon_{ij}\varepsilon_{kl} \tag{3.3}$$

where σ_{ij} is the stress tensor, ε_{ij} is the strain tensor, u is the strain energy per unit volume and C_{ijkl} is the stiffness tensor. This was applied by Aryal *et al.* [46] to a very wide range of MAX phases. Care must be taken to reproduce the physically realistic situation where the stress is equal throughout the unit cell but the strain can vary, i.e. the strain must be applied macroscopically to whole the simulation cell but the atomic positions must then be allowed to relax into the lowest energy configuration.

The latter equation was used to find the local stiffness within a region of the unit cell. The single crystal elastic constants must be dropped since a tensor formulation of heterogeneous elasticity is not the aim, instead local shear moduli are calculated. The unit cell is divided naturally into two distinct regions that are obvious from the geometry of the crystal structure, the local chemistry and nature of bonding: there is a more metallic layer, the M–A layer; and a more covalent layer, the M–X layer, see Figure 1.9. The layer of M-atoms that are bonded to both A-atoms and X-atoms is the natural boundary.

To localise the strain in, say, the M–A layer, all the bonding, that is the relative atomic positions, in the M–X layer are held rigid and are displaced as a whole such that in each M–A layer the appropriate strain is applied. The relative positions of the atoms within the M–A layer are then allowed to relax to achieve the minimum

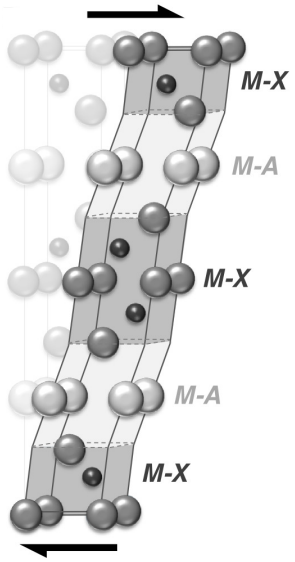

Figure 3.2: Schematic of non-uniform elastic deformation in a "211" MAX phase showing the regions that might be considered distinct, the M–A and M–X layers.

energy. The equation that must then be fitted is:

$$u = \frac{1}{2} G_i \gamma^2 \tag{3.4}$$

where γ is the applied strain and G_i is the local shear modulus, namely either $G_{\mathrm{M–A}}$ or $G_{\mathrm{M–X}}$. The procedure is applied vice versa to calculate the M–X properties.

The overall shear modulus for the whole crystal structure is calculated in the same manner with no restrictions on the atomic positions: all the atoms are allowed to relax fully. Since this relaxed shear is equivalent to a uniform applied stress, an analogy is possible with calculation of the transverse stiffness of long fibre composite materials, the so called slab model [147]. The slab model is illustrated in Figure 3.2. The results of the local calculations can be compared with the overall case using the equation:

$$G_{\mathrm{slab}} = \left[\frac{f_{\mathrm{M–X}}}{G_{\mathrm{M–X}}} + \frac{f_{\mathrm{M–A}}}{G_{\mathrm{M–A}}} \right]^{-1} \tag{3.5}$$

where G_{slab} is the estimate for the overall shear modulus, f_i is the volume fraction of the region i and G_i is the shear modulus of region i. The volume fractions are estimated from the crystal structures of the MAX phases. In particular the fractional coordinate in the c direction of the M1 site in the 211 phases, z_1, and the position

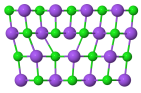

of the M2 site in the 312 and 413 phases, z_2, as shown in Figure 1.9, determines the volume fraction of the regions of the unit cell:

$$f_{\text{M–A}} = \begin{cases} 1 - 4z_1 & \text{for 211 phases} \\ 4z_2 & \text{for 312 and 413 phases} \end{cases} \tag{3.6a}$$

$$f_{\text{M–X}} = \begin{cases} 4z_1 & \text{for 211 phases} \\ 1 - 4z_2 & \text{for 312 and 413 phases} \end{cases} \tag{3.6b}$$

3.4 Results and Discussion

The moduli of the separate layers are presented in Figure 3.3a and summarised in Table 3.2. The M–X layer is stiffer than the M–A layer for all the MAX phases studied here, as expected from the nature of the bonding in the MAX phases as discussed in section 1.4. There is an overall increase in the stiffness of the M–X layer and an overall decrease in the stiffness of the M–A layer as the electronegativity difference between these layers increases, although the data are scattered around that correlation, presumably as more complex chemical factors operate in addition to electronegativity differences.

The trend is clearer when the ratio of the moduli is considered, as shown in Figure 3.3b. The ratio $G_{\text{M–A}}/G_{\text{M–X}}$ varies with the electronegativity difference between the layers, so even where other chemical effects cause the overall bonding to be stronger, the *relative* moduli of the two layers are altered by electrons being drawn from the M–A layer into the M–X layer to varying extents. In the case of A atoms like indium or gallium, electrons are easily lost from the M–A layer to the M–X layer, reducing the ratio, while in the case of sulphur occupying the A site there is almost no electronegativity difference between the layers and the ratio is higher.

This change is reflected in the bond lengths in the M–A layers, the bonds getting longer as electronegativity increases. This reflects a weakening of the bonds in the

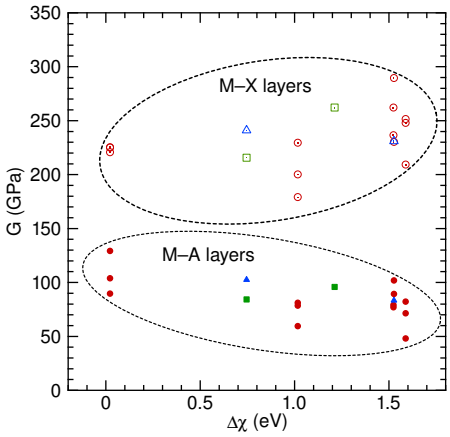

(a) The variation of shear moduli of the M–A and the M–X layers.

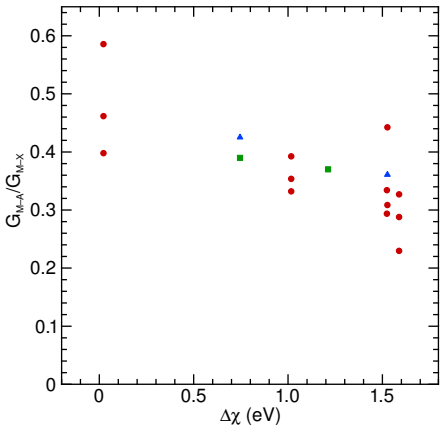

(b) The variation of the ratio of the shear moduli of the M–A and the M–X layers.

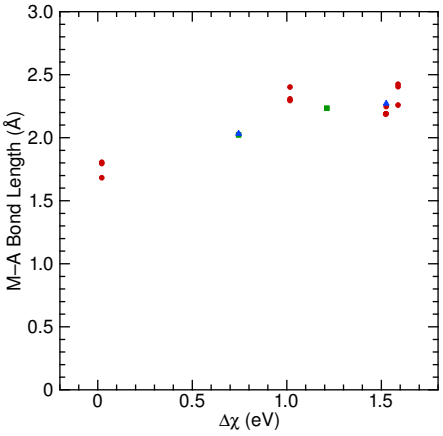

(c) The variation of the M–A bond length.

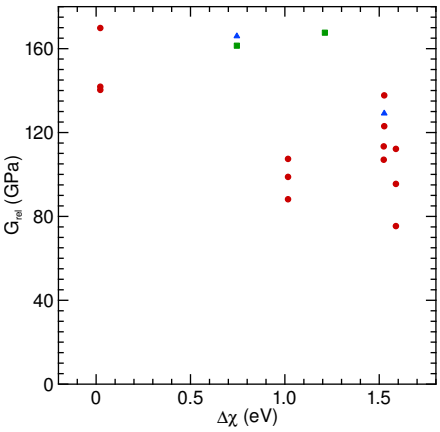

(d) The variation of the overall shear modulus, G_{rel}.

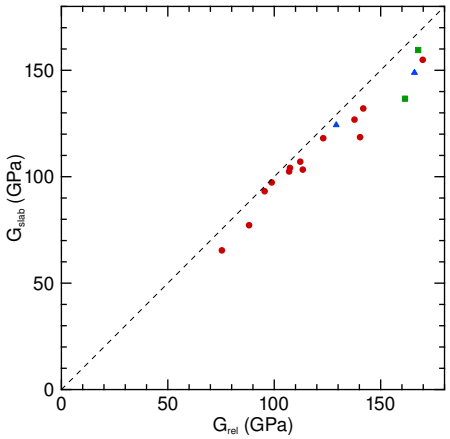

(e) A comparison of the overall shear modulus of the MAX phases, G_{rel}, and the shear modulus calculated from the local shear moduli using the slab model, G_{slab}. The dotted line is $y = x$.

Figure 3.3: The results of modelling by DFT the elastic properties of the MAX phases. $\Delta\chi$ is the electronegativity difference between the M–A and M–X layers. Circles, squares and triangles represent 211, 312, and 413 phases respectively.

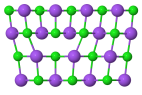

Phase	G_{rel} (GPa)	$G_{\mathrm{M–A}}$ (GPa)	$G_{\mathrm{M–X}}$ (GPa)	G_{slab} (GPa)	$G_{\mathrm{M–A}}/G_{\mathrm{M–X}}$	$\Delta\chi$ (eV)
Nb_2AlC	137.7	101.9	230.4	127.4	0.442	1.5260
Nb_2GaC	113.4	79.1	236.6	103.6	0.334	1.5233
Nb_2In	112.2	82.3	251.6	105.9	0.327	1.5880
Nb_2SC	141.8	103.9	225.1	130.4	0.462	0.0214
Nb_2SnC	107.4	81.2	229.5	103.5	0.354	1.0166
Ti_2AlC	123.0	89.3	289.5	116.5	0.308	1.5260
Ti_2GaC	107.0	77.0	262.2	101.5	0.294	1.5233
Ti_2InC	95.5	71.4	248.0	92.1	0.288	1.5880
Ti_2SC	169.8	129.3	220.8	154.3	0.586	0.0214
Ti_2SnC	98.8	78.6	200.2	97.8	0.393	1.0166
Zr_2InC	75.4	48.1	209.3	65.8	0.230	1.5880
Zr_2SC	140.3	89.7	225.4	118.1	0.398	0.0214
Zr_2SnC	88.2	59.5	179.1	77.1	0.332	1.0166
Ti_3AlC_2	129.1	83.3	230.9	101.8	0.361	1.5260
Ti_3SiC_2	165.9	102.5	241.0	144.5	0.425	0.7453
Nb_4AlC_3	167.6	95.8	262.2	159.5	0.365	1.2117
Ti_4SiC_3	161.4	84.3	215.6	138.1	0.391	0.7453

Table 3.2: Summary of the elastic properties calculated by density functional theory calculations.

M–A layer as electrons are removed to the M–X layer.

The overall modulus is calculated by imposing an overall strain on the unit cell and allowing the atomic positions to relax, hence this is termed the relaxed modulus, G_{rel}. There is a decrease in the shear modulus of the MAX phases as the electronegativity difference across the structure increases, the contribution of the weakening M–A bond lowering the overall shear modulus more than the strengthening of the M–X bonding raises it.

The slab model was used to compare the local moduli, $G_{\mathrm{M–A}}$ and $G_{\mathrm{M–X}}$, with the overall modulus, G_{rel}, using Equation 3.5. The results are plotted in Figure 3.3e. The correlation is very good, showing that the local properties, considered at the sub-unit cell level, are in agreement with the macroscopic properties.

3.5 Conclusions

The MAX phases have been modelled with density functional theory calculations. The unit cells were optimised and found to be in good agreement with the literature.

These unit cells formed the basis of further investigation.

The shear modulus of the M–A and M–X regions of the structure were investigated, as was that of the entire MAX phase structure. The shear modulus was calculated by examining the energy changes for a range of applied shear strains up to 2 % and fitting to Hooke's law.

While investigation of the properties across the unit cell, for example by calculating the generalised stacking fault energy for planes intersecting different parts of the unit cell; the idea of separating the elastic response across regions of the unit cell in such an explicit way has not been undertaken before. The method of calculating local shear by applying shear strains to one layer of a unit cell, but fixing relative atomic positions in all other parts of the unit cell has been verified. The local shear moduli can be combined with a slab model by assuming an equal stress everywhere. The overall shear modulus calculated in this fashion agrees well with calculations of the overall shear modulus and is consistent with experimental observations.

The shear moduli of both the M–A layer and the M–X layer varied with the electronegativity difference between them, as the difference increased (M–X becoming more electronegative) the M–A layer became more compliant and the M–X layer became stiffer. In particular the ratio of these moduli was well correlated with the electronegativity difference between the M–X and M–A layers.

This has shed light on the way that crystal chemistry controls the elastic responses of the MAX phases, and why the overall elastic response, as characterised by stiffness, does not follow the usual trends that might be expected. As the chemical bonding is strengthened in one region, usually the M-X region, there is a corresponding weakening in the M-A region. These effects are evident in the ratio of the local moduli, but are far less obvious in the absolute stiffnesses observed.

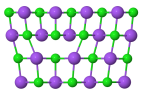

Chapter 4

Dislocations in MAX phases

In Chapter 3 elastic heterogeneity of the unit cell was discussed and the local elastic properties were shown to have a strong dependence on the chemical environment. As discussed in Chapter 1, the Peierls stress (i.e. the lattice resistance at 0 K) is very sensitive to the elastic properties of a crystal. Thus the elastic heterogeneity is expected to have a strong effect on the dislocations in the MAX phases.

The elastic properties of the different layers of the MAX phases are not in the form of full elastic tensors so the approach taken in Chapter 2 to use the full strain state cannot be applied. Instead a simplified model, adapted from that presented by Clegg *et al.* [37] is used that relies on only simple strains and elastic constants. This model was shown to be in good agreement with experiment across orders of magnitude of the Peierls stress for a wide range of materials and is used here to demonstrate the effects of elastic heterogeneity on the Peierls stress.

4.1 Adapted Peierls model

The lack of a full elastic tensor means that the Peierls model used in this case was adapted from the one published by [37]. This works in a similar way to the model described in Chapter 2 except only the first layer of atoms either side of the slip plane are considered and the only displacements allowed are parallel to the Burgers vector, in analogy with the original Peierls model.

The calculation is essentially the same; the dislocation configuration is till found by minimising the dislocation energy, and the dislocation energy is still a balance between two contributions: the elastic energy in the bonds outside the slip plane and the misalignment energy of those bonds across the slip plane. The Peierls stress is then the maximum gradient of the energy changes as the dislocation is displaced. However some aspects are different.

The original model was written to calculate the misalignment energy using the Frenkel approximation, as given in Equation 1.1, but the adapted model was extended to use a parametrised γ-surface to represent the misalignment energies, as represented by the summation

$$\gamma = \sum_{m=1}^{M} C_m \left[1 - \cos\left(\frac{2m\pi\phi}{b}\right)\right] \tag{4.1}$$

where γ is the energy in $\mathrm{J\,m^{-2}}$, C_m are a series of parameters fitted by a least-squares method to a set of energies at different misalignments, m is an integer between 1 and some maximum M which is chosen to be the lowest number that adequately captures the energy profile of the γ-surface, b is the Burgers vector and ϕ is the misalignment in units of Å, such that ϕ/b defines a sort of fractional misalignment. It was generally found that $M = 3$ was sufficient to capture the shape of the γ-surface, but was sometimes extended to six.

The other major difference is that the model in [37] optimises the structure of the dislocation only at the equilibrium position, not at every sampled displacement. The adapted model optimises the structure of the dislocation for every position by searching for the dislocation width that yields the lowest dislocation energy.

The elastic moduli and unit cell geometries, both required for the Peierls model, of the regions of the MAX phase structures were calculated in Chapter 3 so the only other required input for the model is the misalignment potential, derived from the γ-surface.

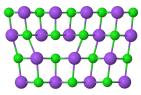

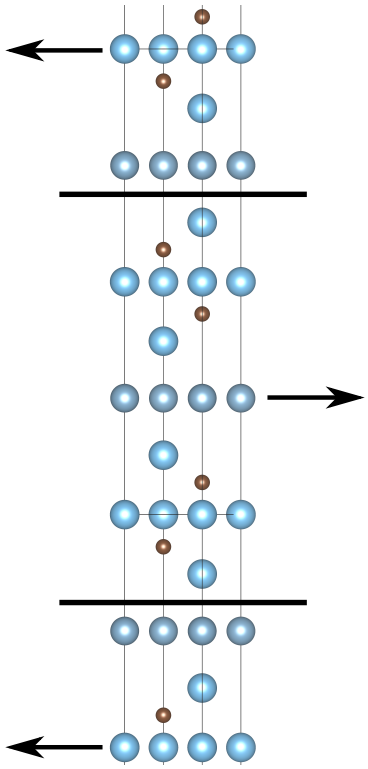

Figure 4.1: Schematic showing the displacements applied to a slab of crystal within a periodic cell to create two opposing stacking faults. The energy changes of the system are therefore twice the γ-surface. Graphic prepared with VESTA [74].

4.2 Calculating the γ-surface

The density functional theory calculations used the same initial set-up as discussed in section 3.2, based on the equilibrated unit cells with periodic boundary conditions in all directions. To calculate the gamma surfaces, a displacement across a plane must be imposed. The simplest way to do this is to maintain the periodic boundary conditions and introduce two opposing stacking faults, as shown schematically in Figure 4.1. There will be a dependence of the stacking fault energy on the distance between stacking faults, so the simulation must be converged with respect to this distance. In practice the lattice parameter of the MAX phases is long enough that only one or two unit cell repeats were necessary.

To displace the atoms, SIESTA's Z-matrix was used [143]. This allows the coordinates of the atoms to be constrained separately in each direction; the displacement parallel to the slip direction, $a/3<1\,1\,\bar{2}\,0>$ was imposed and the atomic positions

were relaxed perpendicular to this displacement. This is important as unreasonably close atomic positions would occur without this relaxation. In analogy with the FCC metals it might be expected for there to be a stable stacking fault. The M–A layer can be seen as a single repeat of the HCP structure, with ABA stacking; the faulted stacking, relative to the other M–A layer in the unit cell, is then ACA, see Figure 1.9.

In materials like aluminium dislocations are know to separate into partial dislocation pairs because the stacking fault energy is low enough that dissociating one full dislocation to become two partials reduces the overall energy despite the introduction of a stacking fault [148]. Atoms are therefore displaced along two successive $<2\,1\,1>$ type directions that sum to $<1\,0\,1>$ overall. Even in the case of full dislocations in close-packed structures this kind of lateral displacement is likely in the core.

Since the hexagonal structure of the MAX phases would have analogous stacking faults, we can expect a metastable point in the middle of the γ-surface, corresponding to the stable stacking fault energy, with a substantial lateral displacement of atoms. The Peierls model, either the one developed in Chapter 2 or its predecessors [37, 149], cannot account for this so it must be accounted for during the calculation of the γ-surface.

Initially 40 positions were modelled at regular intervals between one perfect position and the next displacing along the $<1\,1\,\bar{2}\,0>$. The energy changes, relative to the equilibrium position, were fitted to the function given in Equation 4.1 using the "`scipy.curve_fit`" package provided by the SciPy project [121].

4.3 Results and discussion

4.3.1 The γ surface

The results of the DFT calculation of the γ-surfaces are presented in Figure 4.2 and summarised in Table 4.1. Figure 4.2 shows some of the extremes in the calculated

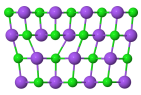

Phase	C1	C2	C3	C4	C5	C6
Ti_2AlC	0.282992	0.156480	-0.016174	0.001095	-0.001666	0.002269
Nb_2AlC	0.448371	0.149654	-0.032832	0.010283	0.001951	-0.001647
Ti_3SiC_2	0.518409	0.165415	-0.028071	0.007997	0.002995	-0.002455
Nb_2GaC	0.308173	0.149612	-0.029413	0.006746	0.002960	-0.002059
Nb_2InC	0.224446	0.155834	-0.023865	0.002967	0.002511	-0.001017
Nb_2SC	0.556995	0.151700	0.012813	0.016965	0.002000	0.002431
Nb_2SnC	0.306205	0.112250	0.013072	0.003043	-0.002861	-0.000279
Ti_2GaC	0.203826	0.106754	-0.015401	-0.000080	0.001344	-0.000344
Ti_2InC	0.212131	0.136290	-0.019126	0.001000	0.001751	0.000058
Ti_2SC	0.480254	0.326211	-0.041373	0.025800	0.001488	-0.000562
Ti_2SnC	0.295972	0.124439	-0.017660	0.002200	0.000554	-0.000501
Zr_2InC	0.091959	0.095488	0.010618	0.002890	-0.001593	-0.000152
Zr_2SC	0.255379	0.312817	-0.021624	0.016800	0.001213	0.000362
Zr_2SnC	0.257600	0.135233	-0.019346	0.002700	0.002464	-0.001410
Ti_3AlC_2	0.283378	0.137157	-0.009093	0.002380	-0.000999	-0.000026
Nb_4AlC_3	0.439674	0.140072	-0.031167	0.012671	0.000282	-0.001988
Ti_4SiC_3	0.503656	0.159172	-0.026991	0.007960	0.002571	-0.001520

Table 4.1: Results of the DFT simulation of the γ-surface for various MAX phases, presented as parameters for Equation 4.1.

γ-surfaces as well as the γ-surfaces of some of the more commonly studied MAX phases.

All the γ-surfaces showed a minimum at $\phi/b = 1/2$, the deepest minima were those in Ti_2SC and Zr_2SC. Interestingly the phase Nb_2SC does not show a similar, pronounced local minimum. The MAX phase closest to showing no local minimum in the stacking fault energy at the anti-phase position is Nb_2SnC, though even that phase has a small minimum. This minimum can be explained in terms of the crystal structure. Because the M–A is locally hexagonally close-packed there must exist a stacking fault that alters the sequence from ABA to ACA. This is likely to be a stable stacking fault, i.e. a local minimum in energy, by analogy with hexagonal metallic elements. The existence of the minimum in all the phases shows the importance of the relaxation of the atomic positions perpendicular to the misalignment displacement: a stacking fault could not be formed unless atoms were allowed to move normal to the imposed displacement.

The γ-surfaces show a similar trend to the shear moduli of the M–A layers, as discussed in Chapter 3. The sulphur bearing phases are the tallest and steepest as

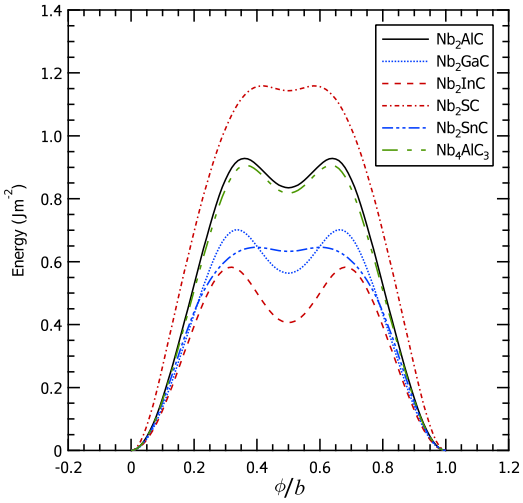

(a) The γ-surfaces for the niobium bearing MAX phases.

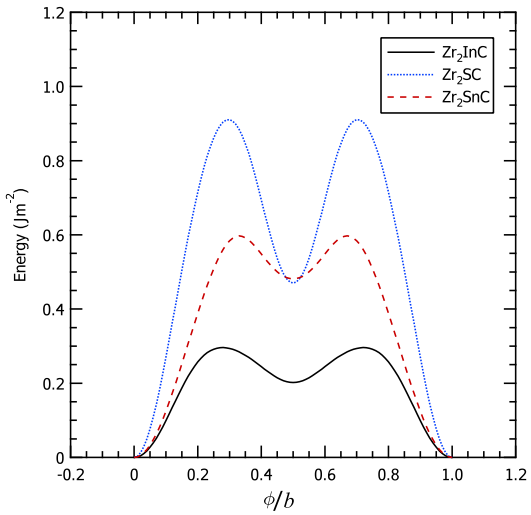

(b) The γ-surfaces for the zirconium bearing MAX phases.

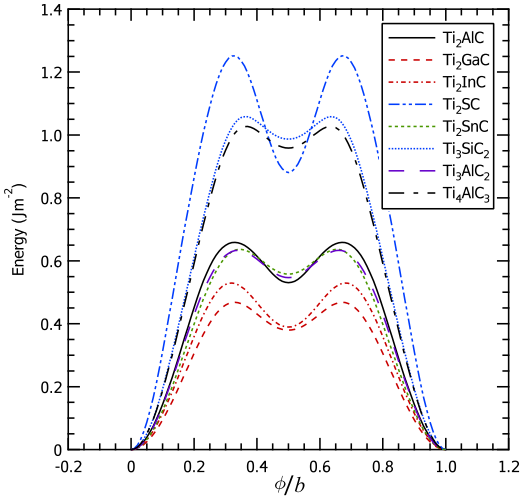

(c) The γ-surfaces for the titanium bearing MAX phases.

Figure 4.2: The γ-surfaces of the MAX phases, organised by the element occupying the M-site and plotted using the parameters given in Table 4.1 and the function given in Equation 4.1.

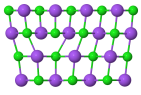

might be expected from the very low electronegativity difference in those phases, while indium bearing phases, which have the largest electronegativity differences, were the shallowest and other phases taking intermediate positions as expected. More detailed analysis of the γ-surfaces was undertaken by examining the effect upon the Peierls stress.

4.3.2 Lateral motion

The qualitative nature of the stacking faults was investigated with the VESTA visualisation software and SIESTA's crystal structure export functionality. A series of atomic configurations at increasing misalignments from a value of ϕ/b of 0 to 0.5 is shown in Figure 4.3.

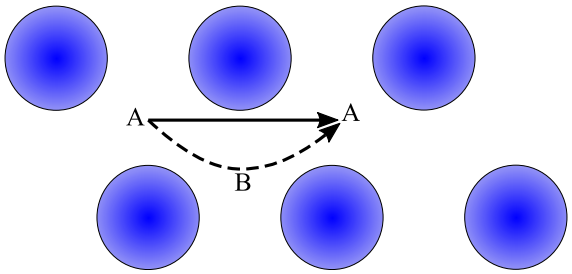

(a) Schematic showing a hexagonally packed layer of atoms analgous to the M or A layers in the MAX phase structure. The stable position for the next layer of atoms is the A site marked. If no lateral motion is allowed then as a stacking fault is created the next layer of atoms will follow the straight line from one site to the next. If lateral relaxation is allowed then a lower energy path might be via the other site, marked B, possibly giving rise to a stable stacking fault.

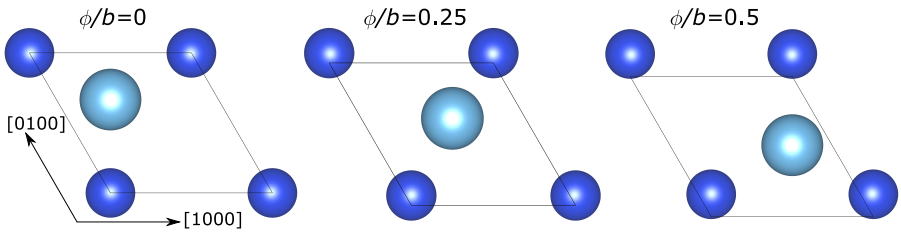

(b) The atomic positions as modelled in Ti_3SiC_2 projected down the [0 0 0 1] direction as a stacking fault is introduced by displacing a slab of crystal in the unit cell. The displacement, ϕ, is imposed parallel to [1 0 0 0] and varies from zero to half the Burgers vector, b. Atoms are allowed to relax normal to the [1 0 0 0]. The atoms shift from A site to the B site, and this is the stable stacking fault and is responsible for the local minimum in the stacking fault energy as seen in Figure 4.2. Graphics prepared with VESTA [74].

Figure 4.3: Diagrams showing the importance of lateral motion in stacking faults.

The two slabs either side of the stacking fault showed clear and substantial lateral displacements. This is shown in Figure 4.3 as layers that start initially offset by $1/3[\bar{1}\,1\,\bar{2}\,0]$ are aligned when the two slabs are displaced by $b/2$, i.e. half the re-

peat distance. This lateral motion, and subsequent change of the stacking sequence, represents the stable stacking fault. This is as expected by analogy with hexagonal close-packed structures. The combination of the lateral motion with the displacement parallel to the slip direction, $[1\,0\,\bar{1}\,0]$, means that the atoms follow a trajectory along the Burgers vectors of two partial dislocations as shown in Figure 4.3. This is exactly as would be expected from the similarity of the M–A layer to the hexagonal close-packed crystal structure.

4.3.3 Peierls stress

The Peierls stress is shown against the lattice geometry, as defined by d/b, in Figure 4.4. There is a huge range in the predicted Peierls stress: τ_p/G varies from 4.07×10^{-3} to 1.29×10^{-5} for Ti_2SC and Zr_2InC respectively. In absolute terms this is a range of $\sim$1 MPa to 690 MPa for those same phases. This range is reasonable: the weakest phase is Zr_2InC, which has the biggest difference in electronegativity and the lowest M–A shear modulus, of only 48.1 GPa, reflecting the lower energy profile of the GSF. The strongest phase is the sulphur bearing Ti_2SC, which has almost no electronegativity difference, and shows a much higher GSF and the highest M–A shear modulus, of 129.3 GPa. As discussed in Chapter 1, the Peierls stress All the calculated Peierls stresses are lower than would be expected from the lattice geometries, i.e. d/b, alone.

Some variation is expected as the lattice geometry changes across the MAX phases, as discussed in Chapter 3, increasing the electronegativity difference between the layers of the crystal structure leads to a shortening of the M–A bond length, which in turn reduces the value of d/b. The range in d/b observed in the MAX phases, about 0.5 to 0.75, would account for a reduction in τ_p/G by around a factor of 10 in an isotropic material, however the MAX phases exhibit a drop of around 300 times. Hence there is also a greater variation in the predicted Peierls stress than can be accounted for by the variation in the crystal structure alone.

The variation of the Peierls stress with the electronegativity difference across the

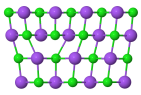

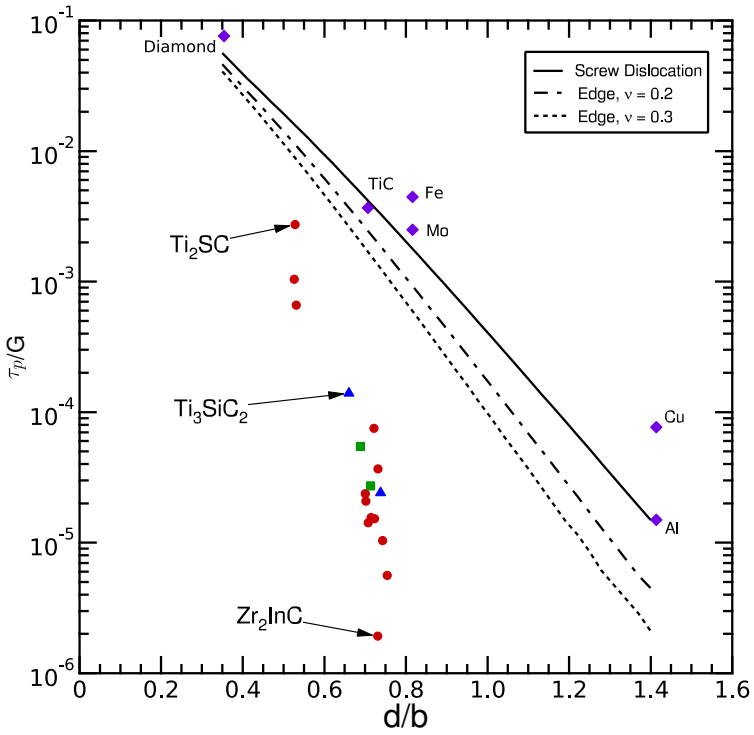

Figure 4.4: The calculated Peierls stress, normalised by the shear modulus, against d/b for the MAX phases. This defines the lattice resistance at 0 K. The circles, triangles and squares represent the 211, 312 and 413 phases respectively, the diamonds are some reference phases with simpler crystal structures, with values obtained from [37]. The lines show the prediction for an isotropic elastic medium for a screw dislocation and an edge dislocation for two different values of the Poisson ratio using the model published in [37].

structure is shown in Figure 4.5a. Increasing electronegativity difference between the M–X and the M–A layers clearly correlates well with a large decrease in the Peierls stress. As was discussed earlier, in Chapter 1, the structure of a dislocation is key to its properties. In particular the Peierls stress is exponentially dependent on the width of the dislocation core, with wide dislocations gliding easily and narrow dislocations exhibiting a large resistance. The variation of the dislocation width is shown against the electronegativity difference in Figure 4.5b and against the ratio of the shear moduli between the regions of the unit cell in Figure 4.5c.

Figure 4.5 shows that the structure of the dislocation is altered considerably across the range of MAX phases investigated which is expected to have a large impact on the Peierls stress as predicted by Peierls and seen in Figure 4.4. As discussed in section 1.1, the size of the dislocation is controlled by the competition between two energetic factors; firstly the strain energy in the crystal away from the slip plane favours a wide dislocation and secondly the misalignment energy in the

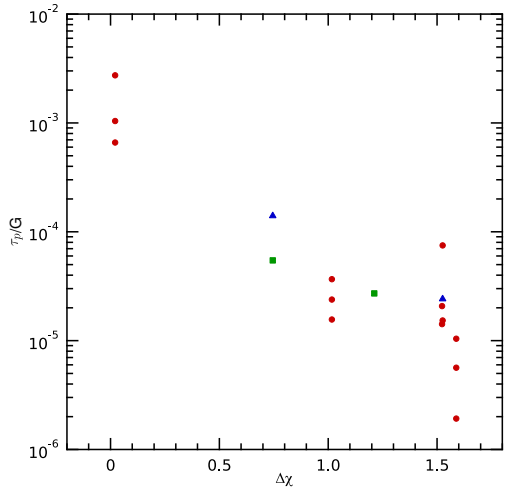

(a) The variation of normalised Peierls stress with the electronegativity difference within the crystal structure.

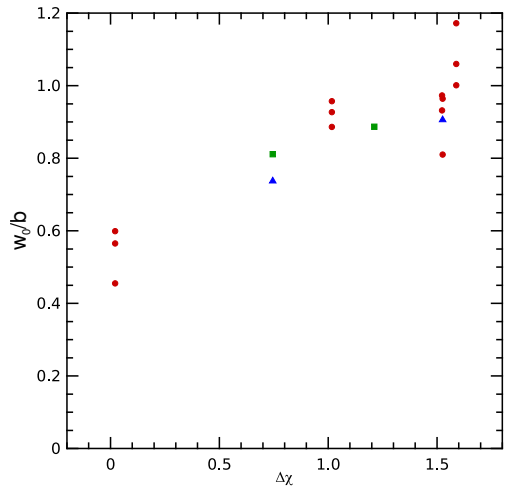

(b) The variation of the dislocation width, at the equilibrium position, with the difference in electronegativity between the layers of the MAX phase structure.

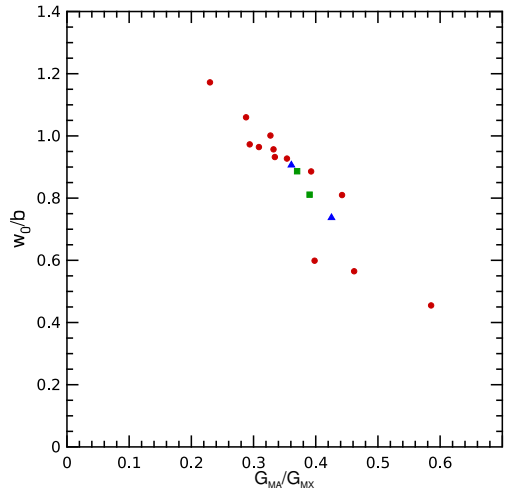

(c) The variation of the dislocation width, at the equilibrium position, with the ratio of the shear moduli of the M–A and M–X regions of the unit cell.

Figure 4.5: The link between the chemical heterogeneity, as expressed as an electronegativity difference between regions of the unit cell, and the Peierls stress. This dislocation geometry is dependent on the ratio of the moduli of the M–A and M–X layers, which is controlled by the electronegativity difference as discussed in Chapter 3.

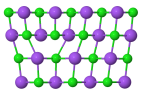

slip plane favours a narrow dislocation. In the MAX phases the local heterogeneity allows the introduction of a lower misalignment energy and a higher strain energy than would be expected, thus stabilising a wide dislocation core.

The strain energy term is raised because the electronegativity difference draws electrons into the M–X layer, stiffening it. Conversely the misalignment energy term, which is characterised crudely by the lower shear modulus or more accurately by the γ-surface, is lowered by the loss of electrons from the M–A layer which occurs under the influence of the electronegativity difference. Thus increasing the electronegativity difference increases the strain energy term and reduces the misalignment energy term, stabilising a wider dislocation and lowering the Peierls stress.

It is this local juxtaposition of the two heterogeneous regions so close together that creates this heterogeneity softening effect. If the heterogeneity were over a larger length scale than adjacent planes of atoms, the dislocations would be affected much less. The stiff region, which is responsible for the high in-plane strain energy in the MAX phases, would also have a high misalignment energy if the slip plane passed through it. Similarly the compliant region would have a low strain energy in addition to its low misalignment energy. This would lead to narrower dislocations in either region, and thus lead to a higher Peierls stress.

4.4 Conclusions

The generalised stacking fault energy, or γ-surface, of the MAX phases was investigated with density functional theory both quantitatively and qualitatively. As expected the heterogeneity of the unit cell had a strong influence on the γ-surface; very heterogeneous phases with a large electronegativity differences had low and shallow γ-surfaces and more homogenous MAX phases with lower electronegativity differences had higher and steeper γ-surfaces.

The importance of careful modelling of the γ-surface was demonstrated. Relaxation of the atomic positions laterally, i.e. perpendicular to the misalignment, created a metastable point in the γ-surface, associated with following the trajectory

of two partial dislocations rather than naïvely following the Burgers vector. All the phases exhibited this local minimum at the halfway position, corresponding to a stable stacking fault.

The γ-surfaces were used, along with the elastic results presented in Chapter 3, to calculate the Peierls stress with an adapted version of the Peierls model. The MAX phases were all softer than expected for phases with their lattice geometry and elastic moduli and showed a greater decrease in the Peierls stress with increasing d/b than expected.

The structure of the dislocations was examined and it was found that the increasing electronegativity difference, which drives the variation in the d/b ratio, the heterogeneity of the local elastic moduli and the nature of the γ-surfaces, is associated with the changes in the dislocation width. Increasing the local heterogeneity results in strengthening of the bonding in the electronegative M–X region and a weakening in the electropositive M–A region, which in turn raises the strain energy term driving wider dislocations and weakens the misalignment energy term driving narrower dislocations. This coupled effect stabilises wider dislocations which glide more easily.

That the low flow stresses in the MAX phases can be explained by the local heterogeneity in the unit cell suggests that controlled chemical heterogeneity in crystal is a route to tailoring the Peierls stress. Since the toughness in many non-metallic materials is limited by the force required to move dislocations, this is also a potential route to increasing the toughness of non-metallic materials.

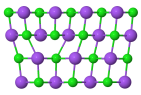

Chapter 5

The hardness of the Ti_2Ni structure

The previous chapters have attempted to address the behaviour of dislocations in almost ideal model systems, the alkali halides and the MAX phases. In particular the behaviour of the MAX phases presents a promising route to tailoring the flow stress of complex crystals, but the question remains as to whether these models of dislocation motion are applicable more broadly, and specifically to systems with a greater industrial relevance.

The MAX phases can accommodate chemically, and hence elastically, heterogeneous regions because the unit cells are large, at least parallel the c axis. This suggests that the unit cell of any candidate should be large, of the order of 10 Å. The MAX phases show very easy basal slip, but slip out of the basal plane is much harder, so any candidate phase will need to have higher crystal symmetry and must have enough independent slip systems to allow full plasticity. The MAX phases also allow a large range of heterogeneity to be investigated due to the wide range of stable compositions, so a range of alloying possibilities is necessary to investigate this softening effect based on elastic heterogeneity.

It is worth noting that the MAX phases are very anisotropic, whereas cubic crystals are likely to be more isotropic a result of their higher symmetry. The

anisotropy is relevant to the behaviour of dislocations, since the stiffness tensor is clearly relevant to controlling the strain energy around the dislocation, but the strong effects seen in the MAX phase are dependent on the spatial heterogeneity, the large reduction in stiffness from one region to another. There is no reason that similar heterogeneities cannot exist in cubic crystals, though since planes in cubic crystals will intersect other planes of the same type there may be a reduction in the degree of heterogeneity that arises.

The Ti_2Ni structure was selected because it meets these criteria. The structure has an FCC crystal lattice (space group $Fd\bar{3}m$) with 96 atoms in the unit cell and, for the case of titanium and nickel, a lattice parameter of 11.28 Å [150, 151]. The range of elements that can be incorporated into the structure is also large, a search using the Inorganic Crystal Structure Database (ICSD) [152] returned 103 results including elements such as sodium, zinc, germanium, niobium and hafnium, amongst others.

5.1 The Ti_2Ni structure

Phases with the Ti_2Ni structure have a large FCC unit cell with a lattice parameter of approximately 11 Å. The cell contains a large number of atoms and appears complex, a plan view is shown in Figure 5.1. However the symmetry of the structure is high, the space group is $Fd\bar{3}m$, and there are only three distinct sites; the Wyckoff positions for which are 16(c) (Ti1), 32(e) (Ni) and 48(f) (Ti2), which have the coordination numbers 12, 12 and 14 respectively. The packing and ordering of these clusters creates the face-centred symmetry. The creation of a face-centred structure, rather than an icosahedral packing as in quasicrystals, requires distorted icosahedral coordination polyhedra.

While in many phases, the conceptualisation of structure as clusters are simply a geometrical description [75], in the Ti_2Ni phases there is direct evidence that the bonding and properties are highly localised into the clusters, particularly the 16(c) site, at which, for Ti_2Ni, a titanium atom sits [153]. Ivanović, Rodić, Koteski et al.

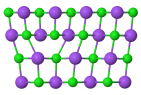

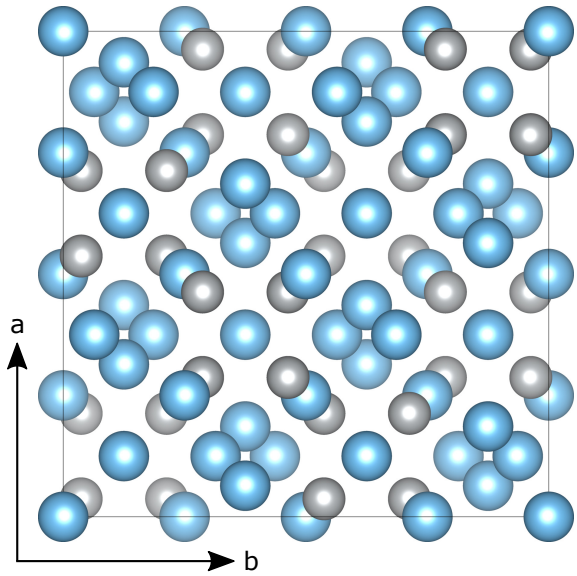

Figure 5.1: Plan view of the Ti_2Ni structure down the [0 0 1]. The larger blue atoms are titanium sites and the smaller silver atoms are nickel sites. Graphic prepared with VESTA [74].

[153] report the electric field gradient of the material to be extremely heterogeneous, showing different bonding at the two titanium sites, the 16(c) and the 48(f), just 3 Å apart.

The 16(c) coordination cluster is found to be the most stable, i.e. stronger bonding, and its bonding to have a metallic character. The cluster at the 32(e) site is less stable, i.e. weaker bonding, but has otherwise similar character to the coordination cluster at 16(c). The appearance of this cluster in both the Ti_2Ni structure and in a related quasicrystal support the idea that these clusters are a natural geometric complement to each other, i.e. the two arrangements pack well. The 48(f) arises in the crystalline state but not the quasicrystalline state, and so is likely to be a product of space filling in the Ti_2Ni crystal structure.

The 48(f) cluster shows a large variation of bond lengths among bonds of the same type. There are two different bond lengths between the Ti2 (48(f)) site and the Ni (32(e)) site, and two different bond lengths between neighbouring Ti2 sites. In contrast the Ti1 (16(c)) site has only two distinct bond lengths, one to the Ni site and one to the Ti2 site and the Ti-Ti bond from 16(c) to the 48(f) is the shorter than both of the Ti-Ti bonds between neighbouring 48(f) sites [150, 151, 153]. Ivanović, Rodić, Koteski et al. [153] ascribe this variation to weaker bonding.

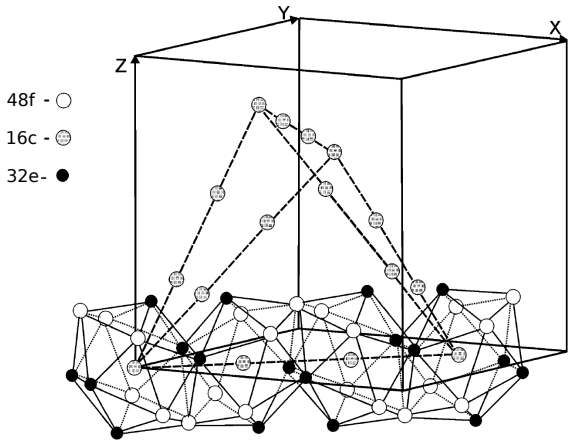

Figure 5.2: The network formed by the metallically bonded coordination clusters at the 16(c) site in the Ti_2Ni structure, reproduced from [153].

Here we are mainly interested in how these properties might influence to dislocation motion. Here we must consider broader regions of crystal rather than local clusters. If the clusters are physically significant structural units then the way these pack together will be key to the dislocation properties, just as in close-packed metals dislocations glide along particular crystallographic planes the same should be expected here. The 16(c) sites form chains, sharing faces and defining a large tetrahedron within the unit cell. This is in fact a Kagomé net, exactly as exists in the Laves phases [51, 52], parallel to the $\{1\,1\,1\}$ planes. The distinction is that the Kagomé net in the Laves phases are defined by single atomic sites rather than clusters. The Kagomé network of 16(c) clusters is shown in Figure 5.2

Dislocations are long, linear defects and so will respond to the properties of extended regions of a crystal. In other face-centred cubic intermetallics with large unit cells slip has been shown to occur on $\{1\,1\,1\}$ planes and in either $<1\,\bar{1}\,0>$ or $<1\,1\,\bar{2}>$ directions, in a simple analogy with FCC metals [154]. The $\{1\,1\,1\}$ planes are shown in Figure 5.3. It is clear that the heterogeneity inherent in the crystal is relevant to the slip system that is likely to operate in this structure since there are distinct layers in the structure when viewed in this way.

The view in Figure 5.3b shows a marked similarity with the Laves phase structure which similarly has a Kagomé layer and a puckered triple layer, albeit with shorter repeat distances. An important point is that the Kagomé layer formed by the 16(c)

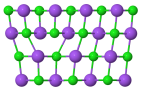

clusters is potentially physically significant within the crystal structure. The crystal can then be considered a network of intersecting Kagomé layers containing all of the 16(c) (Ti1) sites, all of the 32(e) (Ni) sites and a number of the 48(f) (Ti2) sites in the crystal and the space between is filled by the remaining 48(f) (Ti2) sites.

5.1.1 The alloying additions and effects

To assess the effect of alloying additions on the dislocations, salient regions of the crystal structure must be considered. The situation for Ti_2Ni is not as simple as the MAX phases considered in Chapter 4, which have a very distinct heterogeneous layered structure. Much of this complexity arises because any plane in a face-centred cubic structure will necessarily intersect with other planes of the same kind.

A simple model of the regions relevant to dislocations is shown in Figure 5.3a, where distinct layers are labelled showing a mixture of titanium and nickel in one region (the 16(c) clusters) and a purely titanium region in the other. These two layers together form one complete $\{1\,1\,1\}$ layer; the $\{1\,1\,1\}$ layers are stacked in the familiar ...ABCABC... sequence to form the complete structure.

The atom on the nickel site is usually the more electronegative, at least in the alloys considered here, and these sites are associated with the 16(c) cluster which is more strongly bonded than the other clusters, as would be expected. The ratio of Ni:Ti in the mixed region is 9:8, so by analogy with the MAX phases, see Equation 3.1, the electronegativity difference is

$$\begin{aligned} \Delta\chi &= \chi_{\text{mixed}} - \chi_{\text{Ti}} \\ \Delta\chi &= \frac{9\chi_{\text{Ni}} + 8\chi_{\text{Ti}}}{17} - \chi_{\text{Ti}} \end{aligned} \tag{5.1}$$

Hence variations in the electronegativity of the atoms will have a smaller effect on the electronegativity difference between the layers than in the MAX phases.

The Ti_2Ni structure can accommodate a wide variety of elements, but for ease of processing and material availability the compositions were limited to those given

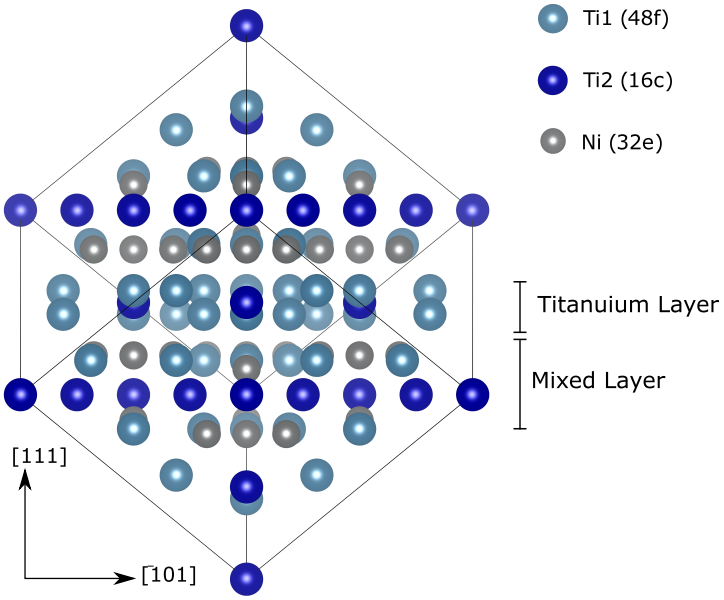

(a) A view of the Ti_2Ni unit cell showing the {1 1 1} planes with the perfect burgers vector, $[\bar{1}\,0\,1]$, across the diagram.

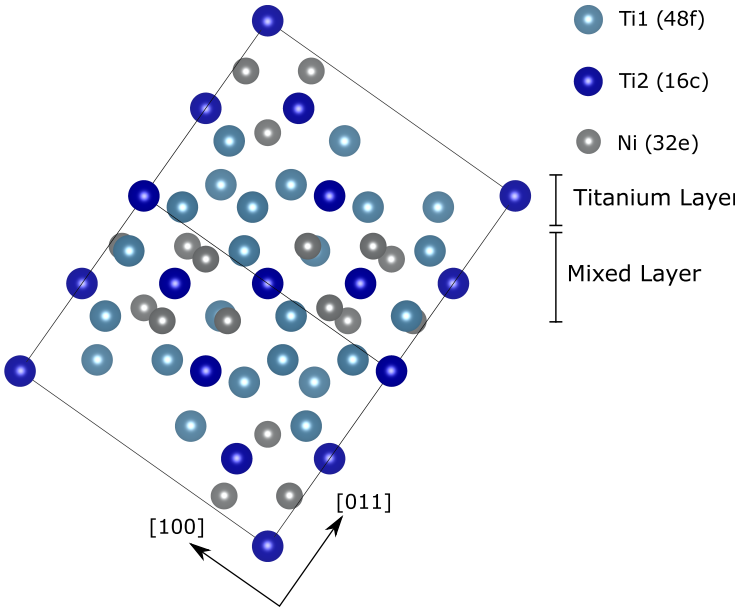

(b) A view of the Ti_2Ni structure showing the {1 1 1} planes looking down the $\langle\bar{1}\,0\,1\rangle$ direction.

Figure 5.3: The {1 1 1} layers of the Ti_2Ni structure projected along two different directions. Graphics prepared with VESTA [74].

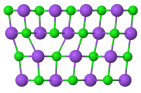

Stoichiometry	$\Delta\chi$ (eV)
Ti_2Ni	0.444
Ti_2Co	0.383
Hf_2Co	0.378
$Ti_2(Co, Ni)$	0.414
$(Hf, Ti)_2Ni$	0.440

Table 5.1: The compositions used to investigate plasticity in the Ti_2Ni structure and the corresponding electronegativity (Mulliken scale [136]) difference between the regions shown in Figure 5.3.

in Table 5.1.

5.2 Sample preparation

Samples were prepared by arc melting pieces of the pure elements to form small, roughly cylindrical ingots of around 40 g. These ingots were then directionally solidified using the optical floating zone technique.

In the floating zone technique, light is focused onto a small region of a cylindrical sample to form a molten zone, the zone is then translated along the length of the sample either by moving the light or by moving the sample. The zone can be passed along the sample once or multiple times in either the same direction or alternating the direction of travel to achieve different ends [155].

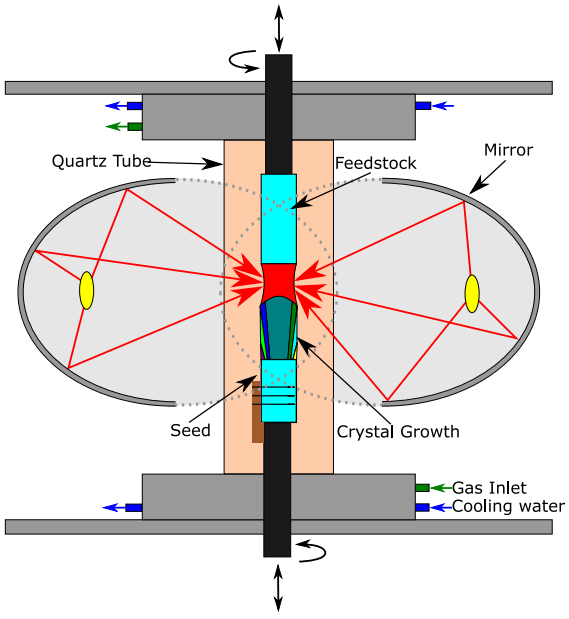

Figure 5.4: Schematic of an optical floating zone furnace.

Nominal Phase	Primary Phase (at%)	Secondary Phase (at%)
Ti_2Ni	67.5Ti 32.5Ni	47.7Ti 52.3Ni
Ti_2Co	66.5Ti 33.5	51.1Ti 28.9Co
Hf_2Co	70.3Hf 29.7Co	51.5Hf 48.5Co
$Ti_2(Ni, Co)$	67.7Ti 16.4Co 15.9Ni	52.8Ti 26.7Co 20.4Ni
$(Ti, Hf)_2$ Ni	36.7Hf 34.6Ti 28.7Ni	25.0Hf 20.7Ti 54.3Ni

Table 5.2: Compositions of the phases present in samples as measured by EDX, an average of 12 point scans for each phase.

The floating zone furnace used was a FZ-T-12000-X-VPO (Crystal Systems Corp). This system uses four xenon arc lamps, each with an ellipsoidal mirror to focus the light onto the sample, a schematic is shown in Figure 5.4. The samples were all grown with the seed and feedstock counter rotating at 15 rpm, i.e. 30 rpm relative rotation, and a growth rate of $20\,\mathrm{mm\,h^{-1}}$.

The sample surfaces were ground flat with silicon carbide paper before polishing with a series diamond pastes from 6 µm to a 0.25 µm finish and finally finished with ten minutes of polishing with a 1:1 solution of colloidal silica and water for a final finish of $\sim$0.05 µm.

The compositions of the phases were checked by energy dispersive x-ray spectroscopy (EDX) using an Oxford Instruments system. The compositions were found to be the same as the nominal compositions for all samples, within the experimental error of this experimental technique.

The measured compositions of the primary phases and any secondary phases present are presented in Table 5.2

5.3 Mechanical testing

Investigating the plastic flow of brittle materials is a challenging problem which has seen much investigation in recent years. Various techniques exist to investigate plasticity in materials that are likely to fracture in conventional testing: for example a constraining hydrostatic pressure [156–158], micropillar compression where the size effects suppress fracture [159] and indentation [160–163]. Of these the indentation hardness test is the simplest experimentally. In contrast constraining pressure

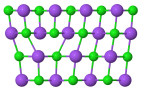

equipment is complex, the high pressures can induce phase changes and uniaxial properties can only be extrapolated to lower hydrostatic stresses and the hydrostatic pressure is known to affect plastic flow [114]. Micropillar compression, while creating a uniaxial stress state, is known to be strongly influenced by size effects [159, 164, 165].

5.3.1 Nanoindentation

When indenting brittle materials small indents are likely to be necessary to suppress cracking, this must be achieved by instrumented indentation. In instrumented indentation the load and the depth are measured throughout the experiment as opposed to measuring the area of the residual indent. However this risks encountering the indentation size effect [160, 163]. To be comparable the indents must all be the same size, and the samples prepared to the same finish by the same method. The size effect can also be characterised by a set of indents at a range of depths, though identifying the actual causes of the effect is difficult. The range of possible causes includes surface layers of oxides, residual stresses in the surface, strain hardening from surface preparation and friction between the indenter and the material surface [160]. Even if all these effects are eliminated or minimised there is a material effect in crystalline materials: at small length scales the indentation hardness is dominated by the the nucleation of geometrically necessary dislocations [160].

To ensure that the results from the indent were comparable across the different samples the crystallographic orientation of the grains in the material was identified by electron backscatter diffraction (EBSD) using a Camscan MX2600 FEGSEM and only those grains close to a single orientation were considered. This ensures that, although the stress state under a Berkovich indenter is complex, the orientation between the stress state and the slip systems is at least similar for all the indents, thus minimising any Schmid factor effects that might affect the hardness when indenting different crystal faces [4]. The <1 1 1> was a common growth direction and so only indents into grains oriented within 10° of the <1 1 1> were used in the analysis,

others were discarded.

Indentation was undertaken with a Micromaterials NanoTest indenter using a Berkovich tip, with the assistance of James Campbell. Thermal drift was minimised by heating a chamber containing both the sample and the indenter to 25 °C and allowing the temperatures to equilibrate. The indents were performed under depth control at a loading rate of $5\,\mathrm{nm\,s^{-1}}$. To probe the depth dependence of the hardness, indents were performed at intervals of c. 100 nm between 100 nm and 1700 nm. Larger datasets were collected to more accurately determine the hardness on known crystallographic faces, as determined by EBSD. The simplest method to achieve this was to produce a square array of widely spaced indents across the surface and investigate the crystal orientation ex-situ. These indents were performed under the same conditions to a depth of 1 µm.

5.3.2 Micropillar compression

While micropillar compression has not been employed to compare the flow properties of the different phases in this work the technique has been used to identify the active slip systems of the Ti_2Ni structure. This can be achieved by milling pillars in an area of the crystal that has been mapped with EBSD.

Pillars were milled into the sample surface using a focused ion beam microscope (FIB), the system used was a FEI Helios NanoLab with Ga^+ ions operated with the help of Claire Davis and Robert Jones. The pillars were milled to be approximately 2 µm in diameter and 5 µm tall. The pillar was milled in a series of steps, consisting of concentric annuli at decreasing beam currents. The details are given in Table 5.3.

Outer Diameter (µm)	Inner Diameter (µm)	Current (nA)	Z-Depth (µm)
12	4	2.8	1.8
4.7	2.5	0.46	0.7
2.7	2	0.048	0.4

Table 5.3: The outer diameter and inner diameter define the area milled at each current, Z-depth defines the required depth at each stage and will automatically adjust the milling time.

Compression of the micropillars was performed with an in-situ Alemnis indenter

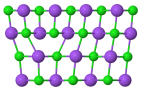

with a diamond flat punch tip operated by Robert Jones. A detailed description of the experimental and analysis procedures can be found in [154].

The slip trace on the pillar can be used to determine the slip plane by comparison with the crystal structure using a visualisation package such as VESTA [74, 154]. The slip direction can be determined by finding the lattice vector parallel to the lateral (i.e. perpendicular to the compression axis) movement during slip and projecting this onto the slip plane, however this can be difficult in FCC systems where likely slip vectors are relatively close together, e.g. <1 0 1> and the <1 1 2> [154].

5.4 Results and Discussion

5.4.1 Size effect

The size effect was investigated first; the results for Ti_2Ni and Ti_2Co are shown in Figure 5.5. At very low depths (at maximum load) the hardness is very high due to the size effect [160], in excess of 60 GPa for indents at a depth of ∼100 nm. The hardness drops with increasing indent depth and plateaus when the depth is at least a micron. Hence to ensure comparable results that limit the influence of size effects on the results the indents used to compare the flow stresses were all performed to a depth of 1 µm.

At the largest depths Ti_2Co shows an increased scatter in the results with a lower mean value, which could be indicative of the onset of cracking beneath the indenter tip, at least in some of the indents performed. This implies that the depth range 800 nm to 1400 nm is probing the plastic flow properties of the material, rather than nucleation of geometrically necessary dislocations in the case of smaller depth, or the fracture toughness in the case of larger indents. The depth of approximately 1 µm, which corresponded to a maximum load of around 200 mN, was used for all the subsequent indents to ensure the results reflect this plastic regime.

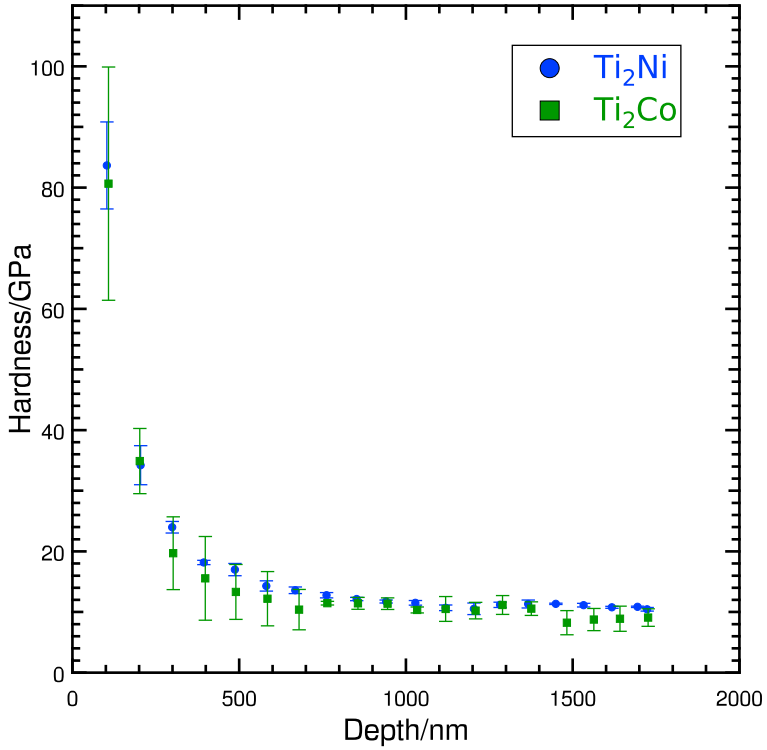

Figure 5.5: The effect of indent depth (at maximum load) on the measured hardness for Ti_2Ni and Ti_2Co using a Berkovich indenter on a Micromaterials NanoTest rig. The hardness values are high at low depths as predicted by the size effect [160] and plateau at around 800 nm.

5.4.2 Slip plane

Micropillars were milled in Ti_2Ni, characterised with EBSD and compressed in-situ. The compressed pillars were imaged by SEM and showed slip traces on the surface. The micrographs are shown in Figure 5.6. The compression axis was found to be approximately parallel to the [1 1 6] direction. Slip traces developed on the surface of the micropillar as deformation occurred. There are two slip systems, of the expected type $[1\,0\,\bar{1}](1\,1\,1)$, with the largest Schmid factor, the $[1\,0\,1](\bar{1}\,1\,1)$ and the $[0\,1\,1](1\,\bar{1}\,1)$, so the slip trace was examined to see if either of these slip systems match. This was done with the crystallographic visualisation package VESTA [74] which can align unit cells to a known three dimensional orientation and show the orientation of lattice planes. The visualisations are also shown in Figure 5.6 next to the corresponding view of the micropillar.

This is an important result as it justifies the calculation for the electronegativity difference of the structure as the difference between the planes of atoms parallel to

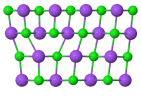

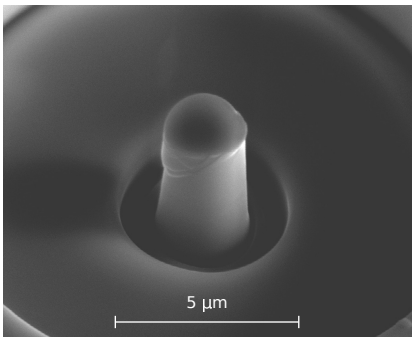

(a) First view of the compressed Ti_2Ni micropillar. The scale bar is approximately parallel to [0 5 $\bar{1}$]

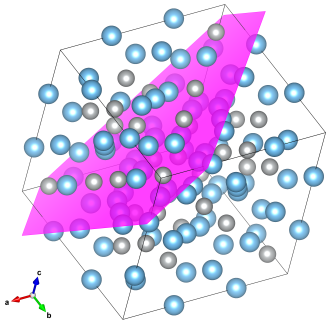

(b) The unit cell aligned with the EBSD results and adjusted for tilt during imaging for the first orientation showing the expected slip plane, (1 $\bar{1}$ 1).

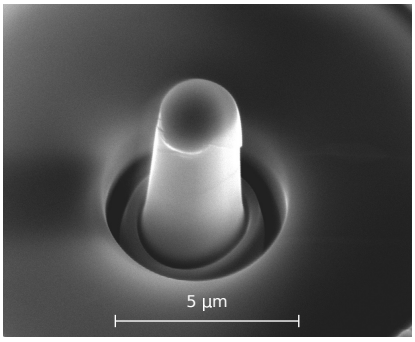

(c) Second view of the compressed Ti_2Ni micropillar. The scale bar is approximately parallel to [6 0 $\bar{1}$]

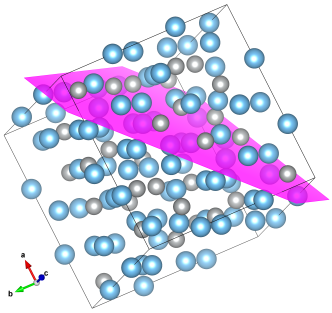

(d) The unit cell aligned with the EBSD results and adjusted for tilt during imaging for the second orientation showing the expected slip plane, (1 $\bar{1}$ 1).

Figure 5.6: A compressed micropillar in Ti_2Ni showing the expected slip plane, (1 $\bar{1}$ 1), for the compression axis [1 1 6].. Graphics prepared with VESTA [74].

the {1 1 1}, as shown in Figure 5.3a.

5.4.3 Hardness results

The hardness values for each phase are presented in Figure 5.7 and summarised in Table 5.4. Figure 5.7 shows that the increasing electronegativity difference has a substantial impact on the hardness of phases with the Ti_2Ni structure. As the electronegativity difference between the layers of the Ti_2Ni structure increases the measured hardness decreases, as expected by analogy with the MAX phases.

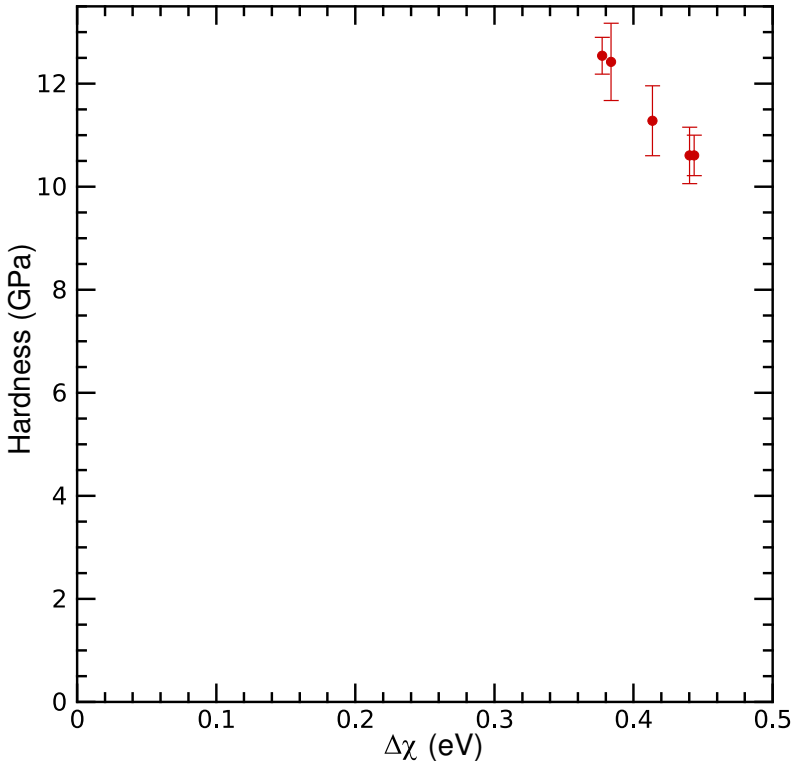

Figure 5.7: The variation of hardness, as measured with a Berkovich indenter, with electronegativity (Mulliken scale [136]), a reduction in hardness of almost 2 GPa or 16 % is seen for a modest variation in electronegativity.

All the alloys tested were hard, but a significant variation was observed, with the hardness varying between 10.6 and 12.6 GPa. The substitution of nickel with cobalt produced the biggest change in hardness, between Ti_2Ni and Ti_2Co the hardness drops 1.81 GPa, or 14.6 %, from 12.42 GPa to 10.61 GPa, as might be expected given the change in electronegativity difference this substitution gives rise to.

The substitution of hafnium for titanium has a smaller effect on the electronegativity difference between the layers and a correspondingly smaller effect on the

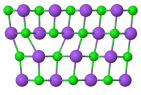

Stoichiometry	Hardness (GPa)	Std. Dev. (GPa)	n	$\Delta\chi$ (eV)
Ti_2Ni	10.61	0.38	30	0.444
$(Hf, Ti)_2Ni$	10.61	0.55	10	0.440
$Ti_2(Co, Ni)$	11.28	0.68	17	0.414
Ti_2Co	12.42	0.75	9	0.383
Hf_2Co	12.54	0.36	12	0.378

Table 5.4: The hardness results for the different stoichiometries with the Ti_2Ni structure.

hardness, Ti_2Co and Hf_2Co differ by 0.12 GPa, which is of the order of the error in the hardness measurement. In the case of Ti_2Ni and $(Hf, Ti)_2Ni$ there is no measured change in the hardness in either direction, which might be expected for the small change in the electronegativity difference, less than 0.01 eV.

The mixed stoichiometries, $Ti_2(Co, Ni)$ and $(Hf, Ti)_2Ni$ fit the trend well and do not exhibit any solution hardening as might be expected. Particularly noteworthy is that $Ti_2(Co, Ni)$ has an intermediate value of electronegativity difference and falls on the trend between the the extreme cases.

5.5 Conclusions

The effects heterogeneity at the unit cell level on deformation behaviour have been explored in phases with the face-centred cubic Ti_2Ni structure. The crystallography of the structure has been examined and the likely heterogeneous regions identified as the planes parallel to the $\{1\,1\,1\}$. These planes are made up of strongly bound clusters at the 16(c) position, which form a Kagomé network. The electronegativity difference between the regions of the unit cell was found to be likely to strengthen the bonding of this network, which contains atoms like nickel and cobalt on the 16(c) site. Stoichiometries were identified to explore a range electronegativity differences using the elements Hf, Ti, Ni and Co, varying $\Delta\chi$ over the range 0.378 eV to 0.444 eV.

The slip system in the Ti_2Ni was characterised by the compression of micropillars with a known crystallographic orientation as determined by EBSD. The slip plane was found to be the $\{1\,1\,1\}$. This is an important result, if slip were on some other plane, then the heterogeneity between regions of the crystal parallel to the $\{1\,1\,1\}$

planes would not be relevant.

Hardness measurements by nanoindentation were undertaken to characterise the size effect. The effect was shown to be limited to indent depths of less than ∼800 nm. Further indents were made on known crystallographic faces of the crystal to characterise the ease of plastic flow. Faces close to the {1 1 1} were indented to minimise the effects of varying Schmid factors. The hardness varied significantly with changing electronegativity, a change in $\Delta\chi$ of 0.066 eV produced a softening of 1.93 GPa, or 15.4 %

Though more modest in scale than the effects seen in the MAX phases, where the range of $\Delta\chi$ varies from 0.02 eV to 1.59 eV, the Ti_2Ni structure has demonstrated the same heterogeneity softening: hardness decreases as the composition is varied to increase the chemical, and thus elastic, heterogeneity within the unit cell. This demonstrates the effect of heterogeneity softening in a cubic structure. Cubic materials are not limited to a small number of slip systems like the hexagonal MAX phases, suggesting that sub-unit cell elastic heterogeneity offers a route to tailoring the macroscopic ductility and thereby the toughness of non-metallic materials.

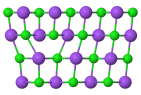

Chapter 6

Conclusions and future work

In this work the plastic behaviour of crystals has been investigated by use of the Peierls model. A new Peierls model has been created using Python and the associated projects, Numpy and Scipy, that allows the creation of a two or three dimensional Peierls model rather than one dimension as in previous models.

Calculations based on linear elasticity and a misalignment potential were in qualitative agreement with experimental observations though quantitative results were not reliable. The model predicts the observed softening in cementite as hydrogen is added via the changes in the single crystal elastic constants as calculated by density functional theory.

Dislocations in ionic solids were investigated, firstly with a Python implementation of the electrostatic and Lennard-Jones energy calculations. This implementation was deliberately without modification for computational ease to avoid the introduction of artefacts or complications. This was to ensure the results were as interpretable as possible.

It was shown for the $<1\,1\,0>\{0\,0\,1\}$ slip system in sodium chloride that the short range repulsion energy, here modelled by the Lennard-Jones potential, and the electrostatic energy were sufficient to predict the observed Peierls stress. As the dislocation moved the energy components were shown to vary out of phase, an analogy of the strain and misalignment energy components of elasticity based Peierls models.

The $<1\,1\,0>\{1\,\bar{1}\,0\}$ slip system could not be adequately described by the model, showing much larger energy changes than expected and unlikely variations in the dislocation width. The size of the simulation and the effects of boundaries were shown not to be responsible for these observations by the use of LAMMPS to simulate larger simulation cells with periodic boundary conditions. There is clearly at least one important factor in the behaviour of dislocations on this slip system that is not accounted for in the model presented here. Two possible factors are core reconstruction or the lack of polarisability in the atomic potentials.

The complex crystal structures of the MAX phases were considered. These phases have clear chemical heterogeneity within the unit cell, which density functional theory calculations showed give rise to elastic heterogeneity. These results were in agreement with the macroscopic properties when combined in a slab model. The properties of these layers were shown to vary with the chemical nature of the layers, as characterised by the electronegativity, where the macroscopic properties did not.

These elastic properties and the calculated generalised stacking fault energy were used in an adapted Peierls model to predict the Peierls stress of the MAX phases. The calculated Peierls stresses are in good agreement with the observed easy flow in the MAX phases, which is not adequately explained by the macroscopic elastic properties alone. The effect was shown to be strong, with τ_p/G varying by five orders of magnitude as the electronegativity difference between the layers of the structure vary by 1.566 eV from 1.588 eV to 0.0214 eV. This shows that the local elastic heterogeneity, induced by a local chemical heterogeneity, on the scale of the dislocation core, can offer a route to tailoring the flow stress of complex crystals.

The effect was also investigated in the Ti_2Ni structure, which is a complex metallic alloy with a large unit cell. The slip system was investigated by micropillar compression, and slip was shown to occur on the $\{1\,1\,1\}$ planes. The slip direction was harder to determine conclusively but the partial $<2\,\bar{1}\,\bar{1}>$ is more likely than the full $<1\,\bar{1}\,0>$. A series of alloys were chosen to alter the chemical heterogeneity of the

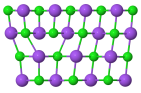

$\{1\,1\,1\}$ planes.

The flow stress of the alloys was tested by nanoindentation of the $\{1\,1\,1\}$ face of single crystals to ensure the Schmid factor remained constant. The hardness of the alloys varied significantly even though the range of heterogeneity was far smaller than that of the MAX phases; a reduction of $\sim$2 GPa from 12.5 GPa to 10.6 GPa or about 15 % was observed for a change in the electronegativity difference of just 0.066 eV.

There are two clear avenues for future work: an experimental route and a modelling route. Experimentally the best validation of the model would be to confirm the Peierls stresses at cryogenic temperatures. The MAX phase results presented here agree with those experimental results that exist, i.e. that the flow stress of Ti_2SiC_3 at room temperature is around 70 MPa which is similar to soft metals. However no direct evidence of the Peierls stress in the MAX phases has been produced to date.

Another obvious route for experimental work to build on this study, which assumes that the conclusions drawn here are valid, is to attempt to find a system that might be more industrially relevant. The Ti_2Ni results are important because they show the effect occurs in an cubic structure with enough slip systems that full plasticity is possible, unlike in the hexagonal MAX phases. However the reduction of the hardness from over 12 GPa to over 10 GPa is clearly insufficient to produce an alloy with enough ductility to be useful as a structural material.

Instead the best opportunities will be phases that are nearly sufficiently ductile, such that modification will more easily reach the critical point at which the alloy is tough enough for use as a structural material. In particular aluminium bearing intermetallics, such as tantalum aluminides which have large face-centred cubic crystal structures, would have sufficient corrosion resistance for higher temperature applications.

The modelling aspects of the project could be taken forward in a number of ways. The initial creation of the atomic arrays could be improved. Screw dislocations have not been considered and the behaviour of screw dislocations can be quite different

to edge dislocations.

Core reconstruction could be addressed by allowing atoms that fall within some core region to have their coordinates optimised directly, while atoms outside of this core are assumed to follow the functional form outlined in this work.

Another improvement would be to integrate the "atomic simulation environment" into the energy calculation. This is a library that allows the use of Python to set up simulations and analysis of the results but integrates more efficient external projects for atomic calculations. A variety of molecular dynamics and quantum mechanical packages are available such that the most appropriate one could be used. For example, this would allow the investigation of polarisability of atoms in ionic materials more easily than the method used thus far.

In summary, a Peierls model has been built with Python to extend the model to three dimensions, allowing the use of energy calculation methods such as interatomic potentials or the full elastic tensor. The effect of changing the stiffness tensor as hydrogen was added to cementite was shown to significantly soften the structure. Dislocations in ionic solids were modelled with partial success, fitting the hard slip system well but did not describe the behaviour of the soft slip system well. The behaviour of the MAX phases was investigated; DFT was used to show that elastic heterogeneity arises as a result of local chemical heterogeneity, as measured by electronegativity differences across the unit cell. The effect of this elastic heterogeneity on the Peierls stress was found to explain the anomalously low flow stresses observed experimentally. This effect was investigated experimentally in a series of alloys with the Ti_2Ni structure where the same softening was observed; as the chemical heterogeneity increased the hardness dropped. This shows that heterogeneity softening can occur in cubic crystals, presenting a possible route to tailored flow properties in complex crystals.

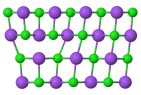

References

[1] E. Reusch, "Ueber eine besondere Gattung von Durchgängen im Steinsalz und Kalkspath," *Annalen der Physik und Chemie*, vol. 208, no. 11, pp. 441–451, 1867. DOI: 10.1002/andp.18672081106.

[2] J. A. Ewing and W. Rosenhain, "Experiments in Micro-Metallurgy: Effects of Strain. Preliminary Notice," *Proceedings of the Royal Society of London (1854-1905)*, vol. 65, pp. 85–90, 1899. DOI: 10.1098/rspl.1899.0004.

[3] J. A. Ewing and W. Rosenhain, "Bakerian Lecture: The Crystalline Structure of Metals.," *Proceedings of the Royal Society of London (1854-1905)*, vol. 65, no. -1, pp. 172–177, 1899. DOI: 10.1098/rspl.1899.0021.

[4] A. Kelly and K. M. Knowles, "Glide and Texture," in *Crystallography and Crystal Defects*, 2nd ed., Chichester, UK: John Wiley & Sons, Ltd, 2012, ch. 7, pp. 197–239. DOI: 10.1002/9781119961468.ch7.

[5] P. W. Bridgman, "The Effect of Hydrostatic Pressure on the Fracture of Brittle Substances," *Journal of Applied Physics*, vol. 18, no. 2, pp. 246–258, 1947. DOI: 10.1063/1.1697610.

[6] H. J. Frost and M. F. Ashby, *Deformation-mechanism maps: the plasticity and creep of metals and ceramics*. Pergamon Press, 1982.

[7] D. J. Rowcliffe and G. E. Hollox, "Hardness anisotropy, deformation mechanisms and brittle-to-ductile transition in carbide," *Journal of Materials Science*, vol. 6, no. 10, pp. 1270–1276, 1971. DOI: 10.1007/BF00552040.

[8] M. Darot, Y. Gueguen, Z. Benchemam, and R. Gaboriaud, "Ductile-brittle transition investigated by micro-indentation: results for quartz and olivine," *Physics of the Earth and Planetary Interiors*, vol. 40, no. 3, pp. 180–186, 1985. DOI: 10.1016/0031-9201(85)90128-1.

[9] Y. Harada and M. Ohmori, "Ductile-brittle transition behavior of rolled chromium," *Journal of Materials Processing Technology*, vol. 153-154, no. 1-3, pp. 93–99, 2004. DOI: 10.1016/j.jmatprotec.2004.04.011.

[10] J. W. Christian, "Some surprising features of the plastic deformation of body-centered cubic metals and alloys," *Metallurgical Transactions A*, vol. 14A, no. 7, pp. 1237–1256, 1983. DOI: 10.1007/BF02664806.

[11] C. R. Weinberger, G. J. Tucker, and S. M. Foiles, "Peierls potential of screw dislocations in bcc transition metals: Predictions from density functional theory," *Physical Review B*, vol. 87, no. 5, p. 054 114, 2013. DOI: 10.1103/PhysRevB.87.054114.

[12] A. Cottrell, "Surprises in materials science," *Interdisciplinary Science Reviews*, vol. 22, no. 4, pp. 318–324, 1997. DOI: 10.1179/isr.1997.22.4.318.

[13] J. P. Hirth and J. Lothe, "Introductory material," in *Theory of Dislocations*, 2nd ed., New York: John Wiley & Sons, Ltd, 1982, ch. 1, pp. 3–28.

[14] J. E. Gordon, "Cracks and Dislocations," in *The New Science of Strong Materials: Or Why You Don't Fall Through the Floor*, Second, Penguin Books Limited, 1991, ch. 4, pp. 77–98.

[15] E. Orowan, "Zur Kristallplastizität. I - Tieftemperaturplastizität und Beckersche Formel," *Zeitschrift für Physik*, vol. 89, no. 9-10, pp. 605–613, 1934. DOI: 10.1007/BF01341478.

[16] E. Orowan, "Zur Kristallplastizität. II - Die dynamische Auffassung der Kristallplastizität," *Zeitschrift für Physik*, vol. 89, no. 9-10, pp. 614–633, 1934. DOI: 10.1007/BF01341479.

[17] E. Orowan, "Zur Kristallplastizität. III - Uber den Mechanismus des Gleitvorganges," *Zeitschrift für Physik*, vol. 89, no. 9-10, pp. 634–659, 1934. DOI: 10.1007/BF01341480.

[18] G. I. Taylor, "The Mechanism of Plastic Deformation of Crystals. Part I. Theoretical," *Proceedings of the Royal Society A: Mathematical, Physical and Engineering Sciences*, vol. 145, no. 855, pp. 362–387, 1934. DOI: 10.1098/rspa.1934.0106.

[19] M. Polanyi, "ÜBER EINE ART GITTERSTÖRUNG, DIE EINEN KRISTALL PLASTISCH MACHEN KÖNNTE," *Zeitschrift für Physik*, vol. 89, no. 9-10, pp. 660–664, 1934. DOI: 10.1007/BF01341481.

[20] V. Volterra, "Sur l'équilibre des corps élastiques multiplement connexes," *Annales scientifiques de l'École normale supérieure*, vol. 24, pp. 401–517, 1907. DOI: 10.24033/asens.583.

[21] A. E. H. Love, *A Treatise on the Mathematical Theory of Elasticity*, 3rd ed. Cambridge: Cambridge University Press, 1920.

[22] J. M. Burgers, "Some considerations on the fields of stress connected with dislocations in a regular crystal lattice," *Proceedings of the section of sciences / Koninklijke Nederlansche Akademie van Wetenschappen*, vol. 42, pp. 378–399, 1939.

[23] A. Forty, "Direct observations of dislocations in crystals," *Advances in Physics*, vol. 3, no. 9, pp. 1–25, 1954. DOI: 10.1080/00018735400101153.

[24] F. C. Frank, "The influence of dislocations on crystal growth," *Discussions of the Faraday Society*, vol. 5, no. 48, p. 48, 1949. DOI: 10.1039/df9490500048.

[25] L. Griffin, "Observation of unimolecular growth steps on crystal surfaces," *The London, Edinburgh, and Dublin Philosophical Magazine and Journal of Science*, vol. 41, no. 313, pp. 196–199, 1950. DOI: 10.1080/14786445008521781.

[26] F. H. Horn, E. F. Fullam, and J. S. Kasper, "Holes in Crystals," *Nature*, vol. 169, no. 4309, pp. 927–928, 1952. DOI: 10.1038/169927a0.

[27] A. Cottrell, "Theory of dislocations," *Progress in Metal Physics*, vol. 1, pp. 77–126, 1949. DOI: 10.1016/0502-8205(49)90004-0.

[28] J. W. Menter, "The Direct Study by Electron Microscopy of Crystal Lattices and their Imperfections," *Proceedings of the Royal Society A: Mathematical, Physical and Engineering Sciences*, vol. 236, no. 1204, pp. 119–135, 1956. DOI: 10.1098/rspa.1956.0117.

[29] U. Dehlinger and A. Kochendörfer, "Eigenbewegungen in Kristallgittern," *Zeitschrift für Physik*, vol. 116, no. 9-10, pp. 576–585, 1940. DOI: 10.1007/BF01329753.

[30] R. Peierls, "The size of a dislocation," *Proceedings of the Physical Society*, vol. 52, no. 1, pp. 34–37, 1940. DOI: 10.1088/0959-5309/52/1/305.

[31] F. R. N. Nabarro, "Dislocations in a simple cubic lattice," *Proceedings of the Physical Society*, vol. 59, no. 2, pp. 256–272, 1947. DOI: 10.1088/0959-5309/59/2/309.

[32] A. H. Cottrell, "Dislocations in crystals," in *Dislocations and plastic flow in crystals*, R. Fowler, P. Kapitzer, N. Mott, and E. Bullard, Eds., First, Oxford University Press, 1953, ch. 3, pp. 58–98.

[33] J. Frenkel, "Zur Theorie der Elastizitätsgrenze und der Festigkeit kristallinischer Körper," *Zeitschrift für Physik*, vol. 37, no. 7-8, pp. 572–609, 1926. DOI: 10.1007/BF01397292.

[34] J. P. Hirth and J. Lothe, "The influence of lattice periodicity," in *Theory of Dislocations*, 2nd ed., New York: John Wiley & Sons, Ltd, 1982, ch. 8, pp. 201–250.

[35] G. Lu, N. Kioussis, V. V. Bulatov, and E. Kaxiras, "The Peierls-Nabarro model revisited," *Philosophical Magazine Letters*, vol. 80, no. 10, pp. 675–682, 2000. DOI: 10.1080/09500830050143778.

[36] H. B. Huntington, "Modification of the Peierls-Nabarro Model for Edge Dislocation Core," *Proceedings of the Physical Society. Section B*, vol. 68, no. 12, pp. 1043–1048, 1955. DOI: 10.1088/0370-1301/68/12/308.

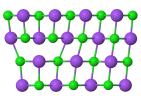

[37] W. Clegg, L. Vandeperre, and J. Pitchford, "Energy Changes and the Lattice Resistance," *Key Engineering Materials*, vol. 317-318, pp. 271–276, 2006. DOI: 10.4028/www.scientific.net/KEM.317-318.271.

[38] A. J. Foreman, M. A. Jaswon, and J. K. Wood, "Factors Controlling Dislocation Widths," *Proceedings of the Physical Society. Section A*, vol. 64, no. 2, pp. 156–163, 1951. DOI: 10.1088/0370-1298/64/2/307.

[39] A. A. Maradudin, "Screw dislocations and discrete elastic theory," *Journal of Physics and Chemistry of Solids*, vol. 9, no. 1, pp. 1–20, 1959. DOI: 10.1016/0022-3697(59)90084-8.

[40] K. Ohsawa, H. Koizumi, H. O. K. Kirchner, and T. Suzuki, "The critical stress in a discrete Peierls–Nabarro model," *Philosophical Magazine A*, vol. 69, no. 1, pp. 171–181, 1994. DOI: 10.1080/01418619408242216.

[41] V. Vitek, "Structure of dislocation cores in metallic materials and its impact on their plastic behaviour," *Progress in Materials Science*, vol. 36, pp. 1–27, 1992. DOI: 10.1016/0079-6425(92)90003-P.

[42] V. V. Bulatov and E. Kaxiras, "Semidiscrete Variational Peierls Framework for Dislocation Core Properties," *Physical Review Letters*, vol. 78, no. 22, pp. 4221–4224, 1997. DOI: 10.1103/PhysRevLett.78.4221.

[43] B. Joós and M. S. Duesbery, "The Peierls Stress of Dislocations: An Analytic Formula," *Physical Review Letters*, vol. 78, no. 2, pp. 266–269, 1997. DOI: 10.1103/PhysRevLett.78.266.

[44] V. A. Lubarda and X. Markenscoff, "Configurational force on a lattice dislocation and the Peierls stress," *Archive of Applied Mechanics*, vol. 77, no. 2-3, pp. 147–154, 2007. DOI: 10.1007/s00419-006-0068-y.

[45] D. Sangiovanni, L. Hultman, and V. Chirita, "Supertoughening in B1 transition metal nitride alloys by increased valence electron concentration," *Acta Materialia*, vol. 59, no. 5, pp. 2121–2134, 2011. DOI: 10.1016/j.actamat.2010.12.013.

[46] S. Aryal, R. Sakidja, M. W. Barsoum, and W.-Y. Ching, "A genomic approach to the stability, elastic, and electronic properties of the MAX phases," *Physica status solidi (b)*, vol. 251, no. 8, pp. 1480–1497, 2014. DOI: 10.1002/pssb.201451226.

[47] G. Wang, S. Schönecker, S. Hertzman, Q. M. Hu, B. Johansson, S. K. Kwon, *et al.*, "Ab initio prediction of the mechanical properties of alloys: The case of Ni/Mn-doped ferromagnetic Fe," *Physical Review B - Condensed Matter and Materials Physics*, vol. 91, no. 22, pp. 1–14, 2015. DOI: 10.1103/PhysRevB.91.224203.

[48] H. Hu, X. Wu, R. Wang, W. Li, and Q. Liu, "Phase stability, mechanical properties and electronic structure of TiAl alloying with W, Mo, Sc and Yb: First-principles study," *Journal of Alloys and Compounds*, vol. 658, pp. 689–696, 2016. DOI: 10.1016/j.jallcom.2015.10.270.

[49] H. L. Zhuang, M. Chen, and E. A. Carter, "Prediction and characterization of an Mg-Al intermetallic compound with potentially improved ductility via orbital-free and Kohn-Sham density functional theory," *Modelling and Simulation in Materials Science and Engineering*, vol. 25, no. 7, p. 075 002, 2017. DOI: 10.1088/1361-651X/aa7e0c.

[50] S. Pugh, "XCII. Relations between the elastic moduli and the plastic properties of polycrystalline pure metals," *The London, Edinburgh, and Dublin Philosophical Magazine and Journal of Science*, vol. 45, no. 367, pp. 823–843, 1954. DOI: 10.1080/14786440808520496.

[51] F. Stein, M. Palm, and G. Sauthoff, "Structure and stability of Laves phases. Part I. Critical assessment of factors controlling Laves phase stability," *Intermetallics*, vol. 12, no. 7-9 SPEC. ISS. Pp. 713–720, 2004. DOI: 10.1016/j.intermet.2004.02.010.

[52] F. Stein, M. Palm, and G. Sauthoff, "Structure and stability of Laves phases part II - Structure type variations in binary and ternary systems," *Intermetallics*, vol. 13, no. 10, pp. 1056–1074, 2005. DOI: 10.1016/j.intermet.2004.11.001.

[53] F. Chu, Y. He, D. Thoma, and T. Mitchell, "Elastic constants of the C15 laves phase compound $NbCr_2$," *Scripta Metallurgica et Materialia*, vol. 33, no. 8, pp. 1295–1300, 1995. DOI: 10.1016/0956-716X(95)00357-2.

[54] M. W. Barsoum and M. Radovic, "Elastic and Mechanical Properties of the MAX Phases," *Annual Review of Materials Research*, vol. 41, no. 1, pp. 195–227, 2011. DOI: 10.1146/annurev-matsci-062910-100448.

[55] J. R. Rice and R. Thomson, "Ductile versus brittle behaviour of crystals," *Philosophical Magazine*, vol. 29, no. 1, pp. 73–97, 1974. DOI: 10.1080/14786437408213555.

[56] J. R. Rice, "Dislocation nucleation from a crack tip: An analysis based on the Peierls concept," *Journal of the Mechanics and Physics of Solids*, vol. 40, no. 2, pp. 239–271, 1992. DOI: 10.1016/S0022-5096(05)80012-2.

[57] S. J. Zhou, A. E. Carlsson, and R. Thomson, "Crack blunting effects on dislocation emission from cracks," *Physical Review Letters*, vol. 72, no. 6, pp. 852–855, 1994. DOI: 10.1103/PhysRevLett.72.852.

[58] D. L. Price, B. R. Cooper, and J. M. Wills, "Full-potential linear-muffin-tin-orbital study of brittle fracture in titanium carbide," *Physical Review B*, vol. 46, no. 18, pp. 11 368–11 375, 1992. DOI: 10.1103/PhysRevB.46.11368.

[59] R. Yu, L. L. He, and H. Q. Ye, "Effects of Si and Al on twin boundary energy of TiC," *Acta Materialia*, vol. 51, no. 9, pp. 2477–2484, 2003. DOI: 10.1016/S1359-6454(03)00032-6.

[60] N. I. Medvedeva, A. N. Enyashin, and A. L. Ivanovskii, "Modeling of the electronic structure, chemical bonding, and properties of ternary silicon carbide Ti_3SiC_2," *Journal of Structural Chemistry*, vol. 52, no. 4, pp. 785–802, 2011. DOI: 10.1134/S0022476611040226.

[61] A. S. Farle, C. Kwakernaak, S. van der Zwaag, and W. G. Sloof, "A conceptual study into the potential of $M_{n+1}AX_n$-phase ceramics for self-healing of crack damage," *Journal of the European Ceramic Society*, vol. 35, no. 1, pp. 37–45, 2015. DOI: 10.1016/j.jeurceramsoc.2014.08.046.

[62] D. B. Miracle and H. A. Lipsitt, "Mechanical Properties of Fine-Grained Substoichiomebic Titanium Carbide," *Journal of the American Ceramic Society*, vol. 66, no. 8, pp. 592–597, 1983. DOI: 10.1111/j.1151-2916.1983.tb10098.x.

[63] M. W. Barsoum and T. El-Raghy, "Room-temperature ductile carbides," *Metallurgical and Materials Transactions A*, vol. 30, no. 2, pp. 363–369, 1999. DOI: 10.1007/s11661-999-0325-0.

[64] C. Humphrey, "Deformation in MAX Phases," PhD thesis, University of Cambridge, 2012.

[65] D. G. Sangiovanni, V. Chirita, and L. Hultman, "Electronic mechanism for toughness enhancement in$TixM_{1-x}N$ (M=Mo and W)," *Physical Review B*, vol. 81, no. 10, p. 104 107, 2010. DOI: 10.1103/PhysRevB.81.104107.

[66] D. Music and J. M. Schneider, "Elastic properties of $Sr_{n+1}Ti_nO_{3n+1}$ phases (n =1–3, ∞)," *Journal of Physics: Condensed Matter*, vol. 20, no. 5, p. 055 224, 2008. DOI: 10.1088/0953-8984/20/5/055224.

[67] J. Emmerlich, D. Music, M. Braun, P. Fayek, F. Munnik, and J. M. Schneider, "A proposal for an unusually stiff and moderately ductile hard coating material: Mo_2BC," *Journal of Physics D: Applied Physics*, vol. 42, no. 18, p. 185 406, 2009. DOI: 10.1088/0022-3727/42/18/185406.

[68] K. Gouriet, P. Carrez, P. Cordier, A. Guitton, A. Joulain, L. Thilly, *et al.*, "Dislocation modelling in Ti_2AlN MAX phase based on the Peierls-Nabarro model," *Philosophical Magazine*, vol. 95, no. 23, pp. 2539–2552, 2015. DOI: 10.1080/14786435.2015.1066938.

[69] G. E. Hollox and R. E. Smallman, "Plastic behavior of titanium carbide," *Journal of Applied Physics*, vol. 37, no. 2, pp. 818–823, 1966. DOI: 10.1063/1.1708264.

[70] S. Korte and W. J. Clegg, "Studying plasticity in hard and soft Nb-Co intermetallics," *Advanced Engineering Materials*, vol. 14, no. 11, pp. 991–997, 2012. DOI: 10.1002/adem.201200175.

[71] R. Telle, A. Momozawa, D. Music, and J. M. Schneider, "Boride-based nano-laminates with MAX-phase-like behaviour," *Journal of Solid State Chemistry*, vol. 179, no. 9, pp. 2850–2857, 2006. DOI: 10.1016/j.jssc.2006.01.028.

[72] M. Sygnatowicz, R. A. Cutler, and D. K. Shetty, "ζ-Ta_4C_{3-x}: A High Fracture Toughness Carbide with Rising-Crack-Growth-Resistance (R-Curve) Behavior," *Journal of the American Ceramic Society*, vol. 98, no. 8, C.-H. Hsueh, Ed., pp. 2601–2608, 2015. DOI: 10.1111/jace.13635.

[73] M. Radovic and M. W. Barsoum, "MAX phases: Bridging the gap between metals and ceramics," *American Ceramic Society Bulletin*, vol. 92, no. 3, pp. 20–27, 2013.

[74] K. Momma and F. Izumi, "VESTA 3 for three-dimensional visualization of crystal, volumetric and morphology data," *Journal of Applied Crystallography*, vol. 44, no. 6, pp. 1272–1276, 2011. DOI: 10.1107/S0021889811038970.

[75] W. Steurer, "Stable clusters in quasicrystals: Fact or fiction?" *Philosophical Magazine*, vol. 86, no. 6-8, pp. 1105–1113, 2006. DOI: 10.1080/14786430500419387.

[76] Z. M. Sun, "Progress in research and development on MAX phases: a family of layered ternary compounds," *International Materials Reviews*, vol. 56, no. 3, pp. 143–166, 2011. DOI: 10.1179/1743280410Y.0000000001.

[77] W. Feng, S. Cui, H. Hu, P. Feng, Z. Zheng, Y. Guo, *et al.*, "First-principles study on electronic structure and elastic properties of hexagonal Zr_2SC," *Physica B: Condensed Matter*, vol. 405, no. 20, pp. 4294–4298, 2010. DOI: 10.1016/j.physb.2010.07.029.

[78] L. Farber, M. W. Barsoum, A. Zavaliangos, T. El-Raghy, and I. Levin, "Dislocations and Stacking Faults in Ti_3SiC_2," *Journal of the American Ceramic Society*, vol. 81, no. 6, pp. 1677–1681, 2005. DOI: 10.1111/j.1151-2916.1998.tb02532.x.

[79] L. Farber, "High-resolution transmission electron microscopy study of a low-angle boundary in plastically deformed Ti_3SiC_2," *Philosophical Magazine Letters*, vol. 79, no. 4, pp. 163–170, 1999. DOI: 10.1080/095008399177390.

[80] M. W. Barsoum, L. Farber, and T. El-Raghy, "Dislocations, kink bands, and room-temperature plasticity of Ti_3SiC_2," *Metallurgical and Materials Transactions A*, vol. 30, no. 7, pp. 1727–1738, 1999. DOI: 10.1007/s11661-999-0172-z.

[81] M. W. Barsoum, M. Radovic, P. Finkel, and T. El-Raghy, "TI_3SIC_2 AND ICE," *Applied Physics Letters*, vol. 79, no. 4, pp. 479–481, 2001. DOI: 10.1063/1.1384479.

[82] D. Music, A. Houben, R. Dronskowski, and J. M. Schneider, "Ab initio study of ductility in M_2AlC (M = Ti, V, Cr)," *Physical Review B*, vol. 75, no. 17, p. 174 102, 2007. DOI: 10.1103/PhysRevB.75.174102.

[83] J. A. Martinez, D. E. Yilmaz, T. Liang, S. B. Sinnott, and S. R. Phillpot, "Fitting empirical potentials: Challenges and methodologies," *Current Opinion in Solid State and Materials Science*, vol. 17, no. 6, pp. 263–270, 2013. DOI: 10.1016/j.cossms.2013.09.001.

[84] M. S. Daw and M. I. Baskes, "Embedded-atom method: Derivation and application to impurities, surfaces, and other defects in metals," *Physical Review B*, vol. 29, no. 12, pp. 6443–6453, 1984. DOI: 10.1103/PhysRevB.29.6443.

[85] J. E. Jones, "On the Determination of Molecular Fields. II. From the Equation of State of a Gas," *Proceedings of the Royal Society A: Mathematical, Physical and Engineering Sciences*, vol. 106, no. 738, pp. 463–477, 1924. DOI: 10.1098/rspa.1924.0082.

[86] R. A. Buckingham, "The Classical Equation of State of Gaseous Helium, Neon and Argon," *Proceedings of the Royal Society A: Mathematical, Physical and Engineering Sciences*, vol. 168, no. 933, pp. 264–283, 1938. DOI: 10.1098/rspa.1938.0173.

[87] J. Tersoff, "New empirical approach for the structure and energy of covalent systems," *Physical Review B*, vol. 37, no. 12, pp. 6991–7000, 1988. DOI: 10.1103/PhysRevB.37.6991.

[88] C. R. Miranda and S. Scandolo, "Computational materials science meets geophysics: dislocations and slip planes of MgO," *Computer Physics Communications*, vol. 169, no. 1-3, pp. 24–27, 2005. DOI: 10.1016/j.cpc.2005.03.007.

[89] A. Kelly and K. M. Knowles, "Appendix 7: Crystal Structure Data," in *Crystallography and Crystal Defects*, 2nd ed., Chichester, UK: John Wiley & Sons, Ltd, 2012, ch. A7, pp. 491–498. DOI: 10.1002/9781119961468.app7.

[90] E. Madelung, "Das elektrische Feld in Systemen von regelmäßig angeordneten Punktladungen," *Physikalische Zeitschrift*, vol. 19, pp. 524–533, 1918.

[91] P. P. Ewald, "Die Berechnung optischer und elektrostatischer Gitterpotentiale," *Annalen der Physik*, vol. 369, no. 3, pp. 253–287, 1921. DOI: 10.1002/andp.19213690304.

[92] S. van der Walt, S. C. Colbert, and G. Varoquaux, "The NumPy Array: A Structure for Efficient Numerical Computation," *Computing in Science & Engineering*, vol. 13, no. 2, pp. 22–30, 2011. DOI: 10.1109/MCSE.2011.37.

[93] D. Smith, F.-R. Stöter, R. T. McGibbon, and N. Werner, *Optimised Einsum: A tensor contraction order optimizer*, 2017. DOI: 10.5281/zenodo.829918. [Online]. Available: https://github.com/dgasmith/opt_einsum.

[94] D. J. Hardy, J. E. Stone, and K. Schulten, "Multilevel summation of electrostatic potentials using graphics processing units," *Parallel Computing*, vol. 35, no. 3, pp. 164–177, 2009. DOI: 10.1016/j.parco.2008.12.005.

[95] S. Plimpton, "Fast Parallel Algorithms for Short-Range Molecular Dynamics," *Journal of Computational Physics*, vol. 117, no. 1, pp. 1–19, 1995. DOI: 10.1006/jcph.1995.1039.

[96] *LAMMPS Molecular Dynamics Simulator*, URL: lammps.sandia.gov, Accessed November 2017.

[97] P. Haasen, "Dislocations and the plasticity of ionic crystals," *Materials Science and Technology*, vol. 1, no. 12, pp. 1013–1024, 1985. DOI: 10.1179/026708385790123766.

[98] M. P. Puls and M. J. Norgett, "Atomistic calculation of the core structure and Peierls energy of an $(a/2)$ [1 1 0] edge dislocation in MgO," *Journal of Applied Physics*, vol. 47, no. 2, pp. 466–477, 1976. DOI: 10.1063/1.322670.

[99] C. H. Woo and M. P. Puls, "Atomistic breathing shell model calculations of dislocation core configurations in ionic crystals," *Philosophical Magazine*, vol. 35, no. 3, pp. 727–756, 1977. DOI: 10.1080/14786437708236001.

[100] F. Granzer, G. Wagner, and J. Eisenblätter, "Atomistische Berechnung der Core-Struktur, Core-Energie und Peierls-Spannung einer Stufenversetzung in NaCl," *Physica Status Solidi (b)*, vol. 30, no. 2, pp. 587–600, 1968. DOI: 10.1002/pssb.19680300220.

[101] C. H. Woo and M. P. Puls, "An improved method of calculating the lattice friction stress using an atomistic model," *Journal of Physics C: Solid State Physics*, vol. 9, no. 2, pp. L27–L31, 1976. DOI: 10.1088/0022-3719/9/2/001.

[102] R. G. Hoagland, J. P. Hirth, and P. C. Gehlen, "Atomic simulation of the dislocation core structure and Peierls stress in alkali halide," *Philosophical Magazine*, vol. 34, no. 3, pp. 413–439, 1976. DOI: 10.1080/14786437608222033.

[103] S. Brandt, W. Skrotzki, and P. Haasen, "Internal Friction of deformed NaCl," *Le Journal de Physique Colloques*, vol. 48, no. C8, pp. C8–89–C8–94, 1987. DOI: 10.1051/jphyscol:1987809.

[104] J. Soullard, "The interaction force between the tetragonal defects and edge dislocations in the rock salt structure," *Philosophical Magazine A*, vol. 64, no. 1, pp. 39–53, 1991. DOI: 10.1080/01418619108206125.

[105] A. Foitzik, W. Skrotzki, and P. Haasen, "Slip on {1 1 1} planes in lead sulphide," *Materials Science and Engineering: A*, vol. 132, no. C, pp. 77–82, 1991. DOI: 10.1016/0921-5093(91)90363-R.

[106] J. D. Eshelby, "LXXXII. Edge dislocations in anisotropic materials," *The London, Edinburgh, and Dublin Philosophical Magazine and Journal of Science*, vol. 40, no. 308, pp. 903–912, 1949. DOI: 10.1080/14786444908561420.

[107] R. P. Thompson, *Pyerls - Python modelling of dislocations using the Peierls analysis*, Archived November 2017 on Zenodo.org. DOI: 10.5281/zenodo.1065538, current version on Github.com URL: https://github.com/rpt26/pyerls.

[108] J. P. Hirth and J. Lothe, "The Theory of Straight Dislocations," in *Theory of Dislocations*, 2nd ed., New York: John Wiley & Sons, Ltd, 1968, ch. 3, pp. 58–90.

[109] J. P. Hirth and J. Lothe, "The influence of lattice periodicity," in *Theory of Dislocations*, 2nd ed., John Wiley & Sons, Ltd, 1982, ch. 8, pp. 201–250.

[110] G. Leibfried and K. Lücke, "ÜBER DAS SPANNUNGSFELD EINER VERSETZUNG," *Zeitschrift für Physik*, vol. 126, no. 5, pp. 450–464, 1949. DOI: 10.1007/BF01669489.

[111] F. R. N. Nabarro, "Stationary Dislocations in a Crystal," in *Theory of crystal dislocations*, ser. Dover Books on Physics and Chemistry, New York: Dover Publications, 1987, ch. 3, pp. 120–154.

[112] P. S. Theocaris, "The limits of Poisson's ratio in polycrystalline bodies," *Journal of Materials Science*, vol. 29, no. 13, pp. 3527–3534, 1994. DOI: 10.1007/BF00352059.

[113] B. S. Rao and S. P. Sanyal, "Structural and elastic properties of sodium halides at high pressure," *Physical Review B*, vol. 42, no. 3, pp. 1810–1816, 1990. DOI: 10.1103/PhysRevB.42.1810.

[114] H. J. Frost and M. F. Ashby, "Effect of pressure on plastic flow," in *Deformation-mechanism maps: The plasticity and creep of metals and ceramics*, Pergamon Press, 1982, ch. 17, pp. 129–130.

[115] J. Gruber, A. C. Lang, J. Griggs, M. L. Taheri, G. J. Tucker, and M. W. Barsoum, "Evidence for Bulk Ripplocations in Layered Solids," *Scientific Reports*, vol. 6, no. 1, p. 33 451, 2016. DOI: 10.1038/srep33451.

[116] A. Kelly and K. M. Knowles, "Tensors," in *Crystallography and Crystal Defects*, 2nd ed., Chichester, UK: John Wiley & Sons, Ltd, 2012, ch. 5, pp. 141–163. DOI: 10.1002/9781119961468.ch5.

[117] A. Kelly and K. M. Knowles, "Strain, Stress, Piezoelectricity and Elasticity," in *Crystallography and Crystal Defects*, 2nd ed., Chichester, UK: John Wiley & Sons, Ltd, 2012, ch. 6, pp. 165–196. DOI: 10.1002/9781119961468.ch6. [Online]. Available: http://doi.wiley.com/10.1002/9781119961468.ch6.

[118] J. P. Hirth and J. Lothe, "Elasticity," in *Theory of Dislocations*, 2nd ed., New York: John Wiley & Sons, Ltd, 1982, ch. 2, pp. 29–57.

[119] F. Perez and B. E. Granger, "IPython: A System for Interactive Scientific Computing," *Computing in Science & Engineering*, vol. 9, no. 3, pp. 21–29, 2007. DOI: 10.1109/MCSE.2007.53.

[120] K. J. Millman and M. Aivazis, "Python for Scientists and Engineers," *Computing in Science & Engineering*, vol. 13, no. 2, pp. 9–12, 2011. DOI: 10.1109/MCSE.2011.36.

[121] E. Jones, T. Oliphant, P. Peterson, *et al.*, *SciPy: Open source scientific tools for Python*, URL: www.scipy.org/, Accessed November 2017, (2001–).

[122] A. Hjorth Larsen, J. Jørgen Mortensen, J. Blomqvist, I. E. Castelli, R. Christensen, M. Dułak, *et al.*, "The atomic simulation environment—a Python library for working with atoms," *Journal of Physics: Condensed Matter*, vol. 29, no. 27, p. 273 002, 2017. DOI: 10.1088/1361-648X/aa680e.

[123] A. H. Mao and R. V. Pappu, "Crystal lattice properties fully determine short-range interaction parameters for alkali and halide ions," *The Journal of Chemical Physics*, vol. 137, no. 6, p. 064 104, 2012. DOI: 10.1063/1.4742068.

[124] J. Nocedal and S. Wright, *Numerical Optimization*, second, ser. Springer Series in Operations Research and Financial Engineering. New York: Springer New York, 2006, p. 136. DOI: 10.1007/978-0-387-40065-5.

[125] J. A. Nelder and R. Mead, "A Simplex method for function minimization," *The Computer Journal*, vol. 7, no. 4, pp. 308–313, 1965. DOI: 10.1093/comjnl/7.4.308.

[126] F. Gao and L. Han, "Implementing the Nelder-Mead simplex algorithm with adaptive parameters," *Computational Optimization and Applications*, vol. 51, no. 1, pp. 259–277, 2012. DOI: 10.1007/s10589-010-9329-3.

[127] M. A. Stopher, "Hydrogen embrittlement in nuclear alloys and bearing steels: From quantum mechanics to thermokinetics," PhD thesis, University of Cambridge, 2017.

[128] W. Köster and H. Franz, "Poisson's ratio for metals and alloys," *Metallurgical Reviews*, vol. 6, no. 21, pp. 1–56, 1961. DOI: 10.1179/mtlr.1961.6.1.1.

[129] J. Wang, "Prediction of Peierls stresses for different crystals," *Materials Science and Engineering: A*, vol. 206, no. 2, pp. 259–269, 1996.

[130] R. Chang and L. J. Graham, "Low-Temperature Elastic Properties of ZrC and TiC," *Journal of Applied Physics*, vol. 37, no. 10, pp. 3778–3783, 1966. DOI: 10.1063/1.1707923.

[131] Y. Kamimura, K. Edagawa, and S. Takeuchi, "Peierls Stresses Estimated from CRSS vs. Temperature Curve and Their Relation to the Crystal Structure," *Key Engineering Materials*, vol. 465, pp. 97–100, 2011. DOI: 10.4028/www.scientific.net/KEM.465.97.

[132] S. Yadav, R. Ramprasad, A. Misra, and X.-Y. Liu, "Core structure and Peierls stress of edge and screw dislocations in TiN: A density functional theory study," *Acta Materialia*, vol. 74, pp. 268–277, 2014. DOI: 10.1016/j.actamat.2014.04.047.

[133] M. Magnuson and M. Mattesini, "Chemical bonding and electronic-structure in MAX phases as viewed by X-ray spectroscopy and density functional theory," *Thin Solid Films*, vol. 621, pp. 108–130, 2017. DOI: 10.1016/j.tsf.2016.11.005.

[134] H.-I. Yoo, M. W. Barsoum, and T. El-Raghy, "Materials science: Ti_3SiC_2 has negligible thermopower," *Nature*, vol. 407, pp. 581–582, 2000. DOI: 10.1038/35036686.

[135] D. Music, Z. Sun, R. Ahuja, and J. Schneider, "Surface energy of $M_2AC(0\,0\,0\,1)$ determined by density functional theory (M=Ti,V,Cr; A=Al,Ga,Ge)," *Surface Science*, vol. 601, no. 4, pp. 896–899, 2007. DOI: 10.1016/j.susc.2006.11.025.

[136] R. S. Mulliken, "A New Electroaffinity Scale; Together with Data on Valence States and on Valence Ionization Potentials and Electron Affinities," *The Journal of Chemical Physics*, vol. 2, no. 11, pp. 782–793, 1934. DOI: 10.1063/1.1749394.

[137] J. E. Huheey, "Bonding models in inorganic chemistry," in *Inorganic chemistry: Principles of structure and reactivity*, 3rd ed., Harper & Row, 1983, ch. 3, pp. 137–160, ISBN: 9780063629875.

[138] K. Lejaeghere, G. Bihlmayer, T. Bjorkman, P. Blaha, S. Blugel, V. Blum, *et al.*, "Reproducibility in density functional theory calculations of solids," *Science*, vol. 351, no. 6280, aad3000, 2016. DOI: 10.1126/science.aad3000.

[139] J. M. Soler, E. Artacho, J. D. Gale, A. García, J. Junquera, P. Ordejón, *et al.*, "The SIESTA method for *ab initio* order-N materials simulation," *Journal of Physics: Condensed Matter*, vol. 14, no. 11, pp. 2745–2779, 2002. DOI: 10.1088/0953-8984/14/11/302.

[140] N. Troullier and J. L. Martins, "Efficient pseudopotentials for plane-wave calculations," *Physical Review B*, vol. 43, no. 3, pp. 1993–2006, 1991. DOI: 10.1103/PhysRevB.43.1993.

[141] N. Troullier and J. L. Martins, "Efficient pseudopotentials for plane-wave calculations. II. Operators for fast iterative diagonalization," *Physical Review B*, vol. 43, no. 11, pp. 8861–8869, 1991. DOI: 10.1103/PhysRevB.43.8861.

[142] A. García, *ATOM User Manual*, URL: https://departments.icmab.es/leem/siesta/Pseudopotentials/Code/downloads.html, Accessed November 2017.

[143] E. Artacho, J. M. Cela, J. D. Gale, A. García, J. Junquera, R. M. Martin, *et al.*, *SIESTA 4.0 – User's Guide*, URL: https://departments.icmab.es/leem/siesta/Documentation/, Accessed Novemeber 2017. [Online]. Available: https://departments.icmab.es/leem/siesta/Documentation/.

[144] V. N. Staroverov, G. E. Scuseria, J. Tao, and J. P. Perdew, "Tests of a ladder of density functionals for bulk solids and surfaces," *Physical Review B*, vol. 69, no. 7, p. 075 102, 2004. DOI: 10.1103/PhysRevB.69.075102.

[145] Z. Wu and R. E. Cohen, "More accurate generalized gradient approximation for solids," *Physical Review B*, vol. 73, no. 23, p. 235 116, 2006. DOI: 10.1103/PhysRevB.73.235116.

[146] V. N. Staroverov, G. E. Scuseria, J. Tao, and J. P. Perdew, "Erratum: Tests of a ladder of density functionals for bulk solids and surfaces [Phys. Rev. B 69 , 075102 (2004)]," *Physical Review B*, vol. 78, no. 23, p. 239 907, 2008. DOI: 10.1103/PhysRevB.78.239907.

[147] D. Hull and T. W. Clyne, "Elastic deformation of long-fibre composites," in *An Introduction to Composite Materials*, ser. Cambridge Solid State Science Series, D. R. Clarke, S. Suresh, and I. M. Ward, Eds., 2nd ed., Cambridge: Cambridge University Press, 1996, ch. 4, pp. 60–77. DOI: 10.1017/CBO9781139170130.006. [Online]. Available: http://ebooks.cambridge.org/ref/id/CBO9781139170130A025.

[148] A. Kelly and K. M. Knowles, "Dislocations in Crystals," in *Crystallography and Crystal Defects*, 2nd ed., Chichester, UK: John Wiley & Sons, Ltd, 2012, ch. 9, pp. 269–304. DOI: 10.1002/9781119961468.ch9.

[149] P. R. Howie, R. P. Thompson, S. Korte-Kerzel, and W. J. Clegg, "Softening non-metallic crystals by inhomogeneous elasticity," *Scientific Reports*, vol. 7, no. 1, p. 11 602, 2017. DOI: 10.1038/s41598-017-09453-1.

[150] G. A. Yurko, J. W. Barton, and J. G. Parr, "The crystal structure of Ti_2Ni," *Acta Crystallographica*, vol. 12, no. 11, pp. 909–911, 1959. DOI: 10.1107/S0365110X59002559.

[151] G. A. Yurko, J. W. Barton, and J. G. Parr, "The crystal structure of Ti_2Ni (a correction)," *Acta Crystallographica*, vol. 15, no. 12, pp. 1309–1309, 1962. DOI: 10.1107/S0365110X62003448.

[152] *Inorganic crystal structure database – ICSD*, URL: icsd.cds.rsc.org, Accessed November 2017.

[153] N. Ivanović, D. Rodić, V. Koteski, I. Radisavljević, N. Novaković, D. Marjanović, *et al.*, "Cluster approach to the Ti_2Ni structure type," *Acta Crystallographica Section B: Structural Science*, vol. 62, no. 1, pp. 1–8, 2006. DOI: 10.1107/S010876810503764X.

[154] C. E. Davis, "Deformation in Laves phases," PhD thesis, University of Cambridge, 2015.

[155] W. G. Pfann, *Zone Melting*, Second. New York: John Wiley & Sons, Inc., 1966, pp. 277–278.

[156] D. T. Griggs, "Deformation of Rocks under High Confining Pressures: I. Experiments at Room Temperature," *The Journal of Geology*, vol. 44, no. 5, pp. 541–577, 1936. DOI: 10.1086/624455.

[157] I. E. French and P. F. Weinrich, "The influence of hydrostatic pressure on the tensile deformation and fracture of copper," *Metallurgical Transactions A*, vol. 6, no. 4, pp. 785–790, 1975. DOI: 10.1007/BF02672300.

[158] P. Borvin, J. Rabier, and H. Garem, "Plastic deformation of GaAs single crystals as a function of electronic doping II: Low temperatures (20 °C–300 °C)," *Philosophical Magazine A*, vol. 61, no. 4, pp. 647–672, 1990. DOI: 10.1080/01418619008231940.

[159] M. D. Uchic, "Sample Dimensions Influence Strength and Crystal Plasticity," *Science*, vol. 305, no. 5686, pp. 986–989, 2004. DOI: 10.1126/science.1098993.

[160] A. C. Fischer-Cripps, *Nanoindentation*, ser. Mechanical Engineering Series. New York, NY: Springer, 2011. DOI: 10.1007/978-1-4419-9872-9. [Online]. Available: http://link.springer.com/10.1007/978-1-4419-9872-9.

[161] A. G. Quarrell, *The Hardness of Metals*, ser. Monographs on the physics and chemistry of materials 4333. Oxford: OUP, 1952, vol. 170, p. 818. DOI: 10.1038/170818b0.

[162] D. M. Marsh, "Plastic Flow in Glass," *Proceedings of the Royal Society A: Mathematical, Physical and Engineering Sciences*, vol. 279, no. 1378, pp. 420–435, 1964. DOI: 10.1098/rspa.1964.0114.

[163] S. Korte, "Plasticity in ceramics - Deformation in small volumes," PhD thesis, University of Cambridge, 2009.

[164] J. R. Greer, W. C. Oliver, and W. D. Nix, "Size dependence of mechanical properties of gold at the micron scale in the absence of strain gradients," *Acta Materialia*, vol. 53, no. 6, pp. 1821–1830, 2005. DOI: 10.1016/j.actamat.2004.12.031.

[165] J. R. Greer, W. Oliver, and W. Nix, "Corrigendum to "Size dependence in mechanical properties of gold at the micron scale in the absence of strain gradients" [Acta Mater 53 (6) (2005) 1821–1830]," *Acta Materialia*, vol. 54, no. 6, p. 1705, 2006. DOI: 10.1016/j.actamat.2005.12.004.

[166] S. J. Clark, M. D. Segall, C. J. Pickard, P. J. Hasnip, M. I. J. Probert, K. Refson, *et al.*, "First principles methods using CASTEP," *Zeitschrift für Kristallographie - Crystalline Materials*, vol. 220, no. 5/6, p. 567, 2005. DOI: 10.1524/zkri.220.5.567.65075.

Appendix A

Inputs

A.1 Elastic Tensors for cementite under different levels of hydrogen loading

The elastic tensors for cementite loaded with varying amounts of hydrogen used for a Peierls analysis, discussed in subsection 2.3.1, are given below. These were calculated by DFT using CASTEP [166] by Miles Stopher and David Bombac, see [127] for more details.

$$C_{ij}^{0\mathrm{H}} = \begin{pmatrix} 387.2 & 153.0 & 155.4 & 0 & 0 & 0 \\ 153.0 & 342.7 & 158.0 & 0 & 0 & 0 \\ 155.4 & 158.0 & 308.5 & 0 & 0 & 0 \\ 0 & 0 & 0 & 133.1 & 0 & 0 \\ 0 & 0 & 0 & 0 & 16.8 & 0 \\ 0 & 0 & 0 & 0 & 0 & 132 \end{pmatrix}$$

$$C_{ij}^{5\mathrm{H}} = \begin{pmatrix} 373.7 & 155.3 & 128.4 & -1.7 & 3.4 & 6.3 \\ 155.3 & 343.6 & 173.8 & 3.3 & -7.3 & -0.8 \\ 128.4 & 173.8 & 286.6 & 2.6 & -9.9 & 1.7 \\ -1.7 & 3.3 & 2.6 & 128.9 & -8 & 0.2 \\ 3.4 & -7.3 & -9.9 & -8 & 32.3 & -1 \\ 6.3 & -0.8 & 1.7 & 0.2 & -1 & 130.1 \end{pmatrix}$$

$$C_{ij}^{7\mathrm{H}} = \begin{pmatrix} 341.3 & 134.2 & 127.6 & 0 & 0 & 4.4 \\ 134.2 & 306.1 & 162.6 & 0 & 0 & 3.4 \\ 127.6 & 162.6 & 288.6 & 0 & 0 & 18.9 \\ 0 & 0 & 0 & 64.6 & 0.8 & 0 \\ 0 & 0 & 0 & 0.8 & 27.7 & 0 \\ 4.4 & 3.4 & 18.9 & 0 & 0 & 103.5 \end{pmatrix}$$

$$C_{ij}^{10\mathrm{H}} = \begin{pmatrix} 331.4 & 127.2 & 130.5 & 0 & 0 & -6.8 \\ 127.2 & 222.8 & 140.1 & 0 & 0 & 1.3 \\ 130.5 & 140.1 & 279.5 & 0 & 0 & -0.3 \\ 0 & 0 & 0 & 95.3 & 3.8 & 0 \\ 0 & 0 & 0 & 3.8 & 61.4 & 0 \\ -6.8 & 1.3 & -0.3 & 0 & 0 & 44.3 \end{pmatrix}$$

A.2 Elastic Tensors for the "simple materials" used to benchmark the Peierls Model

A.3 LAMMPS inputs

Input file:

```
# rpt26@cam.ac.uk getting his teeth into LAMMPS

units metal
dimension 3
boundary f f p
atom_style charge
pair_style lj/cut/coul/msm 15
kspace_style msm 1e-4
read_data data.example
mass 1 22.9
mass 2 35.45
pair_coeff 1 2 0.00206669 3.5545
pair_coeff 1 1 0.0039367 2.497
pair_coeff 2 2 0.00108497 4.612
neighbor 3.2 bin
neigh_modify page 200000000
neigh_modify one 10000000
velocity all zero linear
velocity all zero angular
fix 1 all setforce 0.0 0.0 0.0
thermo_style multi
run 0
```

Data file:

```
# RPT26 on a LAMMPS adventure

8 atoms
2 atom types
-395.944775937 397.060724007 xlo xhi
-563.919131627 559.447761272 ylo yhi
-0.997727668254 2.99318300476 zlo zhi

Atoms

1 1 1 3.07845 6.64186 0
2 1 1 5.04441 9.39267 1.99546
3 2 -1 4.96587 6.59076 1.99546
4 2 -1 3.13155 9.42639 0
5 1 1 6.86751 6.53876 0
6 1 1 8.88857 9.31457 1.99546
7 2 -1 8.78479 6.4919 1.99546
8 2 -1 6.96277 9.35369 0
```